Dissertation for the Degree of Doctor of Philosophy

Full Stokes Ice Models and Subglacial Heat Sources

Numerical Simulations of Volcano-Ice Interaction

Alexander H. Jarosch

UNIVERSITY OF ICELAND

Academic Dissertation

A Dissertation Presented to the University of Iceland Faculty of Science in
Candidacy for the Degree of Doctor of Philosophy

Supervisor

Dr. Magnús Tumi Guðmundsson
Institute of Earth Sciences, University of Iceland

Doctoral Committee

Dr. Magnús Tumi Guðmundsson
Institute of Earth Sciences, University of Iceland

Dr. Guðni Axelsson
Iceland GeoSurvey (ÍSOR)

Dr. Sveinn Jakobsson
Icelandic Institute of Natural History
(Náttúrufræðistofnun Íslands)

Opponents

Dr. Richard Hindmarsh
Physical Sciences Division, British Antarctic Survey
Cambridge, United Kingdom

Dr. Tómas Jóhannesson
Icelandic Meteorological Office (Veðurstofa Íslands)
Reykjavík, Iceland

for Lina and Carla

Contents

List of Figures

List of Tables

List of Symbols

v_s — ice surface velocity (page 61)

V — surface depression volume (page 64)

E_tot — total eruption energy (page 66)

m_m — mass of erupted magma (page 66)

c_m — specific heat content of magma (page 66)

T_er — eruption temperature (page 66)

T_0 — final temperature after cooling (page 66)

E_rel — total energy released during 1996-2005 (page 66)

t_er — time at the end of the Gjálp eruption (page 66)

E_er — energy released during the Gjálp eruption (page 66)

t_end — time at the end of study period (June 2005) (page 66)

E_post — energy released between t_er and t_end (page 66)

E_m — energy stored in erupted magma (page 66)

ΔT — temperature difference (page 66)

T_av — average temperature within Gjálp (page 68)

m_w — mass of water within pore space (page 68)

c_w — specific heat capacity of water (page 68)

m_ridge — mass of Gjálp ridge after eruption (page 68)

C_ridge — heat capacity of Gjálp ridge (page 68)

δT — error in temperature (page 69)

q_w — volumetric flow rate per unit area (page 69)

Abstract

Volcanic areas that lie beneath ice occur in several places on Earth, and include several ice-filled calderas, parts of Antarctica and the ice caps in Iceland, notably Vatnajökull and Mýrdalsjökull. Volcano-ice interaction can cause jökulhlaups, create subglacial mountains and may enhance sliding of ice masses by meltwater lubrication of the ice-bedrock interface. The aim of the research presented in this thesis was to advance the quantitative study of volcano-ice interaction. The research objectives were: (i) to simulate numerically the ice dynamics above subglacial heat sources with a state of the art ice flow model; (ii) the development of methods to infer subglacial heat source parameters by using glacial surface data and (iii) the construction of the heat output record from the subglacial hyaloclastite ridge (edifice) formed in the 1996 Gjálp eruption, Vatnajökull, Iceland. The main findings can be summarized as:

(i) An open source, finite element ice flow model was developed, termed Icetools, to simulate the ice dynamics caused by the interaction between subglacial heat sources and ice using Full Stokes equations. The performance of Icetools was investigated with numerical tests for linear and non-linear ice rheologies: (1) for gravity driven flow down an inclined plane, and (2) for flow over a Gaussian-shaped bed disturbance, a test not yet investigated numerically. The model results correlate well with the analytical solutions and reach steady state.

(ii) Icetools has been used to study the temporal evolution of an elongated depression on the eastern side of the geothermally active Grímsvötn caldera. The 100-150 m deep depression formed gradually between 1998 and 2004. The model results show that heat flux estimates based on depression volume are strongly dependent on the value of the rate factor A in Glen's flow law. If flow of ice into the depression is not taken into account, heat flux underestimates of 15-75 % occur, corresponding to rate factors of $10 - 68 \times 10^{-16}\mathrm{s}^{-1}\mathrm{kPa}^{-3}$. The estimated heat flux at the study site was 260-390 W m^{-2}, with the best estimate being 280 W m^{-2}, obtained from the best estimate of $A = 23 \times 10^{-16}\mathrm{s}^{-1}\mathrm{kPa}^{-3}$. The total power of the modeled site was 250-300 MW, about one tenth of the total heat output of Grímsvötn. This heat flux is of comparable magnitude to that of other powerful subglacial geothermal areas.

(iii) Preservation of hyaloclastite mountains formed in subglacial eruptions is dependent on the flow dynamics of the overlying glacier, and on the rate at which the edifice alters from an initial pile of breccias and tephra to consolidated rock. The eruption at Gjálp in 1996 offered a unique possibility to study the development of such a mountain. Repeated surveying of ice surface geometry, measurement of inflow of ice, and a 2-D ice flow model have been combined to derive a heat output record for 1996-2005 for the hyaloclastite ridge formed in the 13 days long eruption. About two thirds of the total magmatic heat of 1.5×10^{18} J were released during the eruption with extremely high heat output of order 10^6 MW. A rapid decline in heat output followed, reaching ~2500 MW by mid 1997. It remained similar until mid 1999 but declined to 700 MW in 1999-2001. Since 2001 heat output has been insignificant, probably of order 10 MW. The heat output history can be reconciled with the gradual release of the 5×10^{17} J thermal energy remaining in the Gjálp ridge at the end of the eruption, assuming single-phase liquid convection in the cooling edifice. The average temperature of the edifice is found to have been approximately 240 °C at the end of the eruption, dropping to ~ 130 °C after 7 months and reaching ~ 38 °C in 2001. Although an initial period of several months of very high liquid permeability is possible, the most probable value of the permeability from 1997 onwards is of order 10^{-12} m^2. This is consistent with consolidated/palagonitized hyaloclastite but incompatible with a pile of unconsolidated tephra. The probable permeability values may indicate that palagonitization had advanced sufficiently in the first 1-2 years to form a consolidated hyaloclastite ridge, resistant to erosion. No ice flow traversing the Gjálp ridge has been observed, suggesting that it has effectively been shielded from glacial erosion in its first 10 years of existence.

Ágrip (in Icelandic)

Jöklar eru algengir í hlíðum eldfjalla og hlutar eldvirkra svæða eru sumstaðar huldir ís. Dæmi um slíka staði eru ísfylltar öskjur í Andesfjöllum og Alaska, hlutar Suðurskautslandsins og gosbeltin á Íslandi þar sem eldvirkni og jarðhiti er mikill, einkum undir Mýrdalsjökli og Vatnajökli. Eldvirkni og jarðhiti undir jöklum orsaka jökulhlaup, móbergsfjöll myndast í eldgosum og vatn við botn jökuls getur valdið auknu ísskriði. Í þessari ritgerð eru kynntar niðurstöður rannsókna á samspili jökla og jarðhita. Markmið verkefnisins má flokka í þrennt: (i) Nákvæm hermun ísflæðis að jarðhitasvæðum undir jökli með tölulegum aðferðum. (ii) Hönnun aðferða til að meta eiginleika jarðhitasvæða undir jökli út frá ísflæði á yfirborði. (iii) Mat á breytingum með tíma á varmastraum frá hryggnum sem myndaðist undir Vatnajökli í Gjálpargosinu 1996. Helstu niðurstöður verkefnisins eru eftirfarandi:

(i) Smíðað hefur verið tölulega flæðilíkanið Icetools. Styrkur þess er að það leysir Stokes jöfnuna fyrir ísflæði án þeirra nálganna sem algengast er að gera í jöklafræði. Líkanið má því nota til að reikna í tveimur víddum þróun jökulyfirborðs í sigkötlum eða á öðrum viðlíka stöðum þar sem verulegar breytingar verða með tíma. Líkanið var prófað fyrir tvö tilfelli: (1) Flæði íss niður jafnt hallandi plan. (2) Flæði yfir ójöfnu með lögun Gauss-ferils, en það tilfelli hefur ekki verið kannað áður með tölulegum reikningum. Reikningar fyrir bæði tilfellin falla vel að fræðilegum lausnum og ná æstæðu ástandi. Fjallað er um þessar niðurstöður í 2. kafla ritgerðarinnar.

(ii) Líkanið var notað til að rannsaka eiginleika jarðhita sem myndaði 100-150 m djúpa, ílanga sigdæld undir norðaustanverðu Grímsfjalli á árunum 1998-2004. Reikningarnir leiddu í ljós að þegar meta á varmaflæði frá hitasvæði undir jökli út frá þróun sigdældar, skiptir gildið á flæðistuðlinum A í lögmáli Glens fyrir ís miklu máli. Sé flæði íssins inn í dældina ekki tekið með í reikninginn er varmaflæðið vanmetið um 15-75%. Lægri talan á við um stífan ís en það hærra fyrir mýkri ís (eiga við flæðistuðul á bilinu $10-68\times10^{-16}\mathrm{s}^{-1}\mathrm{kPa}^{-3}$). Þessar tölur samsvara varmaflæðinu 260-390 W m^{-2} í tilfelli mælisvæðisins í Grímsvötnum. Líklegasta gildi á varmaflæðinu er talið 280 W m^{-2} sem svarar til flæðistuðulsins $A = 23 \times 10^{-16}\mathrm{s}^{-1}\mathrm{kPa}^{-3}$. Heildarafl jarðhitans undir dældinni er talið hafa

verið 250-300 MW, u.þ.b. 10% af heildarvarmaafli Grímsvatna á tímabilinu. Varmaflæðið undir dældinni er af sömu stærðargráðu og finnst á öðrum öflugum jarðhitasvæðum. Fjallað er um þessar niðurstöður í 3. kafla.

(iii) Afdrif móbergsfjalla sem myndast í eldgosum undir jökli ráðast annarsvegar af því hve hratt gosefnin ummyndast úr sundurlausri hrúgu gosefna yfir í þétt móberg, og hinsvegar af því hve fljótt ís fer að skríða yfir fjallið og rjúfa það niður. Gosið í Gjálp í Vatnajökli í október 1996 myndaði fjallshrygg undir jöklinum og bauð því upp á einstakt tækifæri til að kanna þróun slíkra fjalla. Notaðar hafa verið endurteknar mælingar á lögun og stærð sigdældar, mælingar á skriði íss inn til hennar og tvívítt líkan af ísflæði til að finna varmastraum frá fjallinu á tímabilinu 1996 til 2005. Heildarvarmi sem barst með gosefnum var $(1.5 \times 10^{18}$ J) en um tveir þriðju hlutar varmans losnuðu og nýttust til ísbræðslu í gosinu 1.-13. október 1996. Mjög hraður flutningur varma frá gosefnum til íss mældist í gosinu, enda var varmaflif um 10^6 MW. Að gosi loknu lækkaði varmastraumurinn hratt og hafði náð $\sim$2500 MW í júní 1997 og hélst hann svipaður í tvö ár. Á tímabilinu 1999-2001 lækkaði aflið í $\sim$700 MW og eftir 2001 hefur það verið óverulegt, líklega af stærðargráðunni 10 MW. Hægt er að skýra þessa þróun með losun þeirrar varmaorku sem eftir var í fjallinu (5×10^{17} J) með hræringu jarðhitavatns að loknu gosi. Meðalhiti fjallsins í goslok er talinn hafa verið $\sim$240 °C. Í júní 1997 er hann talinn hafa verið $\sim$130 °C og hafði fallið í $\sim$38 °C árið 2001. Varmaflutningur í jarðhitasvæði er mjög háður lekt bergsins og þróun varmaaflsins í Gjálp gefur vísbendingar um lektina. Mögulegt er að fyrstu mánuðina hafi lekt gosefnanna verið mjög mikil. En frá og með miðju ári 1997 er líklegasta lekt í fjallinu af stærðargráðunni 10^{-12} m^2. Þessi lekt samræmist föstu móbergi en er allt of lág fyrir óharðnaða gjósku. Þetta er vísbending um það að móbergsmyndun hafi á 1-2 árum verið það hröð að fjallið hafi á þeim tíma orðið að móbergi að stórum hluta. Jökulrof slíks móbergsfjalls yrði mun hægvirkara en rof á haug af ósamlímdri gjósku. Mælingar á ísskriði sýna að á tímabilinu 1996-2005 skeið ís aðeins inn í Gjálpardældina en ekki yfir fjallið. Þetta bendir til þess að fjallið hafi í raun verið í skjóli fyrir rofi fyrstu 10 árin meðan bergið harðnaði og þéttist. Gjálparfjallið virðist því komið til að vera. Engin merki hafa sést um að vatn safnist fyrir á gosstaðnum í Gjálp. Það er því ósennilegt að stór jökulhlaup geti komið frá slíkum gosstöðvum undir jökli löngu eftir að eldgosi lýkur. Fjallað er um þessar niðurstöður í 4. kafla.

Acknowledgments

First and foremost I would like to express my deepest gratitude to my supervisor, Magnús Tumi Guðmundsson, for the continuous support and stimulating discussions throughout the years I was working on this thesis. He introduced me to the fascinating world of volcanoes, took my along on exciting glacier field trips, enabled me to explore freshly formed eruption sites and opened my eyes to the thrilling subject of volcano-ice interaction. Whenever time was needed to complete a paper or discuss new research results, he could spare a few minutes which commonly were extended into the hours range. His generosity in ideas and exchange of views is unmatched.

Special thanks go to Finnur Pálsson and Þórdís Högnadóttir for the help and support with so many big and small problems along the way. I am grateful to have had them as colleagues and close friends during my time at the Institute of Earth Sciences. Both warmly welcomed me at the Institute and made me feel at home right from the start. We also shared many glorious moments on the glaciers together.

Guðfinna Aðalgeirsdottir, G. Hilmar Guðmundsson and Antoine Pralong are thanked for sharing valuable insights in numerical glacier modeling, which were very helpful in the early development stage of the Icetools code.

It was a great pleasure for me to join the glacier field campaigns throughout the last three years and being able to actively participating in them. Many good friendships were formed during that time. I would like to name a few of those lion-hearted people who conquer the everlasting ice on a yearly basis[1]: Eyjólfur Magnússon, Þorsteinn Jónsson, Sveinbjörn Steinþórsson, Björn Oddsson, Katrín Auðunardóttir, Hrafnhildur Hannesdóttir, Hálfdán Ágústsson, Jósef Hólmjárn, Ágúst Hálfdánsson, Þóra Karlsdóttir, Magnús Þór Karlsson, Erik Sturkell and Sjöfn Sigsteinsdóttir. It was a great pleasure to work with you all!

The field campaigns on Vatnajökull during the last 13 years have been supported by the National Power Company of Iceland (Landsvirkjun), the Icelandic

---

[1]This list is by no means complete nor does it follow any particular order. If I should have forgotten somebody, please accept my apologies for that and consider yourself included in this list.

Chapter 1

Introduction

This doctoral thesis is based on the following papers, which are included as chapters:

- **Jarosch, A. H.**: *Icetools: a Full Stokes Finite Element Model for Glaciers*, Computers & Geosciences, 2007. (in review) **Chapter 2**.

- **Jarosch, A. H.**, Gudmundsson M. T.: *Numerical studies of ice flow over subglacial geothermal heat sources at Grímsvötn, Iceland, using Full Stokes equations*, Journal of Geophysical Research, Earth Surface, 2007, 112, F02008, doi:10.1029/2006JF000540 **Chapter 3**.

- **Jarosch, A. H.**, Gudmundsson, M. T., Högnadóttir, Þ, Axelsson, G.: *Progressive cooling of the hyaloclastite ridge at Gjálp, Iceland, 1996 - 2005*, Journal of Volcanology and Geothermal Research, 2007. (submitted) **Chapter 4**.

The primary aim of the work presented is to gain deeper understanding of the interaction between subglacial heat sources and the glacier ice above, generally termed volcano-ice interaction. Common types of heat sources encountered are subglacial geothermal systems of different sizes as well as volcanoes or volcanic systems buried underneath glaciers or ice sheets. Previously reported sites featuring subglacial heat sources include several ice-filled calderas around the world (e.g. Clarke et al., 1989; Major and Newhall, 1989) and the large ice caps in Iceland, especially Vatnajökull and Mýrdalsjökull (e.g. Björnsson, 1988; Björnsson and Gudmundsson, 1993; Gudmundsson et al., 1997, 2004). There is also evidence of an active volcanic area underneath the West Antarctic Ice Sheet, near the Whitmore mountains (Blankenship et al., 1993; Behrendt et al., 1994, 1995). Moreover, volcanic regions at high and middle latitude were ice covered during the Pleistocene and earlier glaciations (e.g. Velichko et al., 1997; Hickson, 2000).

Figure 1.1: The last Grímsvötn eruption on November 2nd, 2004. A satellite image of the eruption is shown in Fig. 1.5.

1.1   Research objectives

By focusing on the effects of geothermal heat sources on ice dynamics in temperate glaciers, where ice temperatures are at the pressure melting point, the following research objectives are investigated:

(i) Accurate numerical simulation of ice dynamics above subglacial heat sources with a state of the art ice flow model.

(ii) Development of methods to infer subglacial heat source parameters by using glacial surface data: e.g. ice surface velocities, surface mass balance records and surface depression volume changes.

(iii) Estimation, construction and analysis of the heat output record from the subglacial hyaloclastite ridge (edifice) formed in the 1996 Gjálp eruption, Vatnajökull, Iceland.

Earlier work on the interaction between subglacial heat sources and ice has not utilized numerical ice models to investigate quantitatively the ice dynamics involved. Until now, published research has used calorimetric work to study heat output from subglacial geothermal areas and volcanoes, notably at Grímsvötn

Figure 1.2: The Gjálp eruption on October 3rd, 1996. Photo: Magnus T. Gudmundsson.

and Gjálp (see section 1.3.2 and Figs. 1.1, 1.2 and 1.3). In recent years, considerable advances have been made in ice flow modeling, both on the scale of ice sheets / ice caps, and on a more local scale, for small parts of a glacier (see section 1.3.1). The use of modern ice flow models in the study of volcano-ice interaction has become more feasible. A better understanding of the processes involved in such an interaction has a very practical dimension. As heat is transfered from the subglacial heat source to the ice, meltwater is created, which can cause jökulhlaups and lahars. These generally catastrophic events pose major threats in some volcanic regions, including Iceland (e.g. Major and Newhall, 1989; Björnsson, 2003; Gudmundsson, 2005).

The ice-covered volcanic regions in Iceland offer excellent opportunities to study the interaction of glaciers with subglacial heat sources at various scales. Subglacial eruptions are more common in Iceland than elsewhere on Earth (e.g. Larsen, 2002; Gudmundsson, 2005; Thordarson and Larsen, 2007) and the country has many subglacial geothermal areas of varying heat output and size (e.g. Björnsson, 1988; Gudmundsson et al., 2007). The western part of Vatnajökull hosts the highly active Grímsvötn central volcano (Fig. 1.1) and the recent eruption site of Gjálp (Fig. 1.2). This area offers an unique variety of settings ranging from small ice surface depressions due to minor subglacial geothermal activity

to large volcanic eruptions. Field data from this area collected over the last 10 years of intense volcanic and geothermal activity forms an important part of this study.

1.2 Geological framework

Vatnajökull, with an area of 8100 km^2, is the largest glacier in Iceland and covers $\sim$8 % of the country. Most parts of the glacier are between 400 and 700 m thick (Björnsson, 1988). Several volcanic systems, which typically consist of a central volcano and a corresponding fissure swarm, are partly covered by the western region of Vatnajökull (Björnsson and Einarsson, 1990). Those volcanic systems belong to the Eastern Volcanic Zone, the southeastern section of the rather complex active plate boundary between the American and the Eurasian plate, which crosses Iceland from southwest to northeast (Sigmundsson, 2006, Chapter 3)(Fig. 1.3b). The major central volcanoes in this region rise some 1000 m above the surroundings, have diameters of 15-20 km and calderas in their centers. Two prominent central volcanoes within Vatnajökull are Bárðarbunga and Grímsvötn. Grímsvötn is more active and contains one of the most powerful geothermal areas in Iceland (Björnsson, 1988; Björnsson and Gudmundsson, 1993). Due to the geothermal activity in Grímsvötn, a large depression has formed within Vatnajökull, a prominent surface feature of the ice cap. Meltwater created by the geothermal activity accumulates within the caldera and a subglacial lake is a persisting feature of Grímsvötn, which drained in jökulhlaups every 4-6 years prior to the 1996 Gjálp eruption (Thorarinsson, 1974; Gudmundsson et al., 1995)(Fig. 1.4).

The western part of Vatnajökull has been identified as the region with the highest eruption frequency in Iceland (Larsen et al., 1998). This high level of activity in the region is probably connected to its location above the postulated center of the Iceland mantle plume (Wolfe et al., 1997). The Grímsvötn volcanic system has been without a doubt the most active one in historical times (since about 900 A.D.). The number of confirmed eruptions in the last 800 years is about 60 (Larsen et al., 1998). The Bárðarbunga-Veiðivötn system with at least 17 eruptions in the last 800 years, has also been highly active.

Numerous ridges and mountains beneath the western part of Vatnajökull are considered to have formed during subglacial volcanic activity. They are located within the central volcanoes as well as on their associated fissure swarms (Björnsson, 1988; Björnsson and Einarsson, 1990; Björnsson et al., 1992; Langley, 2000). Exact locations of historical eruption sites within Vatnajökull are generally unknown, despite the fact, that dates have been established for many of these eruptions (Thorarinsson, 1974). For one historical eruption outside the central volcanoes, the location is well established. In 1938, a subglacial fissure eruption formed a short ridge with a volume of 0.3-0.5 km^2 north of Grímsvötn (Gudmundsson
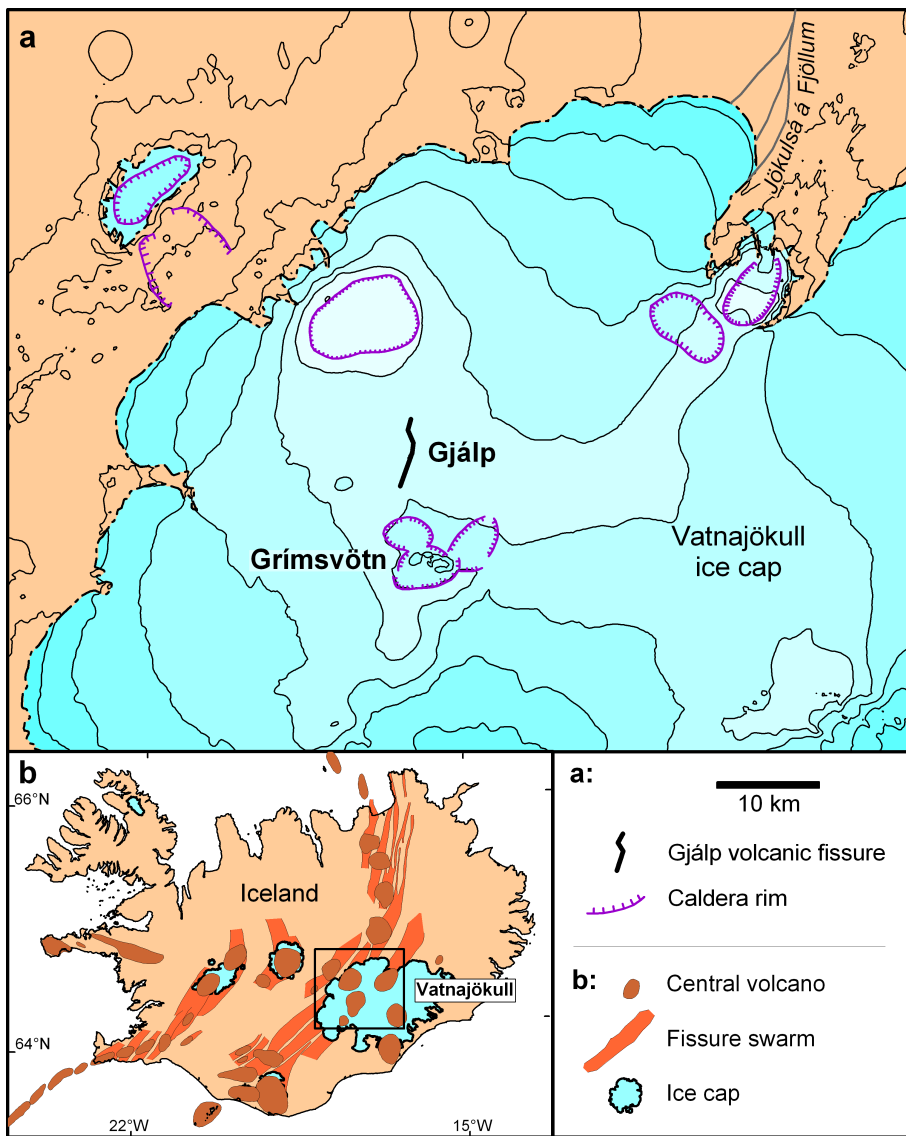
Figure 1.3: Location map. (a) A detailed map of the Vatnajökull ice cap, the Gjálp volcanic fissure and the Grímsvötn volcanic system. (b) An overview of the volcanic systems of Iceland (Einarsson and Sæmundsson, 1987).
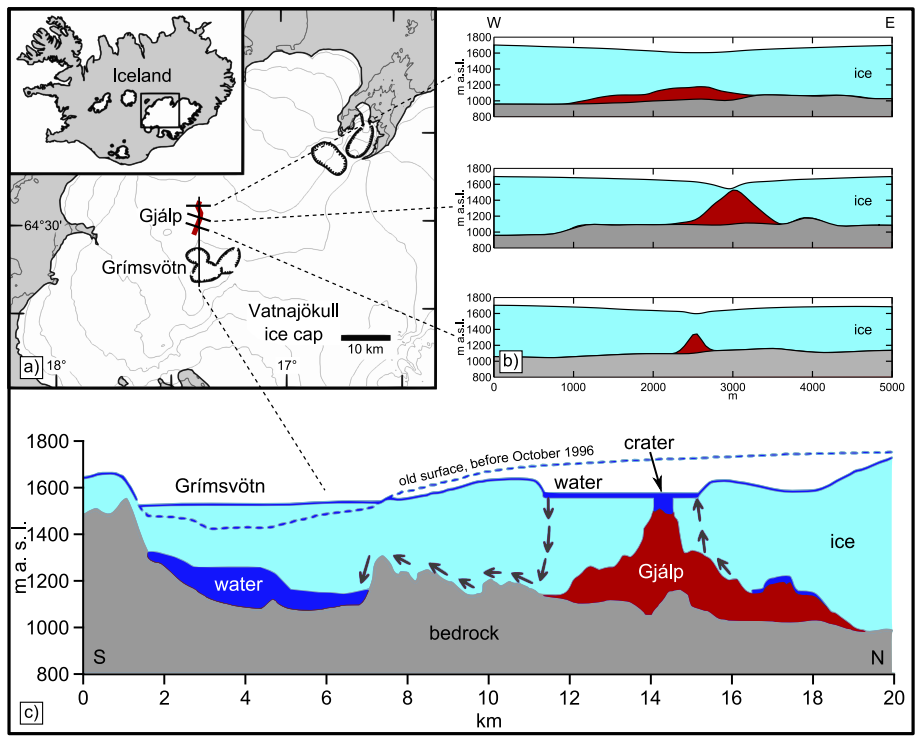
Figure 1.4: Four sections across the Gjálp - Grímsvötn area. (a) Location map of the cross-sections. (b) Three west-east transecting profiles of Gjálp and (c), a north-south transecting profile of Gjálp and Grímsvötn (Gudmundsson et al., 2004). Cross-section (c) displays the subglacial conditions right after the 1996 Gjálp eruption with black arrows indicating possible water flow paths.

and Björnsson, 1991; Björnsson, 1988). The exact timing of the event is not well established but large depressions in the ice surface were observed from the air at the end of May 1938. Other recent eruptions within the western part of Vatnajökull include the 1998 and 2004 (Fig. 1.1) eruptions within the Grímsvötn caldera and the 1996 Gjálp eruption (Fig. 1.2).

1.3 Previous research

"If I have seen further it is by standing on ye shoulders of Giants"
Isaac Newton, 1676.

In this section an overview is given of previous research connected to the themes of this thesis. Each major subject is presented in a separate subsection.

1.3.1 Full Stokes ice models

The flow of ice is principally formulated with the following physical model. Generally the Stokes equation (e.g. Pozrikidis, 1996) is used to describe the laminar nature of ice flow in combination with a non-linear, stress dependent viscosity (Glen, 1955; Nye, 1957). To simulate ice flow numerically, most ice flow models use approximations to the Stokes equation. Since the formulation of the shallow ice approximation (SIA) (Hutter, 1983), which is most commonly used, several other approximations to the Stokes equation have been suggested in the literature. Those approximations generally simplify the strain rate definition and drop terms from the momentum balance equation. The approach of using the Stokes equation without any approximations or simplification is commonly referred to as the "Full Stokes" approach by glaciologists. In former times, the need for such approximations arose from computational limitations. Generally the numerical solution to non-linear Stokes problems is a computationally intensive task, but with the recent advances in computer technology, solving the Stokes formulation for ice has become more and more feasible. An excellent overview in combination with a numerical comparison of approximations used in glaciology is given by Hindmarsh (2004). The Full Stokes formulation for ice is discussed further in Chapter 2 and 3.

Several direct comparisons between the SIA and the Full Stokes approach have been carried out (e.g. Jóhannesson, 1992; Gudmundsson, 2003a). The need for more complete ice flow models has become obvious and more and more components of the stress tensor were included in the formulation as time progressed. These newer generations of ice flow models, often called higher order models, include longitudinal stress gradients. In glaciology, longitudinal stresses refer to all components of the stress tensor except the two horizontal plane shear components. Some examples of modern three-dimensional ice sheet models including

Figure 1.5: Vatnajökull with ash deposits from the Grímsvötn eruption in November 2004. Image courtesy Jacques Descloitres, MODIS Rapid Response Team, NASA-Goddard Space Flight Center (http://visibleearth.nasa.gov/).

longitudinal stresses are found in Hubbard et al. (1998), Pattyn (2003) and Saito et al. (2003).

Full Stokes models became popular and feasible with the increased availability of computational power. Modern applications of Full Stokes ice models are manifold. Early applications have included the study of glacier sliding over sinusoidal bed geometries (Gudmundsson, 1994), or the study of confluence regions in alpine glaciers (Gudmundsson, 1999). Mechanisms of fast ice flow in the Jakobshavn Isbrae glacier, Greenland have been investigated using this type of models (Luthi et al., 2002). The response of alpine glaciers to climate changes (Leysinger Vieli and Gudmundsson, 2004) has been studied in detail as well as the instability of hanging glaciers (Pralong and Funk, 2006). The response of glacier surfaces to sinusoidal bed disturbances has been researched in great detail using a two-dimensional, Full Stokes ice model (Raymond and Gudmundsson, 2005). A recent study of internal layer architecture in ice sheets also utilized a Full Stokes ice model (Hindmarsh et al., 2006).

1.3.2   Vatnajökull

A substantial amount of research on the Vatnajökull ice cap (Fig. 1.5) and it's subglacial volcanic systems has been carried out over the last 70 years. One reason for the interest in this region arises from the complex interactions between ice and volcanoes and the various phenomena caused by this special interrelationship.

Important radio-echo soundings have been carried out between 1978 and 1990, revealing the ice surface and bedrock topography of Vatnajökull in considerable detail (Björnsson, 1988; Björnsson and Einarsson, 1990; Björnsson et al., 1992).

Early attempts to estimate heat output from the Grímsvötn region were already made in 1965 (Sigvaldason, 1965). Applications of calorimetry to study the heat output of Grímsvötn was established by Björnsson (1974, 1988). Björnsson and Gudmundsson (1993) presented a record of heat release from the Grímsvötn geothermal system over a 69 year period (1992-1991). In late 1996 the focus shifted towards Gjálp, whose eruption in October 1996 was the first substantial such event in Iceland in 58 years. First research results including a heat output record over the first 90 days after the eruption were published a year later (Gudmundsson et al., 1997). The Gjálp eruption site has been the subject of many research projects focusing on new insight into subglacial volcanology as well as ice dynamics. Remote sensing methods have been used to understand the ice movements around the freshly formed surface depression and to deduce heat flux values (Björnsson et al., 2001; Gudmundsson et al., 2002b). Important contributions to the understanding of subglacial eruptions and heat transfer mechanisms have been made by Gudmundsson (2003b) and Gudmundsson et al. (2004).

Subglacial hydrology in Vatnajökull has been the subject of many scientific papers, especially jökulhlaups, which have been investigated in great detail (Björnsson, 1974, 1975, 1977, 1988, 2003; Flowers et al., 2004; Jóhannesson, 2002; Thorarinsson, 1974). The large-scale subglacial drainage structure of the whole Vatnajökull ice cap has been studied numerically (Flowers et al., 2003).

Ice dynamics within Vatnajökull have already been simulated numerically. The fate of the ice cap in connection to climate changes has been simulated with finite difference models (Aðalgeirsdóttir et al., 2005, 2006; Marshall et al., 2005). A surface depression formed during the large jökulhlaup after the 1996 Gjálp eruption. The response of the glacier surface to this disturbance has been modeled using a finite difference as well as a Full Stokes finite element model (Aðalgeirsdóttir et al., 2000). The influence of subglacial geothermal activity on ice dynamics around two permanent ice cauldrons (Skaftárkatlar) within Vatnajökull has been observed by satellite radar interferometry and a simple model was applied (Jónsson et al., 1998).
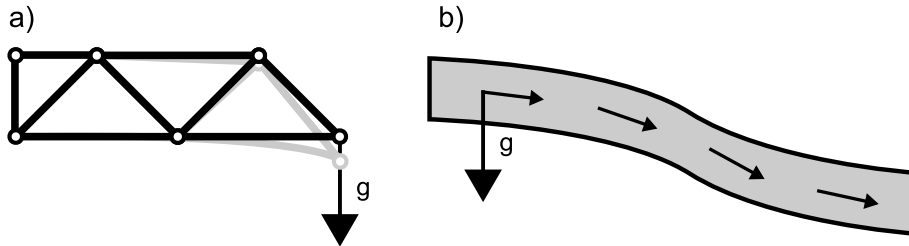
Figure 1.6: (a) An example of a discrete system: a truss. A possible deformation due to gravity g, is indicated in gray. (b) An example for a continuous system: flow of a liquid through a pipe, or ice down a slope, driven by gravity g. Arrows indicate flow direction.

1.4 The finite element method

While attempting to understand the behavior of a highly complex system, one often faces difficulties in analyzing the complete interaction in one operation. To overcome this fundamental problem scientists and engineers often use a simple and yet powerful approach. The system is subdivided into individual components or "elements" whose properties and behavior can be easily understood. To study the behavior of the whole system, it is rebuilt from such "elements" making it possible to tackle the complexity.

In many situations a system is sufficiently represented by a model that is built by a finite number of well-defined components. These systems are termed discrete. Typical examples of discrete systems like trusses and load-bearing structures are found in construction engineering (Fig. 1.6a). In other systems the subdivision into a finite number of components is not sufficient to describe the system and thus the subdivision is continued indefinitely. These systems can only be represented by using the mathematical tool of an infinitesimal, which leads to partial differential equations (PDE) or equivalent statements to describe them. These systems are commonly termed continuous. For example fluid dynamics deals with continuous systems, such as the flow of a liquid through a pipe (Fig. 1.6b).

Nowadays discrete systems with large numbers of elements can be solved readily due to the rapid advances in computer technology. Continuous problems can only be solved exactly with mathematical manipulation, since the number of elements is infinite and the capacity of computers is finite. Generally mathematical methods for solving continuous systems exactly are only available for oversimplified cases.

Over the years, scientists, mathematicians and engineers have developed various methods to solve realistic types of continuous problems. All proposed meth-

ods are based on the idea that the continuum (continuous system) can be subdivided into a finite number of components which assemble a model that approximates the initial system. This process of subdividing the continuum is called discretization. All discretization methods involve approximations which are assumed to approach the real continuum solution as the number of elements (components, discrete variables) increases. An investigation on how well this assumption is valid for the discretization method used in this thesis can be found in section 2.4.1.

Mathematicians have approached the problem of discretization more theoretically and developed general techniques that apply directly to the differential equations, e.g. the finite difference method (e.g. Richardson, 1910) or various weighted residual procedures (e.g. Gauss, 1809; Galerkin, 1923). Having said that, engineers have developed discretization methods based on analogies between real discrete elements and finite portions of a continuum. This approach is more intuitive and early examples can be found in the field of solid mechanics in the 1940s, where it was demonstrated that elastic continuum problems can be solved reasonably well by replacing small portions of the continuum with an arrangement of simple elastic bars (e.g. McHenry, 1943). The term "finite element" was first used by Clough (1960), who pioneered the conceptual and computational aspects of the finite element method. It was then, that the idea of a standard method, which can be applied to discrete systems, began to form. The implications of this new insight were of prime importance for a new conceptual approach to understand discrete systems as well as to develop a standard computational method to solve such problems.

Since those early days much progress has been made and nowadays both approaches, the pure mathematical and the intuitive engineering one, have been combined in a general discretization method for continuum problems based on mathematics. To establish this method, several independent approaches have been combined. Civil engineers calculated force displacement relationships for single elements and then interconnected those elements to form the structure of interest. The assembly followed a well defined procedure which established local equilibrium at each interconnection point or node between the elements. The resulting equations were solvable for the unknown displacement of the structure. Hydraulic engineers had to deal with networks of hydraulic conduits. They first developed the relationship of fluxes and potentials for individual elements and than assembled the system by imposing continuity of flow at each node. Electrical engineers followed a similar approach.

It was realized that those independent approaches followed a standard pattern and that it was possible to formulate a standard method applicable to a large variety of discrete problems. Therefore it is possible to define a standard discrete system (standard discrete problem) which is solvable with a standard mathematical method. This method was termed "finite element method" and can be defined
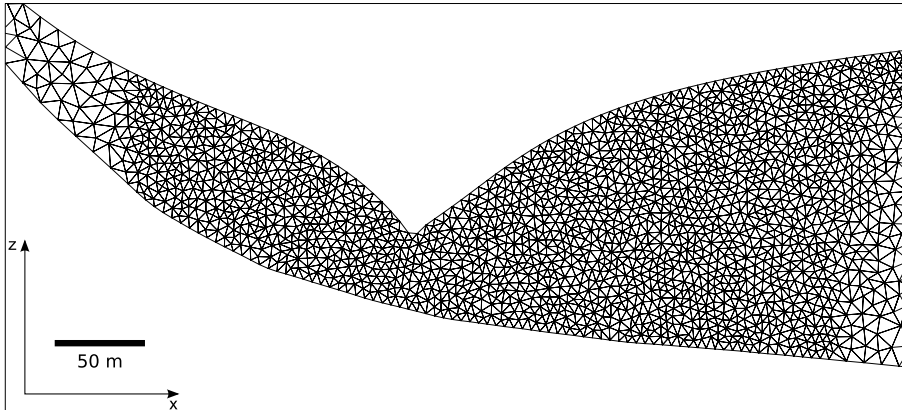
Figure 1.7: The central part of the triangular mesh used to model the ice depression in Chapter 3. Note the change in element size on the outer parts of the mesh.

as a method of approximation to continuum problems where (Zienkiewicz et al., 2005):

(1) the continuum is divided into a finite number of parts (elements), the behavior of which is specified by a finite number of parameters, and

(2) the solution of the complete system as an assembly of its elements follows precisely the same rules as those applicable to standard discrete problems.

The assembly of elements describing a continuous system is often called "mesh" which forms the base of the computational procedure solving the problem. Elements within a mesh can have different shapes corresponding to different dimensions, e.g. triangular (2D), quadrilateral (2D), tetrahedral (3D) and hexahedral (3D). A comparison between triangular and quadrilateral meshes is given in section 2.4.1. Fig. 1.7 displays the central part of the triangular mesh used in Chapter 3 and demonstrates different element sizes within one mesh.

The "finite element method" is a well suited method of approximation to a large number of continuum problems and allows a numerical solution of such problems in an elegant and unified way. The mathematical details of this method are presented in a clear and comprehensive way by Zienkiewicz et al. (2005), who also gives a detailed historical overview of the method. How this method has been used in this thesis by applying it to the problem of ice flow and deformation is presented in Chapter 2.

1.5 Outline of work

In the following subsections an outline is given on why the research objectives were chosen and how they have been investigated in the corresponding research papers. Results can be found either in the abstract of this thesis or within the chapters dedicated to the papers.

1.5.1 Objective i. Numerical simulation of ice dynamics above subglacial heat sources

An open source ice flow model has been implemented based on the Full Stokes formulation of ice and the finite element method to gain new insight into the behavior of glacier systems with subglacial heat sources.

During the development of this software, termed Icetools, several new contributions to modern, numerical ice flow modeling have been made. For the first time a Full Stokes ice model has been applied to the transient evolution of surface depressions formed over subglacial heat sources (Chapter 3). Also, the temporal response of a glacier surface to a Gaussian shaped bed disturbance has been studied with this model, a subject not studied numerically so far (Chapter 2). Details about the software, along with numerical performance tests is presented in Chapter 2.

1.5.2 Objective ii. Development of methods to infer subglacial heat source parameters from glacial surface data

Two main Icelandic, subglacial volcanic systems, Grímsvötn and Gjálp (Fig. 1.3), have been closely monitored over a prolonged period of time by the Institute of Earth Sciences, University of Iceland. The resulting extensive data set inspired the idea of utilizing glacier surface data to infer subglacial heat source properties in a more complete way than done before. The principal methodology used in this approach can be briefly outlined as follows.

The presence of subglacial heat sources leads to significant changes in the surface geometry of the overlying ice, namely the formation of surface depressions and crevasses. Closely monitoring the formation and evolution of such surface depressions is the starting point for inferring heat source properties, e.g. heat flux values, energy output with time, etc. At first sight, the fact that the heat source is buried underneath ice appears to be disadvantageous. However this circumstance can be used in a simple and ingenious way to measure the energy output from such a heat source. Most of the energy released will be used to melt ice, hence the total mass of ice melted over a given period of time can be used

to calculate the energy released during that period. Therefore focus is set upon estimating the total mass of ice melted.

As simple as this approach may appear, a closer investigation of the dynamics in such an interacting system (ice - heat source) reveals its complex interrelations. It will be demonstrated in Chapter 3, that simply measuring the volume changes of the surface depressions for estimating the total mass of melted ice is not sufficient to obtain accurate results unless complete drainage basins with known surface mass balance are studied. In the general case, a detailed study of all mass movements (mass fluxes) within the system is essential for estimating the heat source parameters of interest. The application of the newly developed numerical ice flow model on a region in Grímsvötn, which features a subglacial, geothermal heat source, led to various new insights on the behavior of such complex systems. Details of the findings gained from this study are presented in Chapter 3.

1.5.3 Objective iii. Reconstruction of the heat output record from the Gjálp ridge

The 1996 Gjálp eruption within Vatnajökull (Fig. 1.2 and 1.3) played an important role in the process of understanding subglacial eruptions. It was the first significant eruption within a large ice cap to be monitored in any detail. A considerable amount of new insights on processes occurring in subglacial eruptions under temperate glaciers, gained from the Gjálp observations, has already been published (see section 1.3). The reconstruction of the heat output record of the Gjálp edifice between 1996 and 2005 represents a major step forward towards understanding the formation and preservation of hyaloclastite ridges within glaciers.

Tuyas (table mountains), hyaloclastite ridges and sheets are common types of morphologies formed during subglacial eruptions (e.g. Mathews, 1947; Jones, 1969; Gudmundsson, 2005). During the Pleistocene, subglacial volcanic activity was a major, land-shaping process in Iceland, creating hyaloclastite ridges and tuyas. Those formations still dominate large parts of the present-day landscape. Subglacial volcanism turns out to be a major land forming process in other parts of the world as well, e.g in western Canada (e.g. Mathews, 1947; Hickson, 2000) or on the Antarctic Peninsula, where extensive hyaloclastite regions are found (Smellie, 1999).

A comparison of the Gjálp edifice and it's evolution with ridges formed during the Pleistocene under an ice sheet gives rise to several important questions. They can be formulated according to Gudmundsson et al. (2002a) as: (1) How well can the freshly formed Gjálp ridge, an initially unconsolidated pile of volcanic glass and tephra, withstand erosion from moving ice? (2) Can palagonitization prevent erosion and what is the rate of alteration for the Gjálp ridge? (3) What role does diversion of ice flow play in the preservation of the edifice? (4) Which general

conclusions about the behavior of subglacial as well as subaqueous eruptions can be made?

A pile of initially unconsolidated volcanic material at the base of a glacier, subjected to fast ice flow is expected to suffer heavy erosion. Therefore large parts of a volcanic edifice may be removed over a relatively short period of time. It has been suggested that such erosion processes have occurred in West Antarctica (Behrendt et al., 1995) and may have happened also in Iceland (Bourgeois et al., 1998). The Pleistocene ridges and tuyas found in Iceland are made of pillow lava, breccia and hyaloclastite, with hyaloclastite being the major component in some of the ridges (Schopka et al., 2006; Jakobsson, 1979). A common feature of these formations is that the volcanic glass has altered into palagonite, turning the loose pile of volcanic glass into consolidated rock (Jones, 1969; Jakobsson, 1979). This consolidation has been a key factor in preserving the edifices by making them resistant to glacier erosion. However, the rate at which this alteration occurs in the subglacial environment is unknown.

Another important aspect of studying the heat output record of the Gjálp edifice is to assess the potential for jökulhlaups to occur after the eruption. During the monitored period between late 1996 and mid 2005, no significant meltwater accumulation was detected at the Gjálp eruption site because the produced meltwater drained continuously into the Grímsvötn subglacial lake. Large jökulhlaups are highly likely to occur during or right after a subglacial eruption. The likelihood of jökulhlaup occurrence decreases rapidly after an eruption unless an unusual bedrock geometry favors water accumulation within the glacier.

Answers to the above formulated questions and the reconstructed heat output record of the Gjálp ridge are presented in Chapter 4.

To conclude this introduction, it should be mentioned that modern methods to increase declarative learning (Tucker et al., 2006) helped to improve and optimize the progress during finishing the presented thesis.

Chapter 2

Icetools: a Full Stokes Finite Element Model for Glaciers

Abstract

Detailed studies of glacier flow and deformation of ice require high resolution numerical modeling. The model presented in this paper, icetools, solves the Stokes equation including all components of the stress tensor, termed full Stokes, with the finite element method to enable such detailed studies. Icetools is capable of running in parallel on computational clusters providing the computing power for large scale simulations. Two different numerical tests were performed to demonstrate the capability of the model; (1) a comparison with the analytical solution for gravity driven plane flow down an inclined plane, and (2) flow over a Gaussian-shaped bed disturbance in comparison with the analytical transfer functions for this case. The second test involves time evolution of the surface geometry from an initially uniformly sloping surface. A linear rheology medium with a viscosity of 8×10^{13}Pa s and a non-linear medium with Glen rheology exponent $n = 3$ and rate factor of $A = 23 \times 10^{-16}$s^{-1}kPa^{-3} were studied. Both correlate well with the analytical solution and reach steady state, defined as when the maximum vertical movement drops below 5×10^{-5} times the mean ice thickness per year, after 282 years for the linear case and 135 years for the non-linear case respectively.

2.1 Introduction

To study the deformation and flow of ice sheets and glaciers with numerical models a variety of approximations have been suggested in literature. These approximations simplify the models by excluding different components of the stress tensor and hence reduce the computational power needed for the simulations. An evaluation of the different approximations (Hindmarsh, 2004) reveals the need for a numerical model solving the full set of equations and including all stress tensor components to study small scale phenomena within the ice.

A widely used approximation in glacier models is the shallow ice approximation (Hutter, 1983), which involves simplifying the strain rate definitions and excluding terms from the momentum balance equations. Including longitudinal stress terms and longitudinal stress gradient terms leads to more sophisticated models. In glaciology longitudinal stresses refer to all stress tensor components except the two horizontal plane shear components. Some examples of modern three-dimensional ice sheet models including longitudinal stresses are found in Hubbard et al. (1998),Pattyn (2003) and Saito et al. (2003). Examples for modern Full Stokes numerical ice models are Gudmundsson (1999), Raymond and Gudmundsson (2005) and Hindmarsh et al. (2006).

High resolution flow field calculations in a glacier are required to simulate evolution of the surface influenced by bedrock geometry as well as heat sources at the bedrock, closure of caves and tunnels with complex geometries within the ice or the behavior of crevasses. Including all stresses in the simulation by solving the Stokes equation and using Glen's constitutive equation (Glen, 1955; Nye, 1957) to account for non-linear, stress-dependent viscosity of ice proves to be a successful method to study small scale disturbances of the flow field (Hindmarsh, 2004).

A numerical model which solves the Stokes equation (e.g. Pozrikidis, 1996, p. 222) in three dimensions including the constitutive equation for ice has been developed and named icetools. To compensate the computational needs for such numerical models, icetools is capable of running in parallel on big computational clusters. For the convenience of running small test simulations a single machine version is also provided.

Icetools is developed as an open source project to provide the flexibility, availability and transparency required by the scientific community. Based on several open source software packages, icetools forms a numerical simulation suite for glaciers and ice deformation with the choice of two interfaces, either through Python or Matlab®. The icetools source code is available online[1] under the terms of the GNU General Public License and therefore enabling everybody to use and modify a free, parallelized Full Stokes ice flow model.

The numerical errors of the presented model are estimated by performing

---

[1]Icetools web page http://icetools.sourceforge.net

two independent benchmark tests. A comparison of numerical results for gravity driven plane flow down an inclined plane with the analytical solution for this case was carried out for different grid sizes and grid types to establish the error behavior of the model. The model was put to test again by comparing model runs for ice flow over a single, Gaussian-shaped bed disturbance, with analytical transfer functions describing the same problem (Gudmundsson, 2003a). To the knowledge of the author, this type of test experiment has not been examined before.

In a study of formation of ice surface depressions at the subglacial Grímsvötn volcano in Iceland (Jarosch and Gudmundsson, 2007), icetools was successfully used in modeling a complex ice flow problem.

2.2   Full Stokes Formulation for Ice

The governing equations in this formulation (e.g. Jarosch and Gudmundsson, 2007), which represent conservation of mass (eq. 2.1), linear momentum (eq. 2.2) and angular momentum (eq. 2.3) can be written as

$$\bigtriangledown \cdot \boldsymbol{v} = v_{i,i} = 0 \tag{2.1}$$

$$\sigma_{ij,j} + \rho g_i = 0 \tag{2.2}$$

$$\sigma_{ij} - \sigma_{ji} = 0 \tag{2.3}$$

with v_i the velocity vector, σ_{ij} the stress tensor, ρ the density of the material and g_i the gravitational acceleration vector. The flow of a medium described by eq. (2.1), (2.2) and (2.3) is know as Stokes flow, which describes an incompressible medium with constant viscosity in a laminar flow regime.

Based on the work of Glen (1955) the viscosity of ice is stress dependent. The constitutive equation of Glen describes the relation of the strain rates ($\dot{\varepsilon}_{ij}$) to the deviatoric stress ($\acute{\sigma}_{ij}$) as

$$\dot{\varepsilon}_{ij} = A\tau^{n-1}\acute{\sigma}_{ij} \tag{2.4}$$

with

$$\acute{\sigma}_{ij} = \sigma_{ij} - \frac{1}{3}\delta_{ij}\sigma_{ij} \tag{2.5}$$

the deviatoric stress tensor (δ_{ij} is the Kronecker delta). τ is a second invariant of the deviatoric stress tensor, n the Glen index and A represents a rate factor. In the formulation presented here, A is assumed to be constant. A depends on physical properties of ice (e.g. temperature, impurities etc.) and several higher

order models use a temperature dependent A (e.g. Pattyn, 2003; Saito et al., 2003). Icetools was developed for temperate ice at 0 °C and therefore A is treated as a constant, but it is of course possible to implement a temperature dependent A in icetools. For a more detailed description of the rate factor see e.g. Paterson (2001, p. 85).

Inverting eq. (2.4) gives

$$\sigma'_{ij} = A^{-\frac{1}{n}} \dot{\varepsilon}^{\frac{1-n}{n}} \dot{\varepsilon}_{ij} \tag{2.6}$$

with the effective strain rate as

$$\dot{\varepsilon} = \sqrt{\frac{1}{2} \dot{\varepsilon}_{ij} \dot{\varepsilon}_{ij}}. \tag{2.7}$$

Inserting eq. (2.6) into eq. (2.2) leads to the Stokes equation as

$$-\nabla \cdot [\eta(\nabla \boldsymbol{v} + \nabla \boldsymbol{v}^T)] + \nabla p = \rho \boldsymbol{g}, \tag{2.8}$$

using eq. (2.5), p denoting the pressure, and the viscosity defined as

$$\eta = \frac{1}{2} A^{-\frac{1}{n}} \dot{\varepsilon}^{\frac{1-n}{n}}. \tag{2.9}$$

2.3 Numerical Model

To solve the Full Stokes Formulation for a glacier the stress dependent viscosity of ice has to be taken into account. Therefore it is not sufficient to solve the governing equations with a constant viscosity. To include the constitutive equation of ice (eq. 2.4) in the model, an iterative method is used. This iterative method, shown in Fig. 2.1, makes it possible to use a standard code to solve the Stokes equation with the finite element method (e.g. Zienkiewicz et al., 2005). By iteration of the viscosity the rheology of a glacier is achieved.

The iterative steps of the model (cp. Fig. 2.1) are described in detail in the following subsection.

2.3.1 Initial Stokes Problem

The initial Stokes problem describes a Newtonian fluid with a constant viscosity of $\eta = 8 \times 10^{13}$ Pa s (Paterson, 2001, p. 98). This problem is solved for a given geometry and boundary conditions by using an open source code solver for finite element method problems called Getfem++[2]. Getfem++ is an advanced finite element method model software handling several different types of partial

---

[2]Getfem++ library. http://www-gmm.insa-toulouse.fr/getfem/
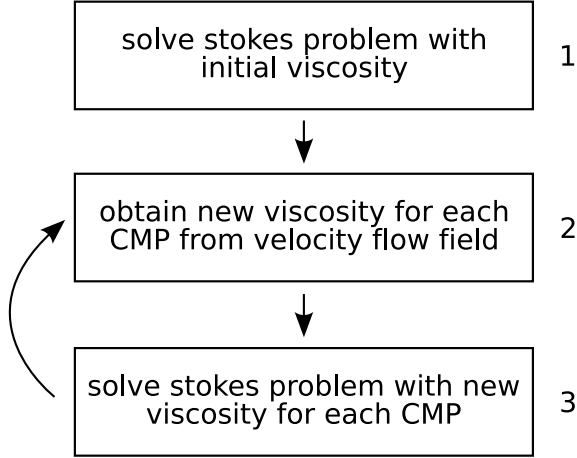
Figure 2.1: The iterative scheme of the model. CMP abbr. for computational mesh point or node.

differential equations, including Laplacian, linear elasticity and the Stokes equation. In the current version of icetools several modifications of the Getfem++ package were made which are described in subsection 2.3.5 below. After successfully solving the Stokes problem the result is a velocity vector field for the problem along with the corresponding pressure scalar field, which is known as a velocity-pressure formulation of the problem.

To create a computational mesh which describes the geometry for the Getfem++ package, the open source software Gmsh[3] is used along with some Python scripts written by the author. Gmsh is a state of the art mesh generator which primarily uses Delaunay triangulation and is therefore an ideal tool to prepare complex geometries for the simulation.

2.3.2   Calculation of the Viscosity

The obtained velocity vector field can be used to calculate the strain rates for the model on each node according to the equation

$$\dot{\varepsilon}_{ij} = \frac{1}{2}\left(v_{i,j} + v_{j,i}\right). \tag{2.10}$$

Using the inverse form of Glens constitutive equation (eq. 2.6), it is easy to calculate the new viscosity values on each node with eq. (2.9). The viscosity

---

[3]http://www.geuz.org/gmsh/

becomes singular as the deviatoric stress goes to zero (cp. eq. 2.4). To regulate the viscosity, the non-linear flow law was extended with a linear term as suggested by Hutter (1983):

$$\dot{\varepsilon}_{ij} = A(\tau^{n-1} + \tau_0^{n-1})\sigma'_{ij}. \qquad (2.11)$$

τ_0 is the crossover stress at which the linear and the exponential terms contribute equally to the total strain rate. Values for τ_0 are not very well constrained and range from 0 to 50 kPa (Pettit and Waddington, 2003). The crossover stress defines an upper limit for the viscosity in the model, which was chosen to be at $\eta_{max} = 1 \times 10^{15}$ Pa s and corresponds to $\tau_0 \sim 15$ kPa.

2.3.3 Viscosity Iteration

The viscosity scalar field obtained with the method described in subsection 2.3.2 is now the input viscosity on each corresponding node to a subsequent Stokes problem. The first loop inside the iteration process is now completed. By repeating step 2 and 3 in the iteration scheme, the viscosity of the glacier on each node converges towards a stress dependent viscosity according to the constitutive equation, eq. (2.4).

A quality parameter must be introduced to decide when a sufficient number of iterations has taken place to meet the required accuracy of the model. Such a parameter can be a predefined number of iterations, which was derived by comparing a simple model with an existing analytical solution, or the difference in the viscosity values from two successive iterations is lower than a given threshold.

This iterative approach to a non-linear viscosity is well established in Glaciology (e.g. Gudmundsson, 1999; Raymond and Gudmundsson, 2005).

2.3.4 Periodic boundary conditions

The concept of a periodic boundary condition (e.g. Allen and Tildesley, 1989, p. 24) for the inflow and the outflow of ice was modified and implemented in the model as described here. During the iterations in the model to obtain the viscosity given by Glen's flow law, eq. (2.4), the velocity values for the inflow and outflow boundary are calculated dynamically.

The initial Stokes problem with an initial viscosity starts with $|\boldsymbol{v}| = 0$ at the inflow and outflow boundary and after the solution for the velocity vector field is obtained, the values of the velocity along a cross section parallel to the boundary within the glacier are used as a boundary condition for the next iteration step. So during the iterations the model converts from a Newtonian fluid to a glacier and from a wall like boundary at the inflow and outflow to a flow-law driven boundary condition. This type of periodic boundary condition is demonstrated in Fig. 2.2 using the same geometry as in the first numerical test (cp. subsection 2.4.1), a

200 m thick, 2000 m long slab of ice on a 3° inclined plane. In this case the velocities at a horizontal coordinate x = 400 m and x = 1600 m are used as a boundary condition at x = 0 m and x = 2000 m in the next iteration step, see Fig. 2.2.

This approach assumes that the region of the glacier between the readout cross section and the actual boundary is repeated periodically and therefore extends the glacier to infinity outside the boundary. Assuming that the whole modeled domain is periodic and therefore using the outflow boundary as an inflow boundary would be another way to implement periodic boundary conditions. The use of two periodic boundary regions, one for the inflow and another for the outflow, allows the region in between the readout cross sections for the boundaries to be unique. This is convenient to model bedrock geometries which are not periodic, e.g. a unique bedrock anomaly.

Tests showed that the minimum distance from the boundary to the readout cross section of the velocity values should be at least double the mean ice thickness, cp. Fig. 2.2. Greater distances are producing a faster convergence to a solution whereas smaller distances seem to fail to converge sufficiently. The accuracy of this approach to a periodic boundary is tested in subsection 2.4.1.

2.3.5 Modifications of the Getfem++ package

The Getfem++ package provides a solver for the Stokes problem which is not capable to run in parallel at the time of the model development. When the Stokes problem grows bigger and the number of points in the mesh increases, this solver gets inefficient and slow. To optimize the solving of the Stokes problem and to make computation of the problem possible on a parallel cluster or symmetric multiprocessor computer, the Stokes solving routine was outsourced to a parallel mathematic library called PETSc[4] (Balay et al., 2004, 1997), which is also open source. An interface between the two packages was created and now all functions of the PETSc library can be used with Getfem++.

In the current state of development, icetools mainly uses Getfem++ through the Matlab® interface to assemble the stiffness matrix and formulate the linear system of equations for the Stokes problem and the chosen boundary conditions. This step is not parallel yet and utilizes the sequential algorithms of Getfem++. Since this is done in Matlab®, which is a procedural language, the object-oriented nature of Getfem++ is used within the Getfem - Matlab® interface. After the linear system of equations is assembled, it is solved using the PETSc interface. The PETSc library provides an extensive amount of direct and iterative linear equation solvers with the corresponding preconditioners. Icetools uses a parallel Uzawa type algorithm (Arrow et al., 1958; Zienkiewicz et al., 2005), which is also used in the sequential Getfem++ routine, to solve the system of linear equations

---

[4]PETSc web page. http://www-unix.mcs.anl.gov/petsc/
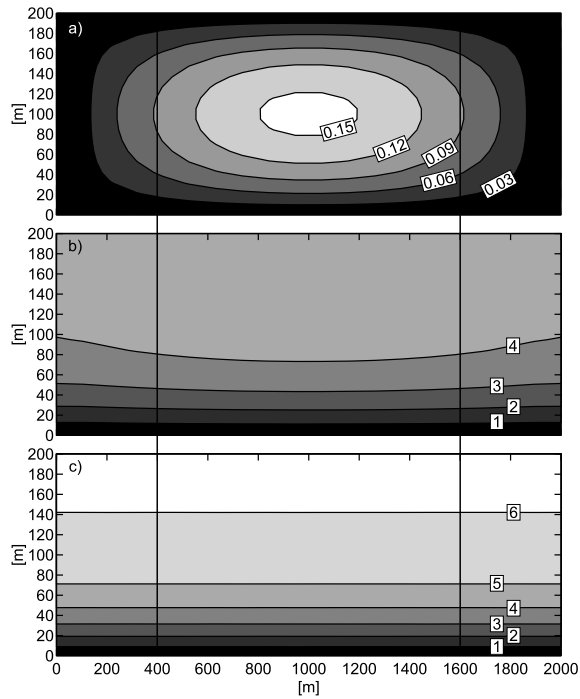
Figure 2.2: Convergence of the periodic boundary condition on a squared grid with 12.5 m grid size for in- and outflow on a tilted slab of ice. Vertical black lines mark the readout of the flow field to be used in the periodic boundary. a) the initial flow field with $|\boldsymbol{v}| = 0$ as an in- and outflow boundary. b) the flow field after 10 viscosity iterations and c) after 80 viscosity iterations. Contours are given in m year^{-1}.
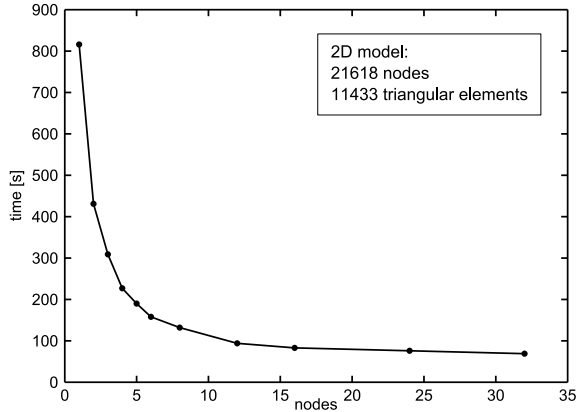
Figure 2.3: Time needed to solve a typical 2D problem as a function of number of computational nodes used.

resulting from the Stokes problem. This parallel solver utilizes the iterative GMRES method (Saad and Schultz, 1986) provided by the PETSc library. The Uzawa algorithm computes a residual in each iteration step which is used as a criterion for convergence of the solution. Other iterative or direct solvers can easily be used through the PETSc library interface.

A typical 2D problem with 21618 nodes and 11433 triangular elements was used to investigate how the parallel solver scales with the number of computational nodes in a cluster used. This test case used a linear rheology for ice. Fig. 2.3 shows the time needed to solve the problem with increasing number of computational nodes.

2.4 Numerical Tests

To test the numerical model and estimate the errors of the numerical results, two different kind of examinations can be done. Creating models for simple geometries which have an analytical solution and comparing the numerical results with these given analytical solutions gives an estimate of the absolute errors involved. Another, completely different type of error behavior in a finite element model emerges from the chosen grid size. Repeating the comparison of the model results with the analytical solution for a given setup with different grid sizes leads to an estimate of the relative errors caused by the different grid sizes.

Simple geometries for which analytical solutions exist feature symmetries which do not exist in real glaciers. Often the stress distribution within the simple model is far from a real case scenario. Therefore it is not possible to test the

model in a more general way than mentioned above and both types of tests are vital to understand the error behavior of the numerical model.

Two different, two-dimensional numerical tests were performed to investigate the error behavior of icetools. The Full Stokes formulation presented in section 2.2 is three-dimensional because icetools is capable of performing simulations in three and two dimensions. The Getfem++ library which is used by icetools is generic in the sense that there is no limitation in dimension or degree of the finite elements used in a simulation. This enables the user to simply switch between the two-dimensional and three-dimensional mode of icetools.

2.4.1   Gravity driven plane flow down an inclined plane

Flow of a slab of ice down an inclined plane driven by gravity has a simple analytical solution (Paterson, 2001, p.251) and can be used to test the numerical model. The geometry used here to evaluate the numerical model was a 200 m thick, 2000 m long slab of ice on a 3° inclined plane.

The analytical solution is used as an inflow / outflow boundary condition, (abbr.: a-bc) as well as the periodic boundary condition described in subsection 2.3.4 with a distance from the boundary to the readout section of 400 m (abbr.: p-bc). The results for three different grid sizes (50 m, 25 m and 12.5 m) are displayed in Fig. 2.4. All simulations are performed on an unstructured triangular and a squared grid. In the triangular case, grid size denotes the radius of a circumscribed circle for a triangle and in the squared case, grid size is side length of a square.

The model converges to a stable solution after 15 viscosity iterations in the case of a triangular grid, whereas the squared grid converges after 18 iterations. This difference is even more pronounced when a periodic boundary condition (Fig. 2.4b) is used. In this case the triangular grid converges after 20 iterations to a stable solution as opposed to the squared grid, which needs around 60 iterations to reach a stable solution. The absolute errors decrease monotonically for all gird sizes and grid types except for the triangular case with a grid size of 50 m. Even though a stable solution is reached for this case as well with both an analytical and a periodic boundary condition, this suggests that gird sizes of 50 m or bigger are not suitable for triangular grids. The maximum error, or difference between the analytical solution for this case and the model, varies significantly depending on grid size, grid type and boundary condition used. To emphasize this behavior of the model, maximum errors for triangular and squared grids along with the boundary conditions and grid sizes used are summarized in Table 2.1. The number of viscosity iterations after which the maximum error is calculated are given in the last column, named "visc. iter.".

Obviously, the model gets more accurate with smaller grid sizes, which is expected for a finite element model. The analytical boundary condition leads to smaller errors compared to the periodic boundary condition. This suggests
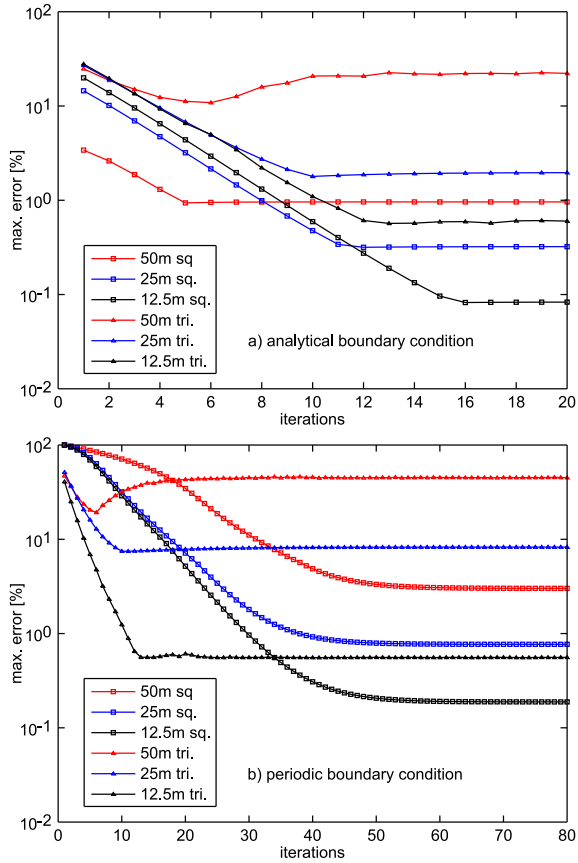
Figure 2.4: The convergence of the absolute error between the model and the analytical solution as a function of viscosity iterations using a logarithmic vertical scale. The results for triangular and squared grids with an analytical boundary condition (a-bc) are presented in (a) and with a periodic boundary condition (p-bc) in (b). The grid sizes used (40 m, 25 m and 15 m) are given in meters.

| max. error (%) | max. error (%) | BC | grid | visc. |
triangle	square		size	iter.
22.20	0.96	a-bc	50	20
45.04	3.02	p-bc	50	80
1.96	0.32	a-bc	25	20
8.27	0.77	p-bc	25	80
0.6	0.08	a-bc	12.5	20
0.56	0.19	p-bc	12.5	80

Table 2.1: Maximum difference between the analytical solution and the model for different grid types, gird sizes and boundary conditions. Here a-bc denotes the analytical boundary condition and p-bc the periodic boundary condition respectively. The number of viscosity iterations used to obtain the presented maximum errors is given in the last column, named "visc. iter."

that the analytical boundary condition forces the model somewhat towards a pre-described solution, leading to smaller maximum errors. The periodic boundary condition on the other hand, which does not pre-describe velocities at the boundary, is not forcing the model in such a manner.

Another important result of this numerical test is the different error behavior between triangular and squared girds. Obviously the squared elements are numerically more stable and always produce much lower maximum errors than triangular elements. This behavior is not surprising since it is much easier to reconstruct the gradient of the velocity field on a squared grid than on a triangular. The gradient of the velocity field is used to calculate the viscosity (cp. eq. 2.10 and eq. 2.9) and therefore errors in the gradient also introduce errors in the final numerical result. The triangular elements despite their weaker error performance have three great advantages over the squared elements. It is much easier to describe complex geometries with triangular elements, changes in grid size within the model are no problem and they converge much faster to a stable solution when a periodic boundary condition is used. The right choice of element type and grid size depending on the complexity of the model geometry is therefore vital to obtain good numerical results.

It should be noted that an upper viscosity limit as described in subsection 2.3.2 is not needed to get good numerical results with large grid sizes. Only when grid sizes become small (> 15 m) in regions of low deviatoric stresses, than an upper viscosity limit is needed to reach a stable solution. If the viscosity is not regulated in such a case, the model does not reach a steady solution and errors oscillate between 5 to 15 % despite the number of viscosity iterations. This behavior can be explained by the fact that the finite element method uses a weak formulation of the Stokes problem and therefore uses an averaged viscosity

near the upper surface. If the grid size becomes very small, even the averaged viscosity tends towards too high values or even becomes singular.

The error behavior of icetools is comparable with other Full Stokes finite element ice models. Gudmundsson (1994) reports for the same test case a maximum error of 0.04 % if the analytical solution is used as an inflow and outflow boundary and 0.1 % if a periodic boundary condition is used. Rectangular grid elements are used but no gird size is specified. Helbing (2006) obtains a maximum error of 0.1 to 0.2 % for a 300 m thick and 300 m long slab of ice, which had a tilt angle of 4°. A grid size of 10 m on squared grids was used for this experiment together with a periodic boundary condition. Both finite element models are based on the same commercial code.

2.4.2   Gaussian-shaped bed disturbance

Gudmundsson (2003a) derived transfer functions for a linear medium describing the ice surface geometry corresponding to a certain bedrock undulation. Comparing numerical model results for linear and non-linear ice rheologies with these functions was already done extensively for a sinusoidal basal topography by Raymond and Gudmundsson (2005).

Here another type of basal topography is investigated. A single, Gaussian-shaped bed disturbance is used in a model simulating the evolution of the surface geometry with time. Following the convention of Gudmundsson (2003a), all spatial variables are nondimensionalized using the mean ice thickness h, in this case 200 m. So the dimensional spacial variables x and z become nondimensional with $(x, z) = h(X, Z + 1)$ and are named X and Z. The bed disturbance has a maximum extent along the bedrock of 2h and a maximum height of 0.4h. The dimensions of the bed disturbance and the ice thickness were chosen to represent a typical subglacial ridge under a shallow glacier. The bedrock has an inclination of 3°, no basal sliding is imposed on the bedrock boundary and the whole model reaches to 10h on both sides from the center of the disturbance. Another model was set up to investigate the linear case further where the model geometry reaches to 30h on both sides from the center. As a boundary condition for the inflow and outflow boundary the analytical solution of a inclined plane is used in both cases, for both linear and non-linear rheology. The choice of the analytical boundary condition is based in the better error performance of icetools with this type of boundary condition in combination with triangular grid elements, which are used in this test. A grid size of 20 m was chosen for the surface as well as the outer regions of the model, whereas in the region around the bed disturbance the grid size is 10 m. The surface evolution with time is modeled with the kinematic boundary condition (Hutter, 1983) as

$$\frac{\partial F}{\partial t} + \boldsymbol{v} \cdot \nabla F = \dot{b}, \tag{2.12}$$

with $F(x,t)$ being a function describing the glacier surface elevation and $\dot{b}(x,z,t)$ is the accumulation/ablation rate along the surface. Using a surface mass balance $\dot{b} = 0$, this boundary condition is integrated forward in time with a forward Euler finite difference scheme after 15 iterations for the viscosity. The finite difference scheme for the surface evolution and the finite element scheme for the ice flow have the same grid size along the surface boundary. After the surface was updated using the kinematic boundary condition, the model geometry is remeshed using the Gmsh software. Time steps of 3 years are used in this simulation.

Four final surfaces are compared in Fig. 2.5a; the transfer functions (red), a linear medium with a viscosity of 8×10^{13}Pa s (dashed blue), a non-linear medium with a Glen rheology using $n = 3$ and $A = 23 \times 10^{-16}$s^{-1}kPa^{-3} (green), all three for the 20h long model domain, and the linear medium for the 60h long model (blue). The longer model geometry in the linear medium case was computed to investigate the influence of the size of the model domain on the solution and to reveal effect of the boundary conditions on the model behavior. Clearly the 20h long model (dashed blue) was not suitable for the linear case. The outflow boundary condition is influencing the surface geometry shape, which is not the case in the 60h long model (blue). Therefore the 20h long linear rheology model is considered invalid and the 60h long model domain is referred to as the linear rheology case in the subsequent discussion. For the non-linear rheology case, the 20h long model domain is sufficient to avoid influences of the outflow boundary on the surface geometry.

Clearly two dents have formed in all four different solutions to the problem (Fig. 2.5). Monitoring the maximum vertical movement per year, $v_{z(max)}$, in the regions around the dents is used to define when the evolution approaches steady state.

To estimate the actual numerical value of $v_{z(max)}$ which is used as a steady state criteria, the non-linear rheology case is investigated. The upslope dent region is defined from X=0 to X=2 and $v_{z(max)}$ in the first time step is 1.3 m year^{-1} or 6.5×10^{-3}h year^{-1}, while the downslope dent region is between X=-2 and X=0 and $v_{z(max)}$ has a value of -1.35 m year^{-1} or -6.8×10^{-3}h year^{-1} in the first time step. $v_{z(max)}$ is continuously decreasing with each time step. Steady state is here defined as when $v_{z(max)}$ has decreased two orders of magnitude from the initial value at the upslope dent. In this case $v_{z(max)} = 0.01$ m year^{-1} or 5×10^{-5}h year^{-1}. This occurs after 135 years for the non-linear rheology. The same steady state criteria is applied to the linear rheology case and is fulfilled after 282 years.

The upslope dent in both of the numerical results fits well with the transfer function, especially for the linear rheology (blue). The downslope results from the numerical simulations correlate with the transfer function as well, but an offset in both solutions is observed. This offset is similar for the linear and the
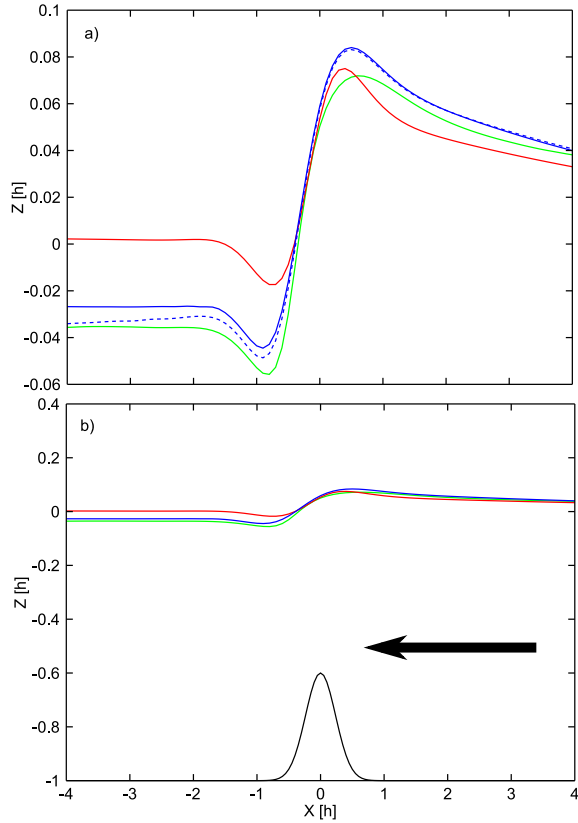
Figure 2.5: Comparison of three numerical model results with the analytical transfer functions for a linear medium (red). The numerical result for a linear medium with a viscosity of 8×10^{13}Pa s (dashed blue),and a non-linear medium with $n = 3$ and $A = 23 \times 10^{-16}$s^{-1}kPa^{-3} (green) are displayed for the 20h long model domain. The linear medium case for a 60h long model domain (blue) is also shown. All numerical solutions are plotted after they fulfilled the steady state criteria (cp. text). Main flow direction is indicated with the black arrow. (a) displays a close-up view of the surface response to the bed disturbance, whereas (b) includes the actual bed disturbance and the 20h linear medium case is not plotted here.

non-linear case, about $\sim$ -0.035h. Both numerical models produce downward movement of the surface downstream of the bed disturbance, which causes these misfits. A comparison of the ice volume upstream ($X > 0$) with the ice volume downstream ($X < 0$) of the bed disturbance can explain the misfit between the numerical results and the analytical transfer function. Overall mass and therefore volume conservation is ensured in the models by using the same inflow and outflow boundary condition. The upstream volume in the final, steady state geometry is found to be slightly larger compared to the initial geometry, whereas the downstream volume is smaller. The excessive ice volume on the upstream side matches the missing ice volume on the downstream side in both numerical results. For the linear medium $\sim$ 1% more volume is found on the upstream side compared to the initial total ice volume, whereas on the downstream side $\sim$ 1% is missing. The non-linear medium shows the same behavior with $\sim$ 2% volume imbalance between the upstream and downstream side. The reason for this is that the ice flux over the bed disturbance is smaller in the numerical models compared to the analytical solution.

As demonstrated by Raymond and Gudmundsson (2005), there is an increasing difference between the analytical and the numerical transfer amplitude with increasing bed disturbance amplitude for the linear rheology case. Their estimate of the percentage difference in amplitude for a bedrock amplitude of 0.4h, given a sinusoid bed disturbance with a wavelength of 5h, is $\sim$ -19 %. Comparing the amplitudes of the upslope dent in the linear case presented here gives a percentage difference of $\sim$ 12 % whereas at the downslope dent the amplitudes have a $\sim$ -9 % difference.

The analytical transfer function used in this comparison which serves as an analytical solution to the problem is based on perturbation theory (Gudmundsson, 2003a). For small bed disturbance amplitudes ($< 0.1h$), the discrepancy between numerical results and the transfer function is less than 2 % (Raymond and Gudmundsson, 2005). As the amplitude of the basal disturbance increases, so does the discrepancy between the numerical and analytical solution. This behavior is caused by non-linear finite amplitude effects, which are not accounted for in the analytical perturbation solution. However, Raymond and Gudmundsson (2005) found that the observed differences between the numerical and analytical solution for a sinusoidal bed are smaller than expected for a high amplitude bed disturbance of 0.4h, as used here for the Gaussian-shaped disturbance.

Calculating the correlation coefficients for both numerical results with the analytical transfer function reveals quite a good agreement. The correlation coefficient for the non-linear case with $n = 3$ is 0.977 and for the linear case 0.983.

This experiment was chosen to provide a comparison of the surface geometry caused by a single, Gaussian-shaped bed disturbance for a linear and non-linear medium. To the knowledge of the author this was not attempted before. The ex-

tensive analysis for sinusoidal bedrock undulations by Raymond and Gudmundsson (2005) was used as a guideline for this test and should serve as further reading.

2.5   Conclusion

This paper presents a numerical glacier model (icetools) capable of solving the full Stokes equation with the constitutive equation for ice using the finite element method. To allow large scale modeling, icetools can run in parallel on computational clusters.

Numerical benchmark tests revealed a maximum error of the model in comparison with the analytical solution for a gravity driven plane flow down an inclined plane as low as 0.08 % for the smallest investigated grid size of 12.5 m on a squared grid, using the analytical solution as inflow and outflow boundary conditions. The different error behavior between squared and triangular grid elements was demonstrated as well for this test case. By investigating the flow over a single, Gaussian-shaped bed disturbance, it was possible to achieve correlation coefficients of 0.977 for a non-linear medium with $n = 3$ and 0.983 for a linear medium in comparison with the analytical transfer functions for this problem (Gudmundsson, 2003a).

The presented model, icetools, is a useful tool for teaching Full Stokes numerical ice models utilizing its simple-to-understand Matlab$^{\circledR}$ interface. It was also successfully used to investigate formation of ice surface depressions at the subglacial Grímsvötn volcano in Iceland (Jarosch and Gudmundsson, 2007).

Acknowledgments

Chapter 3

Numerical studies of ice flow over subglacial geothermal heat sources at Grímsvötn, Iceland, using Full Stokes equations

Abstract

The importance of studying geothermal heat sources under glaciers lies in: (1) the potential for jökulhlaups from such sites; (2) the potential for enhanced sliding of ice masses caused by meltwater lubrication of the ice-bedrock interface; and (3) the potential to gain a deeper understanding of the interaction between the geothermal system and the overlying ice. We study the temporal evolution of an elongated depression on the eastern side of the geothermally active Grímsvötn caldera through numerical 2-D forward modeling, solving the full Stokes equation. The 100-150 m deep depression formed gradually between 1998 and 2004. The model results show that heat flux estimates based on depression volume are strongly dependent on the value of the rate factor A in Glen's flow law. If flow of ice into the depression is not taken into account, heat flux underestimates of

15-75 % occur, corresponding to rate factors of $10 - 68 \times 10^{-16}\text{s}^{-1}\text{kPa}^{-3}$. The estimated heat flux at the study site was 260-390 W m^{-2}, with the best estimate being 280 W m^{-2}, obtained from the best estimate of $A = 23 \times 10^{-16}\text{s}^{-1}\text{kPa}^{-3}$. The total power of the modeled site was 250-300 MW, about one tenth of the total heat output of Grímsvötn. This heat flux is of comparable magnitude to that of other powerful subglacial geothermal areas. Finally, as the maximum modeled strain rates $(1 \times 10^{-7}\text{s}^{-1})$ are within the range of the applicability of Glen's flow law, this suggests that the full Stokes approach should be valid for the study of many subglacial geothermal areas.

3.1   Introduction

Volcanic areas that lie beneath ice occur in several places on Earth, and include several ice-filled calderas (e.g. Major and Newhall, 1989; Clarke et al., 1989), and the ice caps in Iceland, notably Vatnajökull and Mýrdalsjökull (e.g. Björnsson, 1988; Björnsson and Gudmundsson, 1993; Gudmundsson et al., 1997, 2004; Larsen et al., 1998), whilst an active volcanic area lies beneath the West Antarctic Ice Sheet, near the Whitmore Mountains (Blankenship et al., 1993). Areas of localized and elevated heat flux are common in these regions and manifest themselves in various ways, from localized but long-lived geothermal areas to transient volcanic eruptions.

A heat source at the base of a glacier melts ice and the meltwater produced may either accumulate beneath the glacier or drain continuously away. In Iceland, both are observed, with the subglacial lake at Grímsvötn being the best documented example of meltwater accumulation (e.g. Björnsson and Gudmundsson, 1993; Gudmundsson et al., 1995). Here, the accumulation of meltwater at the heat source continues until the meltwater has forced a pathway underneath the surrounding ice to the ice margin, at which point there is rapid drainage of the accumulated meltwater away from the source area in a flood (jökulhlaup) (e.g. Björnsson, 1988, 2003). Floods of this type may pose threats to man-made infrastructure such as bridges and roads and can be a significant hazard to the local population in affected areas. In contrast, several smaller and long-lived depressions found in the Grímsvötn area and elsewhere above heat sources do not show signs of water accumulation, and are thought to drain continuously (Björnsson, 1988). A further possible consequence of elevated geothermal flux is that the resulting meltwater may lubricate the base of the ice, thereby enhancing basal sliding and possibly contributing to the initiation of ice streams (Blankenship et al., 1993).

The principal manifestation of a subglacial heat source is a depression in the overlying ice, often referred to as an ice cauldron. The properties of subglacial heat sources can be deduced by studying the size and depth of such depressions and their surface mass balance. Such studies enable the geothermal energy output

of the source to be determined by calorimetry (e.g. Gudmundsson et al., 2004). The geological settings of the subglacial heat sources can be divided roughly into three types:

(1) Heat sources with large and well-defined drainage basins where average values of geothermal power can be obtained from mass balance studies of the basins. These heat sources are usually large, often covering areas with dimensions considerably larger than the ice thickness. Grímsvötn is the best example of this type of setting (Figure 3.1a).

(2) Volcanic eruptions where extremely high heat fluxes occur over a short period of time and where calorimetric estimates can be obtained from ice volume changes without consideration of either surface mass balance or of ice flow (Figure 3.1b).

(3) Transient to long-lived depressions with diameters of the same order of magnitude as the ice thickness (Figure 3.1c). The margins of the drainage areas for individual depressions are difficult to define due to the lack of a clear topographic basin on the upstream side of a depression. These are the most common type of ice surface depression in Iceland, which develop above long-lived geothermal heat sources (Björnsson, 1988, 2003).

A comprehensive study of how small to intermediate size heat sources interact with the overlying ice would require extensive measurements of surface ice flow velocity at a carefully selected set of depressions in a region with known bedrock topography. These data would then need to be combined with full 3-D ice flow models to explore how the heat source properties affect the flow field. As a first step in such a study, we use 2-D numerical modeling to explore the properties of a part of the Grímsvötn geothermal area, consisting of a basal heat source and an overlying glacier (Figure 3.2). We apply a finite-element model that solves the full Stokes equation (e.g. Pozrikidis, 1996, p. 222) for ice using the non-linear Glen's flow law (Glen, 1955), similar to recently published models (e.g. Martin et al., 2004; Le Meur et al., 2004), except that we study the temporal evolution of depressions. By solving the full Stokes equation all components of the stress tensor are obtained and thus this method is ideal for the study of ice deformation above subglacial heat sources where there are sharp horizontal and vertical velocity variations.

3.2 Governing equations and numerical model

3.2.1 Stokes flow and Glen rheology

The flow of ice can be described by balance equations based on general continuum mechanics. These balance equations can be written as
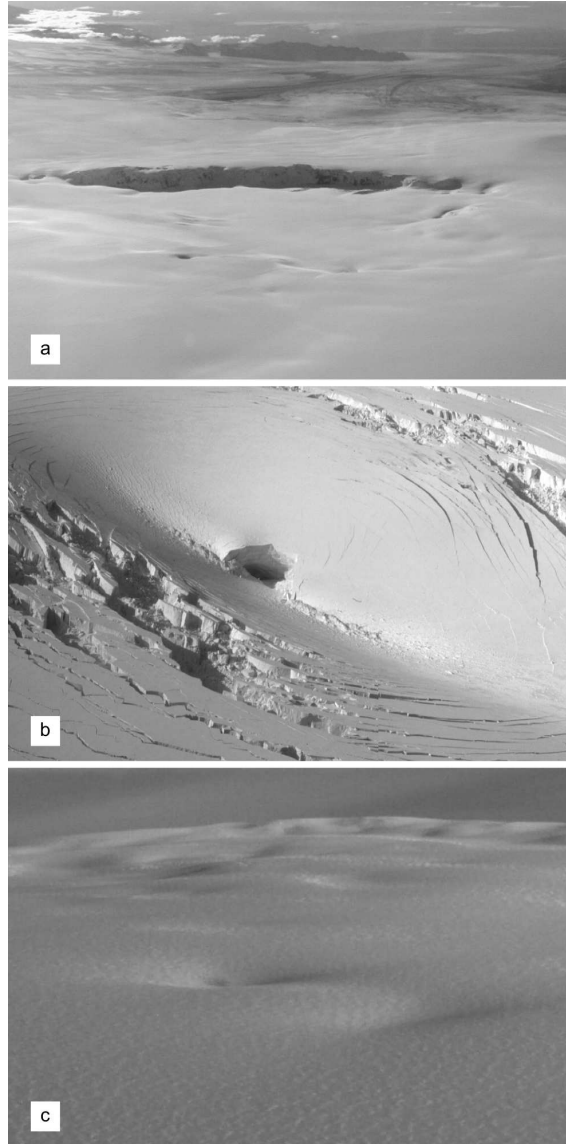
Figure 3.1: (a) The Grímsvötn caldera, (b) the rapidly subsiding depression forming during the subglacial phase of the Gjálp eruption in 1996 and (c) long-lived small depressions on Mýrdalsjökull. These represent three different types of settings for subglacial heat sources in terms of magnitude and spatial extent of heat sources (see text).
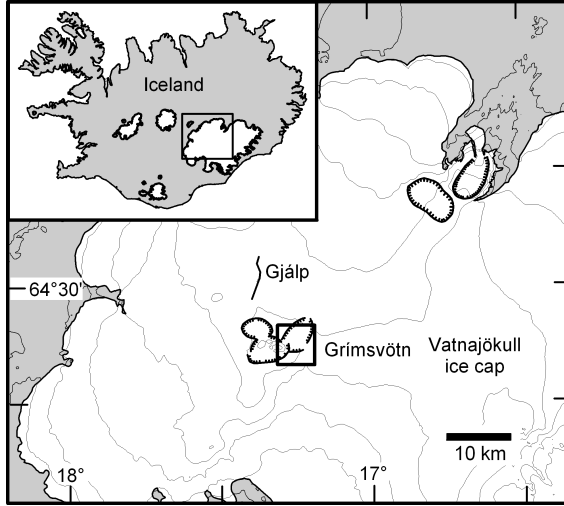
Figure 3.2: Western part of Vatnajökull and the Grímsvötn caldera. The box marks the area on Fig 3.4.

$$\nabla \cdot \boldsymbol{v} = v_{i,i} \quad = \quad 0, \tag{3.1}$$

$$\sigma_{ij,j} + \rho g_i \quad = \quad 0, \tag{3.2}$$

$$\sigma_{ij} - \sigma_{ji} \quad = \quad 0, \tag{3.3}$$

with $\boldsymbol{v}$ the velocity vector, σ_{ij} the stress tensor, ρ the density of the material, and $\boldsymbol{g}$ the gravitational acceleration vector. The density, ρ, is assumed to be constant in this model. Based on the work of Glen (1955) and Nye (1957) the viscosity of ice is stress-dependent. The constitutive equation for ice describes the relation of the strain rates ($\dot{\varepsilon}_{ij}$) to the deviatoric stress (σ'_{ij}) as

$$\dot{\varepsilon}_{ij} = A\tau^{n-1}\sigma'_{ij}, \tag{3.4}$$

with

$$\sigma'_{ij} = \sigma_{ij} - \frac{1}{3}\delta_{ij}\sigma_{ij}, \tag{3.5}$$

being the deviatoric stress tensor and δ_{ij} the Kronecker delta. τ is the second invariant of the deviatoric stress tensor, n the Glen index, and A represents a rate factor (see subsection 3.2.3).

The inverse form of equation (3.4) is

$$\sigma'_{ij} = A^{-\frac{1}{n}} \dot{\varepsilon}^{\frac{1-n}{n}} \dot{\varepsilon}_{ij}, \tag{3.6}$$

with

$$\dot{\varepsilon} = \sqrt{\frac{1}{2}\dot{\varepsilon}_{ij}\dot{\varepsilon}_{ij}}, \tag{3.7}$$

the effective strain rate. Inserting equation (3.6) into equation (3.2) leads to the Stokes equation as

$$-\nabla \cdot [\eta(\nabla \boldsymbol{v} + \nabla \boldsymbol{v}^T)] + \nabla p = \rho \boldsymbol{g}, \tag{3.8}$$

using the definition of the deviatoric stresses, p denoting the pressure, and the viscosity defined as

$$\eta = \frac{1}{2} A^{-\frac{1}{n}} \dot{\varepsilon}^{\frac{1-n}{n}}. \tag{3.9}$$

3.2.2 Boundary conditions

The principal setup of the physical problem is summarized in Figure 3.3. It is assumed that no basal sliding occurs in the modeled region. The glacier surface in the model is stress free (e.g. Raymond and Gudmundsson, 2005) and the evolution of the surface with time is simulated with a kinematic glacier surface boundary (Hutter, 1983)

$$\frac{\partial F}{\partial t} + \boldsymbol{v} \cdot \nabla F = \dot{b}, \tag{3.10}$$

with $F(x,t)$ being a function describing the glacier surface elevation and $\dot{b}(x,z,t)$ is the accumulation/ablation rate along the surface. Equation (3.10) is solved using the forward Euler scheme (e.g. Mickens, 1994) with sufficiently small time steps to avoid dispersion in the surface profile.

The boundary at the ice-bedrock interface is divided into a region without enhanced geothermal flux (Γ_{b1}) and a region with enhanced geothermal flux (Γ_{b2}), as shown in Figure 3.3. In the model this is implemented as

$$v_i = \begin{cases} \boldsymbol{0} & \text{on } \Gamma_{b1}, \\ \begin{pmatrix} 0 \\ 0 \\ \frac{q_h}{\rho L} \end{pmatrix} & \text{on } \Gamma_{b2}. \end{cases} \tag{3.11}$$

Here L is the latent heat of fusion for ice (3.35×10^5 J kg^{-1} (e.g. Paterson, 2001)) and $q_h(x)$ is the local heat flux at the base of the glacier in W m^{-2}. In
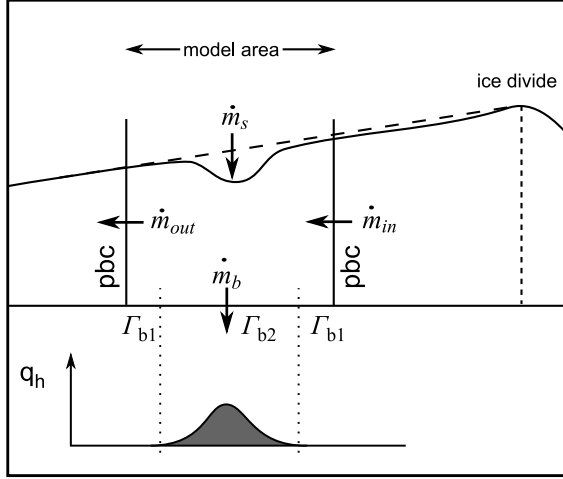
Figure 3.3: Schematic model defining mass flux terms and boundary conditions. The boundaries where periodic boundary conditions are applied are labeled with pbc.

region Γ_{b1}, equation (3.11) represents the assumption of no-slip behavior, which is a reasonable approximation for this area as shown by Aðalgeirsdóttir et al. (2000). In region Γ_{b2} , equation (3.11) describes how basal melting by the local geothermal flux leads to vertical ice velocities at the bedrock boundary. In this approach it is assumed that all heat provided by the heat source is available for melting. This is reasonable for a subglacial environment with basal ice at the melting point where the meltwater generated escapes continuously along the ice-bedrock boundary.

The inflow boundary situated upstream along the general flow direction and the outflow boundary downstream are both implemented using a 400-500 m wide segment from the boundary inside the model as a region which is periodically repeated outside the model. This periodic type boundary condition (e.g. Allen and Tildesley, 1989) allows the inflow and outflow of the system to be flow-law driven without repeating the whole model geometry. Hence it is possible to model unique features such as heat sources in the central region of the model between the boundary segments.

Equation (3.1) can also be written in mass flux terms (Figure 3.3) to illustrate the principal mass flow terms in and out of the model.

$$\frac{dm}{dt} = \dot{m}_{\text{in}} + \dot{m}_{\text{s}} - \dot{m}_{\text{out}} - \dot{m}_{\text{b}}. \tag{3.12}$$

Here $\frac{dm}{dt}$ is the rate of change of mass of ice within the system, $\dot{m}_{\mathrm{in}}$ is inflow of ice from the upslope side, $\dot{m}_{\mathrm{out}}$ is outflow on the downslope side, $\dot{m}_{\mathrm{s}}$ is surface mass balance and $\dot{m}_{\mathrm{b}}$ is basal mass balance. In equation (3.12) inflow is taken as positive and outflow is taken as negative (Figure 3.3).

3.2.3 Values of the rate factor

The model parameters n and A, which control the ice viscosity according to equation (3.9), are the two main ice model parameters which need to be examined. While $n = 3$ is the commonly used value for the stress regime in many glacial settings (e.g. Marshall, 2005; Paterson, 2001), it is well known that the rate factor A varies with temperature, impurities, anisotropy etc., and therefore that a single numerical value applicable to all settings cannot be assigned. A common approach is to use A to tune a model to fit field data (e.g. surface velocities) and in this way to ensure that all of the factors affecting ice-flow are included in the value of A. Reported values of A vary considerably. Paterson (2001, p. 85) concluded that $A = 68 \times 10^{-16}\mathrm{s}^{-1}\mathrm{kPa}^{-3}$ was the most appropriate value for temperate ice while e.g. Hubbard et al. (1998), studying valley glacier flow, used $A = 20 \times 10^{-16}\mathrm{s}^{-1}\mathrm{kPa}^{-3}$. An important result is that of Aðalgeirsdóttir et al. (2000) who derived a best fitting value of $A = 23 \times 10^{-16}\mathrm{s}^{-1}\mathrm{kPa}^{-3}$ for the closure rate of an ice depression located only 1 km to the east of the depression that is the subject of the present study (Figure 3.4). Below we test three values for A, ranging from 10 to $68 \times 10^{-16}\mathrm{s}^{-1}\mathrm{kPa}^{-3}$.

3.2.4 Finite-element model

Our finite-element model solves equation (3.8) with an initial viscosity of $\eta = 8 \times 10^{13}$ Pa s, treating the glacier as a Newtonian fluid (Paterson, 2001, p. 98). Equation (3.9) is then used to calculate the new viscosity values on each grid point in the model according to the strain rates, which are derived from the velocity field. By iterating the viscosity according to this scheme, the rheology of ice is included in the model. This approach is known as fixed point iteration. The model code is based on the open source finite-element library Getfem++ version 1.6 (available at http://www-gmm.insa-toulouse.fr/getfem/) which was modified for ice dynamics as mentioned above and extended to solve problems in parallel on computer clusters.

3.3 Grímsvötn

3.3.1 Geographical setting

Grímsvötn (Figure 3.2) has the highest eruption frequency of any volcano in Iceland. A 60 year period of unusually low activity seems to have ended with

eruptions in 1996, 1998 and 2004 (e.g. Larsen, 2002). Geothermal activity in the Grímsvötn caldera and its vicinity displays considerable temporal changes, and fluctuations in volcanism and heat output appear to be linked (Björnsson and Gudmundsson, 1993). Soon after the eruption in December 1998, a large increase in ice melting was detected under the easternmost part of the north-facing 200-300 m high caldera wall (Figures 3.4 and 3.5). The geometry of the subsidence that developed was highly elongate in an east-west direction, and consisted of interconnected ice cauldrons that partly merged with time to generate the final subsidence structure. The ice surface was surveyed annually in 1998-2004 (Gudmundsson and Högnadóttir, 2005) and this revealed that the temporal evolution of this elongated depression was irregular. For example, two large ice cauldrons formed suddenly during 1999-2000 in the center and at the eastern margin of the eventual depression (Figure 3.5), whereas the development of other segments was more gradual.

3.3.2 Model configuration

Several assumptions and simplifications are made in the modeling. Heat is assumed to be transferred instantaneously and without loss from source to ice, implying that meltwater drains immediately along the bedrock-ice interface; no storage of heat or meltwater is taken into account. This is not fully correct since in the deepest, central part of the depression, the ice was melted completely and a small meltwater lake formed above the bedrock, surrounded by ice walls. The depth of this lake varied, with its surface lying 100-150 m below the pre-depression 1998 surface. This means that not all meltwater drained away and so the meltwater that was stored acted as a thermal buffer, distributing heat to the surrounding ice walls. Some heat was also lost to the atmosphere through the water surface. This applied only to about 10% of the total depression area, so heat transfer from 90% of the heat source did occur subglacially.

Details of the evolution of individual segments of the elongated depression, and deviations from fully subglacial conditions, cannot be addressed except with a full three-dimensional model that incorporates a spatially and temporally varying heat source. Consequently our approach of using a two-dimensional model of an average profile across the depression is a crude approximation, but nevertheless it yields valuable information on the behavior of this system.

The ice surface data (Gudmundsson and Högnadóttir, 2005) were used to average three north-south oriented profiles (Figure 3.4) across the depressions to create the input for a two-dimensional model. To complete the data set, bedrock data (Björnsson et al., 1992) were also averaged on the same profiles. The change in surface elevation that occurred between 1998 and 2004 is shown in Figure 3.5.

The numerical simulation takes the 1998 averaged surface geometry as well as the averaged bedrock geometry as the initial data set. The transient evolution of the surface in 1998-2002 is simulated in time steps of 1/4th of a year which
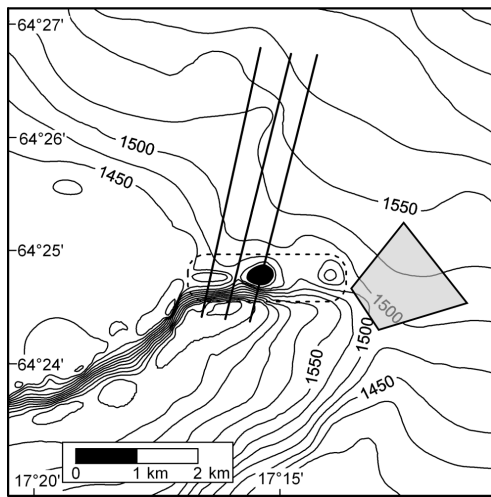
Figure 3.4: Surface map of the study area at Grímsvötn from 2004. The solid
black lines mark the three chosen profiles. They only cover the western part of
the depression since conditions were more complicated in the eastern part, where
significant ice flow occurs both from south and north. The dotted outline marks
the extent of the geothermal area and the black spot indicates the small lake
where complete melt-through occurred in the latter part of the study period.
The gray shaded area marks the location used by Aðalgeirsdóttir et al. (2000) to
estimate the rate factor A (see text).
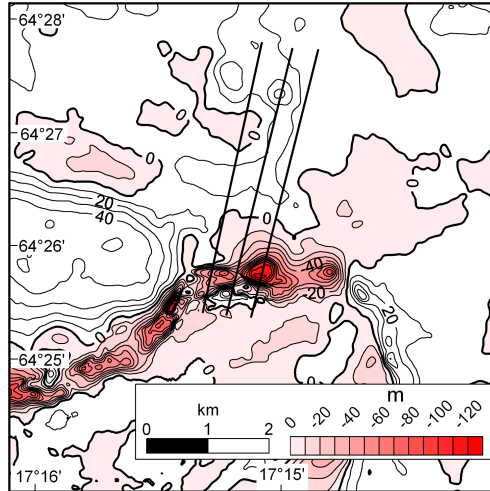
Figure 3.5: Contour map of the surface elevation change between 2004 and 1998. Black lines mark the three profiles and negative elevation change is displayed in colors. The large uplift on the left reflects a rise in the level of the subglacial Grímsvötn lake.

is sufficient for the rates of deformation generated in the model for this period. However for 2003 and 2004, 1/8th of a year time steps are used because of the increase in deformation rates within the depression.

Boundary conditions were implemented as described in subsection 3.2.2 except for the downstream outflow boundary, since the Grímsvötn model terminates at a caldera wall, where the bedrock boundary intersects the surface boundary. The geothermal flux anomaly responsible for melting is assigned a Gaussian shape, active over a 400 m long segment of the bedrock (Figure 3.6).

When inflow of ice is ignored the resulting average heat flux is $q_{start} = 226$ W m^{-2}. This number is obtained from the volume difference between the measured 1998 and 2004 surfaces using a typical value for the surface mass balance in this area of $\dot{b} = 1.35$ m year^{-1} (Aðalgeirsdóttir et al., 2003). q_{start} is an underestimate and the task of the forward modeling is to estimate the additional heat flux required to account for the additional melting of the ice that flows into the depression. The heat flux at the base is varied until the modeled evolution over a certain period of time matches the measured evolution, with q_{start} used as a staring value. The water body that accumulated in the central part of the depression during the latter part of the study period changed the heat transfer properties of the heat source-ice interface. Therefore the measured surface geometry is difficult to match with the model. Moreover, the resolution of our data
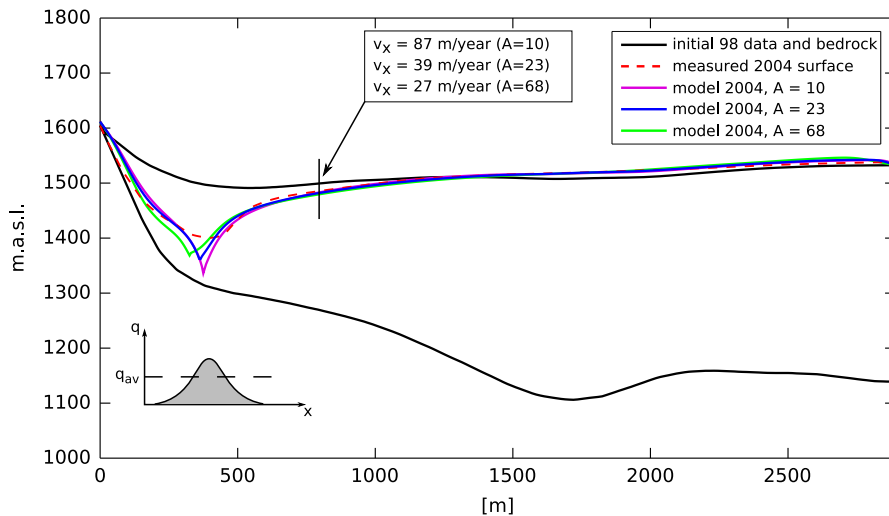
Figure 3.6: The initial 1998 surface geometry and bedrock data (black), the measured surface geometry in 2004 (red), the modeled 2004 surface with rate factors $A = 10$ (magenta), $A = 23$ (blue) and $A = 68 \times 10^{-16}\mathrm{s}^{-1}\mathrm{kPa}^{-3}$ (green). The horizontal velocities at the surface (x=800 m) for each modeled rate factor are listed for comparison.

only allows the average heat flux for the 6 year period to be estimated. The ratio between the simulated and measured volume changes on the surface during the 6-year period was used as a quality parameter and termed r_{vol}. If r_{vol} is close to 1 the volumes match and the heat flux value is estimated for the given model parameters.

3.4 Results

3.4.1 Heat flux and model parameter sensitivity

To examine the influence of different values for A on basal heat flux estimates, a set of different heat flux values was modeled with $A = 10$, 23 and 68×10^{-16} s^{-1} kPa^{-3}. The first value represents rather stiff ice (corresponding to a temperature of $\sim$ -8 °C), the second is the value estimated by Aðalgeirsdóttir et al. (2000) and the third is the recommended estimate of Paterson (2001) for pure, temperate ice. The results of these test runs are displayed in Figure 3.7.

The first striking result is the linear correlation between the estimated heat
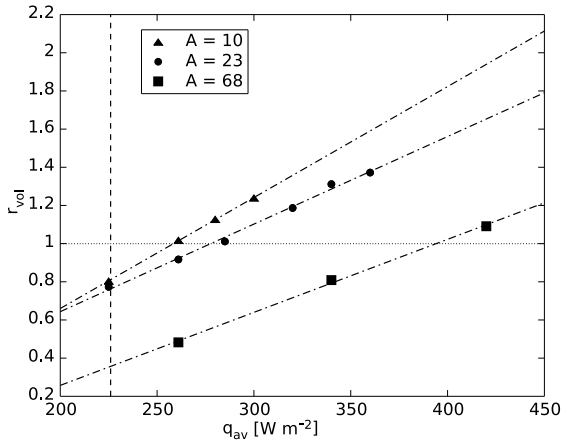
Figure 3.7: The ratio between the simulated and measured volume change (r_{vol}) during the model period from 1998 to 2004 as a function of heat flux (q_{av}) for 3 different rate factors, A ($\times 10^{-16}\mathrm{s}^{-1}\mathrm{kPa}^{-3}$). The dotted line marks the perfect volume fit, $r_{\mathrm{vol}} = 1$ and the vertical dashed line marks the heat flux value q_{start}, estimated by the measured volume change, including a surface mass balance but ignoring all ice flux. Dash-dotted lines denote the linear regressions through the corresponding data sets.

flux q_{av} and the ratio r_{vol}. This correlation can be understood by considering the direct relationship between A and deformation velocity (e.g. Paterson, 2001), hence a strong correlation between ice flow velocities (and ice flux) and the rate factor is to be expected (Figure 3.6). The estimated heat flux values q_{av} for the different rate factors are given in Table 3.1. The underestimate in heat flux is defined as $U = \frac{q_{av}-q_{start}}{q_{start}} * 100$.

The q_{av} values in Table 3.1 are obtained from the regression lines in Figure 3.7 where $r_{\mathrm{vol}} = 1$. q_{start} is here used as a reference value, since it can always be estimated from volume changes without any consideration of ice flow. q_{model} is the heat flux estimate from the actual model run that had r_{vol} close to 1.

The modeled heat fluxes vary over a range of 130 W m^{-2} which is 33 % of the value of heat flux obtained using $A = 68 \times 10^{-16}\mathrm{s}^{-1}\mathrm{kPa}^{-3}$. This illustrates the importance of quantifying the rate factor A with field methods for each study area.

A comparison of how well the modeled final surface geometries fit with the measured geometry in 2004 would indicate which rate factor best fits the data. The heat flux values from the chosen models q_{model}, their volume change ratios r_{vol} as well as R, their correlation coefficients with the measured 2004 geometry

Table 3.1: Estimated heat flux values q_{av} for different rate factors A and the underestimation U when ignoring ice flow. The actual modeled heat flux values q_{model}, with the volume fit ratio r_{vol} close to 1. R is the correlation coefficient between the modeled and the measured, final surface geometry.

A ($\times 10^{-16}\text{s}^{-1}\text{kPa}^{-3}$)	q_{av} (W m^{-2})	U (%)	q_{model} (W m^{-2})	r_{vol}	R
10	260	14	261	1.02	0.9684
23	280	23	285	1.01	0.9761
68	390	74	420	1.09	0.9685

in the horizontal segment x = 0 to 1000 m, are shown in Table 3.1. $A = 23 \times 10^{-16}\text{s}^{-1}\text{kPa}^{-3}$ is the rate factor with the highest correlation although the other two also have a high R. It needs to be pointed out that this correlation only indicates a favorable A, so it is by no means a method to estimate the rate factor A. The high correlation of $A = 23 \times 10^{-16}\text{s}^{-1}\text{kPa}^{-3}$ is not surprising since this value of A was determined from an earlier study of a depression only 1 km away from the one studied here (Aðalgeirsdóttir et al., 2000). Therefore we will use $A = 23 \times 10^{-16}\text{s}^{-1}\text{kPa}^{-3}$.

Another model parameter influencing the heat flux estimate is the surface mass balance $\dot{b}$. The surface mass balance adds to the ice volume in the model and therefore the higher the surface mass balance the more heat is needed to create the same volume change over a given period of time. For the geometry and time period studied in the Grímsvötn case a maximum estimate of the error in surface mass balance is ± 0.5 m year^{-1}. This would lead to an error of ± 15 W m^{-2} in heat flux estimation, which amounts to 4-6 % error in the heat flux values obtained in Table 3.1. The maximum error in mass balance is used because of the location of the study site near the caldera rim, where variable amounts of snow drift will affect the surface mass balance.

3.4.2 Velocity, strain rates and surface evolution

The velocity vector components for the Grímsvötn model after 6 years of evolution using a rate factor of $A = 23 \times 10^{-16}\text{s}^{-1}\text{kPa}^{-3}$ are shown in Figure 3.8. The horizontal velocity component (Figure 3.8b) increases sixfold from the region where the flow is not influenced by the heat source (horizontal coordinate x > 2000 m) to the central part of the depression. The influence of the heat source is clearly recognizable in both the horizontal (Figure 3.8b) and the vertical (Figure 3.8c) velocity components. The zone of influence reaches from x < 1600 m to the center of the depression on the northern, upstream side of the model and
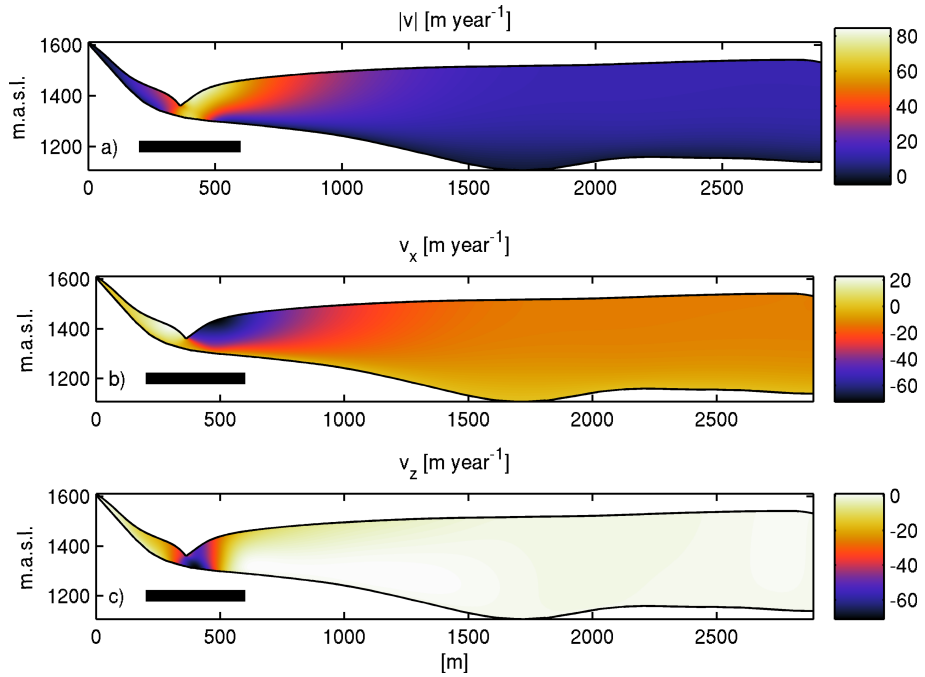
Figure 3.8: The final velocity flow field at the end of the simulation ($A = 23 \times 10^{-16}\text{s}^{-1}\text{kPa}^{-3}$). (a) the norm of the velocity vector, (b) the horizontal and (c) the vertical component as colors in m year^{-1}. The black bar indicates the extent of the heat source.

up the slope on the southern side to x $\sim$ 200 m. On the northern side this region extends several ice thicknesses outwards from the center of the depression. The asymmetry in the flow field caused by the southern slope is a distinct feature in both velocity components. The difference in inflow rates between the northern and southern sides of the depression is approximately 30 m year^{-1} in the innermost part of the depression (see Figure 3.8a). This effect leads to a shift of the center of the depression to the south. The time evolution of the shifting of the center is shown in Figure 3.10 together with the final heat flux distribution. The center of the heat source is at x = 400 m and the center of the depression is at x = 360 m, which leads to 40 m offset over 6 years of evolution. But this offset is not linear with time. During the first two years the offset is rather inconspicuous, whereas during the following four years the offset becomes increasingly more apparent.

The maximum error in the modeled velocity is estimated as 4 %, which is
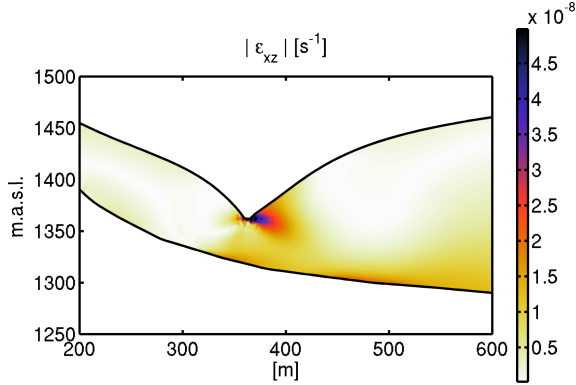
Figure 3.9: The $|\dot{\varepsilon}_{xz}|$ component of the strain rate tensor for the Grímsvötn model after 6 years of evolution. The maximum value is $\sim 1 \times 10^{-7}\mathrm{s}^{-1}$ in the very center of the depression.

the maximum difference between the model-derived velocities for a parallel-sided slab of ice and the analytical solution for the slab. Using this 4 % error in the velocities, and by comparing velocity values at points separated by a distance of $1/4$ of the ice thickness, a maximum error of 10 % in the strain rates is obtained. However this finite-element model treats the ice as a non-Newtonian fluid (with the rheology given by Glen's flow law), therefore the model does not account for crack formation within the continuum. At a strain rate of less than about $10^{-7}\mathrm{s}^{-1}$, ice at a temperature above -20 °C deforms with fully ductile creep, whereas for strain rates higher than $10^{-6}\mathrm{s}^{-1}$, ice fractures with little if any prior plastic deformation (Petrenko and Whitworth, 1999, p. 206). Thus, at such high strain rates the rheology of Glen definitively stops describing the continuum. The $|\dot{\varepsilon}_{xz}|$ component of the strain rate tensor for the final geometry is shown in Figure 3.9. $|\dot{\varepsilon}_{xz}|$ is less than $2 \times 10^{-8}\mathrm{s}^{-1}$ for most parts of the depression. Only in the innermost, steepest part does $|\dot{\varepsilon}_{xz}|$ increase to $\sim 5 \times 10^{-8}\mathrm{s}^{-1}$ (blue-black area in Figure 3.9). The peak value of $\dot{\varepsilon}_{xy} = 1.0 \pm 0.1 \times 10^{-7}\mathrm{s}^{-1}$ is found at the surface within this region. The highest near-surface strain rate, relevant for crevasse formation, is $\dot{\varepsilon}_{xx} = 5.0 \pm 0.5 \times 10^{-9}\mathrm{s}^{-1}$, which is well within the defined range for full ductile creep for ice. This implies that crevasses observed in the field at the study site did not reach deep into the ice and therefore do not appreciably influence the ductile behavior of the ice.

Figure 3.10 shows the evolution of the surface geometry in one year time steps throughout the model period from 1998 to 2004. The dashed line marks the measured surface geometry of 2004. It is clear that the model fit is rather poor in the innermost region of the depression. The reason for this discrepancy is that water
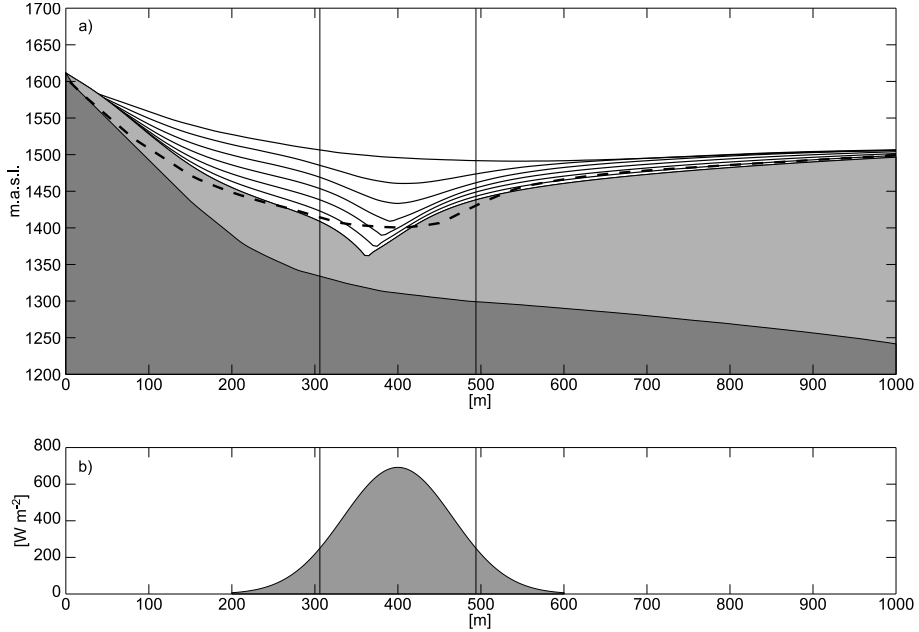
Figure 3.10: (a) The modeled surface for each year in comparison with the average of the three surface profiles in 2004 (dashed line). (b) The heat flux distribution. The vertical solid lines mark the region with $q_{av} \geq \frac{q_{max}}{e}$, indicating the hot region of the heat source.

accumulated during the latter part of the study period (c.p. subsection 3.3.2) and therefore the model does not reflect the associated change in heat transfer properties. There is also a mismatch between the data and the model on the southern slope, near the southern boundary. This is caused by the surface mass balance, which in the model has snow accumulating on the slope rather than drifting and being deposited in the depression. So this mass addition of snow might contribute to the mismatch in the center of the depression between the modeled and the measured surface.

3.5 Discussion

The present work illustrates the importance of considering inflow of ice to depressions (ice cauldrons) in glaciers when studying the thermal output of underlying geothermal areas. The model results indicate that if only depression volume is considered and inflow of ice ignored, the basal heat flux may be underestimated

51

by 15-75 %. This large range in values is caused by uncertainty in the value of A, the rate factor. However, the strong dependence of the deformation velocity on the rate factor indicates that information on surface flow velocities can be used to estimate the value of A for each study site, thus reducing the uncertainty in heat flux and thermal power.

The favored rate factor of $A = 23 \times 10^{-16} \text{s}^{-1} \text{kPa}^{-3}$ is low, only one third of the value suggested by Paterson (2001) for temperate ice (Aðalgeirsdóttir et al., 2000). It is well known that several tephra layers and scattered ash particles occur within the ice in the Grímsvötn area (e.g. Larsen et al., 1998) and that such impurities at low concentrations may soften ice and could give higher rate factors, whereas such impurities at high concentrations (of order 15 %) have little impact on the rate factor (e.g. Marshall, 2005). Ice softening due to low concentration of impurities must therefore be overwhelmed by another property or process that would tend to stiffen the ice. It is possible that the result of relatively stiff ice around Grímsvötn is caused by the transient nature of the studied flow fields. Both in the present study and in the study of Aðalgeirs-dóttir et al. (2000) ice flow was diverted from the prevailing flow direction. The depression analyzed by Aðalgeirsdóttir et al. (2000) formed by collapse during the draining of meltwater from Grímsvötn in November 1996, in the aftermath of the Gjálp eruption. The formation of the depression studied in this paper led to diversion of ice flow from west-southwest to south. As a consequence, any anisotropy present in the ice will have been unfavorably oriented relative the new flow direction leading to a low rate factor.

One of the limitations of the present method is that the width of the zone of elevated heat flux cannot be defined with any certainty. In our model this width is about the same as that of the ice thickness. It is to be expected that a much wider zone of elevated heat flux would lead to a wider depression. However, it is likely that the results on depression shape would not be significantly affected by a narrower heat source provided that the total power remained the same. This relative insensitivity of depression shape for heat source widths smaller than one ice thickness has been verified with runs of synthetic models (not presented here).

The total thermal power is a key parameter in studies of geothermal heat and its potential for ice melting, and the possible generation of subglacial lakes with meltwater release through jökulhlaups. For a 2-D source, defined from heat flux q_{av} and heat source width, l, the power per unit length of source (perpendicular to model section) is $P' = lq_{av}$. For the Grímsvötn study area, the value of this parameter lies in the range 104-168 kW m^{-1}, with the best estimate (for $A = 23 \times 10^{-16} \text{s}^{-1} \text{kPa}^{-3}$) of 114 kW m^{-1}. Since the length of the modeled part (western part) of the depression (Figure 3.5) is about 1.4 km, the total heat output is estimated to be 160 MW. The total length of the area is 2.5 km. Subsidence in the eastern part is on average similar to that of the modeled area, suggesting that the time averaged total heat output for the whole area

may have been 250-300 MW. This is about one tenth of the total thermal power of Grímsvötn (Björnsson and Gudmundsson, 1993). The 250-300 MW can be taken as a minimum value since direct heat loss to the atmosphere from the 200 m wide water body in the central part of the depression during the latter part of the period is ignored. However, as pointed out earlier, this direct heat loss is considered to have been very minor compared to the heat required for ice melting.

The estimated heat flux of 260-390 W m^{-2}, with 280 W m^{-2} the value obtained with the best estimate of $A = 23 \times 10^{-16}$s^{-1}kPa^{-3}, can be compared to other heat flux estimates. The power of heat sources encountered in volcanic regions varies considerably. Björnsson and Gudmundsson (1993) estimated the total heat output of Grímsvötn for 1922-1991 and noted that it had reached a maximum of 11600 MW in 1934-1938 and dropped to around 2000 MW in the 1980s. The highest value was associated with active volcanism whereas the lowest value was associated with a period when volcanic activity was absent. A minimum heat flux value at Grímsvötn is obtained by assuming that the total heat output is evenly distributed over an area of 40-70 km^2 and this yields a basal heat flux of 30-50 W m^{-2}. However, the total heat output is not evenly distributed since it is partly manifested in separate depressions that have a combined area 10-20 km^2. The assumption that all heat is released beneath these cauldrons yields an average heat flux of several hundred W m^{-2}. Another example is the eastern Skaftár cauldron 10 km northwest of Grímsvötn, which has a total heat output of 800 MW (Björnsson, 1988). Taking the area of elevated heat flux as 6-7 km^2 (the area of the surface depression in 1998) an average heat flux of 120 W m^{-2} is obtained. This comparison suggests that the heat flux of the surveyed site is of the same order of magnitude as for other cases.

It remains to be tested whether the model approach used here can be applied to the much higher heat fluxes and deformation rates that accompany volcanic eruptions under ice. In the 1996 Gjálp eruption the heat flux is estimated to have been three orders of magnitude higher than that obtained here: in the Gjálp eruption it was 5-6 $\times$ 10^5 W m^{-2} during the first three days, and the horizontal strain rate for the first 16 hours was $\approx 1.3 \times 10^{-6}$s^{-1} (Gudmundsson et al., 2004). This is a subject for further research.

We have demonstrated the method of using a finite-element model to simulate the surface evolution of a glacier above a heat source is a useful tool for estimating heat source properties and characterizing glacier response. More detailed studies of the properties of a subglacial heat source are possible using three dimensional full Stokes models. This would allow modeling of the inflow of ice into a depression created by a heat source to be studied in greater detail, and also would include possible cross flow through such depressions.

3.6　Conclusion

A two-dimensional finite-element model that solves the full Stokes equation has been used to study the properties of a subglacial heat source forming an elongated depression in the ice surface in the eastern part of the Grímsvötn caldera, Iceland. The evolution of this depression over the period 1998-2004 has been simulated. The results demonstrate the necessity of considering ice flow towards subglacial geothermal areas if reliable estimates of their thermal power are to be obtained. The main findings can be summarized as follows:

- A systematic 15-75 % underestimate of the geothermal flux can occur if inflow of ice into the depression is ignored. In this study, the amount by which the geothermal flux is underestimated is shown to be linearly related to the chosen values of the rate factor A in Glen's flow law. It is found that omission of the heat contribution used to melt inflowing ice would lead to an underestimate of 23 % if $A = 23 \times 10^{-16} \mathrm{s}^{-1} \mathrm{kPa}^{-3}$ is used.

- The average heat flux under the depression is estimated as 260-390 W m^{-2}, with 280 W m^{-2} corresponding to the favored value of A. These heat flux values are of the same order of magnitude as those at other, powerful subglacial geothermal areas in Iceland. The mean heat output of the 2.5-km-long depression over the survey period was 250-300 MW.

- The maximum deformation rate determined by the model is $1 \times 10^{-7} \mathrm{s}^{-1}$, indicating that Glen's flow law (and thus the full Stokes approach used here) should be widely applicable to many cases where geothermal areas occur beneath ice.

3.7　Acknowledgments

Chapter 4

Progressive cooling of the hyaloclastite ridge at Gjálp, Iceland, 1996 - 2005

Jarosch, A. H., Gudmundsson, M. T., Högnadóttir, Þ, Axelsson, G.: *Progressive cooling of the hyaloclastite ridge at Gjálp, Iceland, 1996 - 2005*, Journal of Volcanology and Geothermal Research, 2007. (submitted)

Abstract

In the subglacial eruption at Gjálp in October 1996 a 6 km long and 500 m high subglacial hyaloclastite ridge was formed while large volumes of ice were melted by extremely fast heat transfer from magma to ice. Repeated surveying of ice surface geometry, measurement of inflow of ice, and a Full Stokes 2-D ice flow model have been combined to derive a heat output at Gjálp for the period 1996-2005. The very high heat output of order 10^6 MW during the eruption was followed by rapid decline, dropping to ∼2500 MW by mid 1997. It remained similar until mid 1999 but declined to 700 MW in 1999-2001. Since 2001 heat output has been insignificant, probably of order 10 MW. The total heat carried with the 1.2×10^{12} kg of basaltic andesite erupted (0.45 km^3 DRE) is estimated to have been 1.5×10^{18} J. About 64% of the thermal energy released from the 0.7 km^3 edifice in Gjálp occurred during the 13-day long eruption, 20% were released from end of eruption until mid 1997, a further 10% in 1997-2001, and from mid 2001 to present, less than 2%. The heat output history can be reconciled with the gradual release of the 5×10^{17} J thermal energy remaining in the Gjálp ridge after the eruption, assuming single phase liquid convection in the cooling edifice. The

average temperature of the edifice is found to have been approximately 240 °C at the end of the eruption, dropping to $\sim$ 130 °C after 7 months and reaching $\sim$ 38 °C in 2001. Although an initial period of several months of very high liquid permeability is possible, the most probable value of the permeability from 1997 onwards is of order 10^{-12} m^2. This is consistent with consolidated/palagonitized hyaloclastite but incompatible with unconsolidated tephra. This may indicate that palagonitization had advanced sufficiently in the first 1-2 years to form a consolidated hyaloclastite ridge, resistant to erosion. No ice flow traversing the Gjálp ridge has been observed suggesting that it has effectively been shielded from glacial erosion in its first 10 years of existence.

4.1 Introduction

Volcanic eruptions within glaciers or ice sheets create a variety of structures and morphologies, including hyaloclastite mountains and sheets (Kjartansson, 1943; Mathews, 1947; van Bemmelen and Rutten, 1955; Jones, 1969; Lescinsky and Fink, 2000; Gudmundsson, 2005). Within large glaciers and ice sheets, high heat transfer rates from fragmented magma to ice cause melting of large volumes of ice and large outburst floods (jökulhlaups) which drain the meltwater produced (Björnsson, 1988; Major and Newhall, 1989). Subglacial volcanic activity during the Pleistocene was a major land-shaping process in Iceland, which created tuyas (table mountains) and hyaloclastite ridges, that dominate large parts of the modern landscape. The present-day volcanic zones of Iceland are still partly covered with glaciers and ice caps, and subglacial volcanic activity is frequent (e.g. Larsen et al., 1998). Subglacial volcanism can be identified as an important process of land formation in other parts of the world, e.g. in western Canada (Mathews, 1947; Hickson, 2000) as well as on the Antarctic Peninsula, where large hyaloclastite regions are found (Smellie, 1999). Active volcanoes may also exist under the West Antarctic Ice Sheet (Blankenship et al., 1993).

The Gjálp eruption occurred in the autumn of 1996 within Vatnajökull (Fig. 4.1), the largest glacier in Iceland. The eruption began on September 30th, at about 22h GMT, with the onset of continuous seismic tremor and lasted until October 13th (Einarsson et al., 1997). During the eruption 3 km^3 of ice melted and the Gjálp hyaloclastite ridge was formed with a volume of 0.7 km^3, rising about 500 m over the pre-eruption bedrock and extending about 6 km along the bed (Gudmundsson et al., 1997, 2002a, 2004). It took 30 hours for the eruption to melt its way through the 550 m thick ice at the eruption site. Gudmundsson et al. (2004) give a detailed description of the course of events during the Gjálp eruption. The main form of activity during the eruption was quenching and fragmentation of magma into volcanic glass and the observed heat transfer rate during the first ten days of the eruption reached a maximum of $\sim 2.6 \times 10^{12}$ W (Gudmundsson et al., 1997). Only about 2-3 % of the energy released during the eruption is
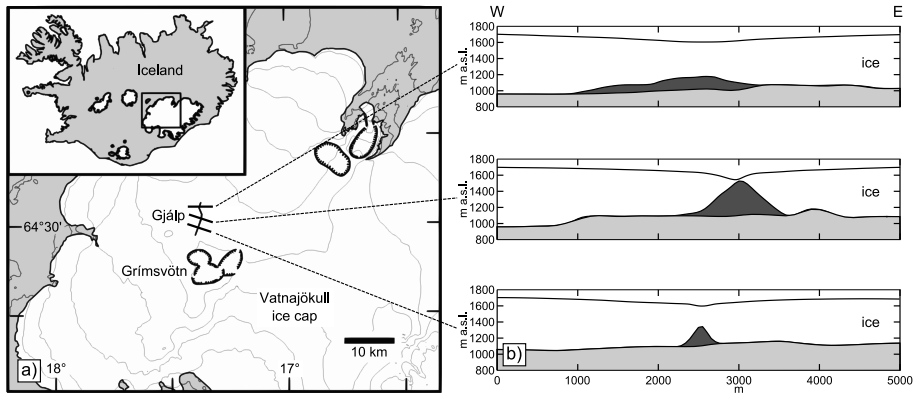
Figure 4.1: (a) Location map of the Gjálp eruption. (b) Three profiles across the Gjálp edifice. The pre-eruption bedrock is displayed in light gray and the erupted material from 1996 in dark gray along with the 1997 surface.

considered to have been lost to the atmosphere (Gudmundsson et al., 2004).

Comparing the Gjálp edifice and it's evolution with ridges formed during the Pleistocene under an ice sheet gives rise to questions such as (Gudmundsson et al., 2002a): (1) How well can the freshly formed Gjálp ridge, an initially unconsolidated pile of volcanic glass and tephra, withstand erosion from moving ice? (2) Can palagonitization (e.g. Stroncik and Schmincke, 2002) prevent fast erosion and what is the rate of alteration for the Gjálp ridge? (3) What role does diversion of ice flow play in the preservation of the edifice? (4) Which general conclusions about the behavior of subglacial as well as subaqueous eruptions can be made?

A pile of unconsolidated volcanic material at the base of a glacier, subjected to fast ice flow is expected to suffer heavy erosion. Large parts of a volcanic edifice may be removed over a relatively short period; it has been suggested that such edifice removal has occurred in West Antarctica (Behrendt et al., 1995) and it may have happened also in Iceland (Bourgeois et al., 1998). The Pleistocene ridges and tuyas found in Iceland are made of pillow lava, breccia and hyaloclastite, with hyaloclastite being the major component in some of the ridges (Schopka et al., 2006; Jakobsson, 1979). A common feature of these Pleistocene formations is that the volcanic glass has altered into palagonite, turning the loose pile of volcanic glass into consolidated rock (Jones, 1969; Jakobsson, 1979). This consolidation has been a key factor in preserving the edifices by making them resistant to glacier erosion. However, the rate at which this alteration occurs in the subglacial environment is unknown, but a comparable case would be the evolution of the island of Surtsey that emerged in a phreatomagmatic eruption off the south

coast of Iceland in 1963-64. Studies at Surtsey showed that palagonitization was strongly temperature dependent; the basaltic tephra was palagonitized to dense tuff in only 1-2 years where it was subjected to mild geothermal activity at temperatures of 80-100 °C (Jakobsson, 1972, 1978; Jakobsson and Moore, 1986).

The top of the Gjálp edifice was only exposed for about a year after the eruption since it was covered by inflowing ice by the end of 1997 (Gudmundsson et al., 2002a). A deep ice cauldron remained above the submerged top (Figs. 4.2 and 4.3) gradually declining in depth. This cauldron was still present in 2005 and 2006, confirming some heat output has occurred at this place throughout the study period. No significant meltwater accumulation was detected at the Gjálp eruption site during the monitored period indicating that the produced meltwater drained continuously into the Grímsvötn subglacial lake.

It has been considered likely that palagonitization has to some extent taken place at Gjálp (Gudmundsson et al., 2002a) but in the absence of samples from the subglacial edifice this remains hypothetical. However, information on glacier development since the eruption and other indirect evidence on the thermal state of the edifice would provide important constraint on ideas on development of hyaloclastite mountains within glaciers. In this paper we apply calorimetry, ice flow modeling and field measurements of ice depression volume and ice flow velocities to derive estimates of heat output from the Gjálp ridge over the 10 year period since its formation. This record is used to derive a rough temperature history of the edifice. The record provides important constrains on the post-eruption thermal evolution of subglacially formed volcanic edifices and the time scales of glacier healing after a subglacial eruption.

4.2 Method of heat output estimation

Our approach is to use calorimetry to derive the heat output from Gjálp. The record can be divided into two parts:

a) During the eruption. Here the heat output record is obtained from the mass of ice melted during the eruption, estimated from volume of ice depressions at the eruption site and along the flow path of the meltwater. This record already exists (Gudmundsson et al., 2002a, 2004).

b) The thermal power after the eruption. Here surface mass balance and inflow of ice into the depressions need to be taken into account to derive meaningful estimates of basal melting.

After the Gjálp eruption, a separate ice drainage basin formed around the depressions created by basal melting during and immediately after the eruption (Gudmundsson et al., 2002a, 2004, 2002b; Björnsson et al., 2001; Alsdorf and Smith, 1999). We apply mass continuity and define the Gjálp depression
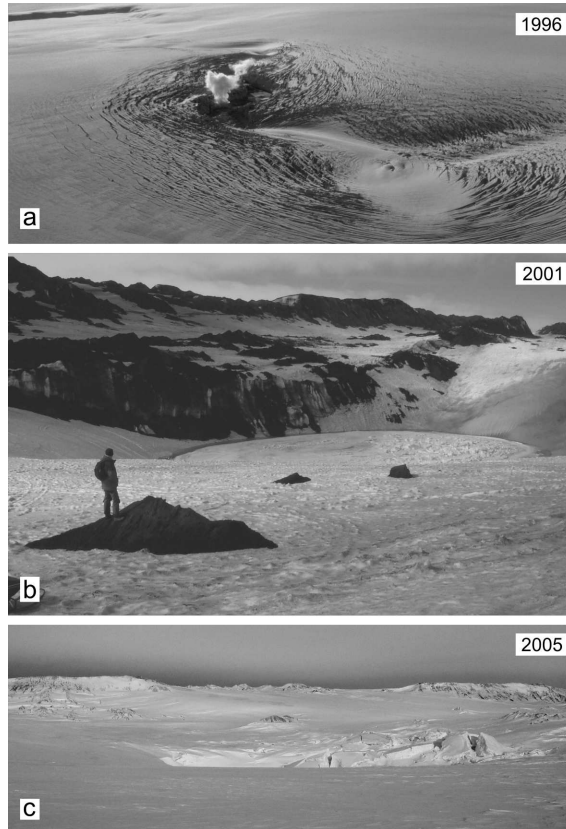
Figure 4.2: Evolution of the Gjálp surface depression. (a) The new surface depression in October 1996 from the air, two weeks after the end of the eruption. The depression was about 4 km wide at that time with steam rising from the subglacial crater. (b) The cauldron at the site of the subareal crater in June 2001. In the background, tephra covered ice ridges are visible. (c) The same site as in (b) in October 2005 with the ice ridges in the background.

(Figs. 4.1, 4.2 and 4.3) as our system. The rate of mass loss by melting and subglacial water drainage at the base is the parameter sought, since it is directly proportional to geothermal power. In accordance with observations of ice surface depression shape and extent, we assume that all basal melting occurs at the boundary between the Gjálp ridge and the overlying glacier. The system is bounded on the eastern, southern and western sides by ice divides (Fig. 4.3) while ice flows in through the northern boundary. The general mass balance of the system is given by

$$\rho \dot{V} = \dot{m}_{\text{in}} - \dot{m}_{\text{out}} + \dot{m}_{\text{s}} - \dot{m}_{\text{b}} \qquad (4.1)$$

with $\dot{V}$ the rate of change in the surface depression volume, ρ the ice density, $\dot{m}_{\text{in}}$ and $\dot{m}_{\text{out}}$ the mass flux into and out of the system, $\dot{m}_{\text{s}}$ the mass flux at the surface, termed surface mass balance in glaciology, and $\dot{m}_{\text{b}}$ the mass flux at the base, i.e. mass loss caused by basal melting. During the study period, $\dot{m}_{\text{out}} = 0$ was assumed, which is supported by the measured surface velocities (Fig. 4.3).

Geothermal heat flux at the base of the glacier conducts heat into the ice at the bedrock-ice interface. In case of a cold glacier or ice sheet this increases the temperature of the ice until the melting point is reached and from this point on the energy is used to melt ice. In a temperate glacier, where the ice is at the pressure melting point throughout, the energy is instantly used for melting. The Vatnajökull ice cap is temperate and thus the relation between heat output Q_{heat} [W] and ice mass melted at the base $\dot{m}_{\text{b}}$ [kg s^{-1}] is

$$Q_{\text{heat}} = \dot{m}_{\text{b}} \, L, \qquad (4.2)$$

with L being the latent heat of fusion for ice (3.335×10^5 J kg^{-1} (Petrenko and Whitworth, 1999)).

The fact that $\dot{m}_{\text{out}} = 0$ simplifies eq. (4.1) and therefore only the terms $\dot{m}_{\text{s}}$, $\dot{V}$, and $\dot{m}_{\text{in}}$ have to be estimated to quantify Q_{heat}. The mass flux terms required have been measured in the field.

4.3   Field methods

Extensive field work has been carried out since the eruption in 1996. Aerial observations including radar altimetry were applied in the months after the eruption (Gudmundsson et al., 2004) and from spring 1997 onward the eruption site was visited at least twice a year, in early spring and autumn. Seasonal and annual changes in glacier geometry, surface mass balance values and surface velocities were acquired during these visits.

4.3.1 Surface mass balance: $\dot{m}_s$

Surface mass balance data for the whole Vatnajökull ice cap has been collected continuously for the whole study period (Björnsson et al., 2002, F. Pálsson and H. Björnsson, pers. comm.) and an independent estimate was made in 2001 within the Gjálp depression by snow coring down to the tephra layers deposited in eruptions in 1996 (Gjálp) and 1998 (Grímsvötn). The result for the Gjálp area is a mean annual mass balance of 1.35 m year^{-1} ice equivalent, which leads to a $\dot{m}_s = 1240$ kg m^{-2} year^{-1}, using an ice density of 917 kg m^3.

4.3.2 Topography maps: $\dot{V}$

In June each year topographic profiles have been surveyed with a GPS mounted on a snowmobile. In the field seasons from 1996 to 2003, a DGPS with sub-meter accuracy was used but since 2004 the profiling has been done with a Trimble® R7 kinematic GPS with centimeter accuracy. On the basis of the surveyed profiles, topographic maps were drawn by hand, digitized and digital elevation models (DEMs) created using the Kriging algorithm (Cressie, 1991) (Fig. 4.3a-c).

The 1996 pre-eruption surface topography map in combination with the annual maps allows an estimation of changes in volume ($\dot{V}$) of the surface depression initially formed during the 1996 eruption (Fig. 4.3d-f).

4.3.3 Surface velocities: $\dot{m}_{in}$

Since 1997, surface ice flow velocities have been measured each summer using a network of stakes installed and positioned with GPS in spring and remeasured and retrieved in autumn. This approach allows an estimation of average summer surface velocity (v_h) at the location of the stakes (Appendix A). In June 1997 about 20 stakes were installed but due to heavy crevassing in late summer only 8 could be retrieved. In 1998, velocity at 22 stakes was obtained, 12 in 1999, 27 in 2001 and 2002, 28 in 2003 and 37 in 2004 and 2005. Between autumn 2002 and 2003, the true annual horizontal velocity could be measured by installing a 6 m long iron stake at one locality. The annual velocity obtained was 12.1 ± 1.5 m year^{-1}, not significantly different from the summer velocity in 2002 of 9.7 ± 1.5 m year^{-1}. This is important since it indicates that the summer velocities are representative of the annual velocities.

The annual surface velocity measurements play an important role in the estimation of the ice transported into the system ($\dot{m}_{in}$). The analytical, parallel-sided slab model of a glacier gives a ratio between the vertically averaged velocity of the glacier, $\bar{v}$ and the surface velocity v_s as $\bar{v}/v_s = 0.8$ for a Glen nonlinearity of n = 3 (Paterson, 2001). This ratio is only valid for a parallel-sided slab geometry. The geometry of the inflow region north of Gjálp is more complex (Fig. 4.4) and
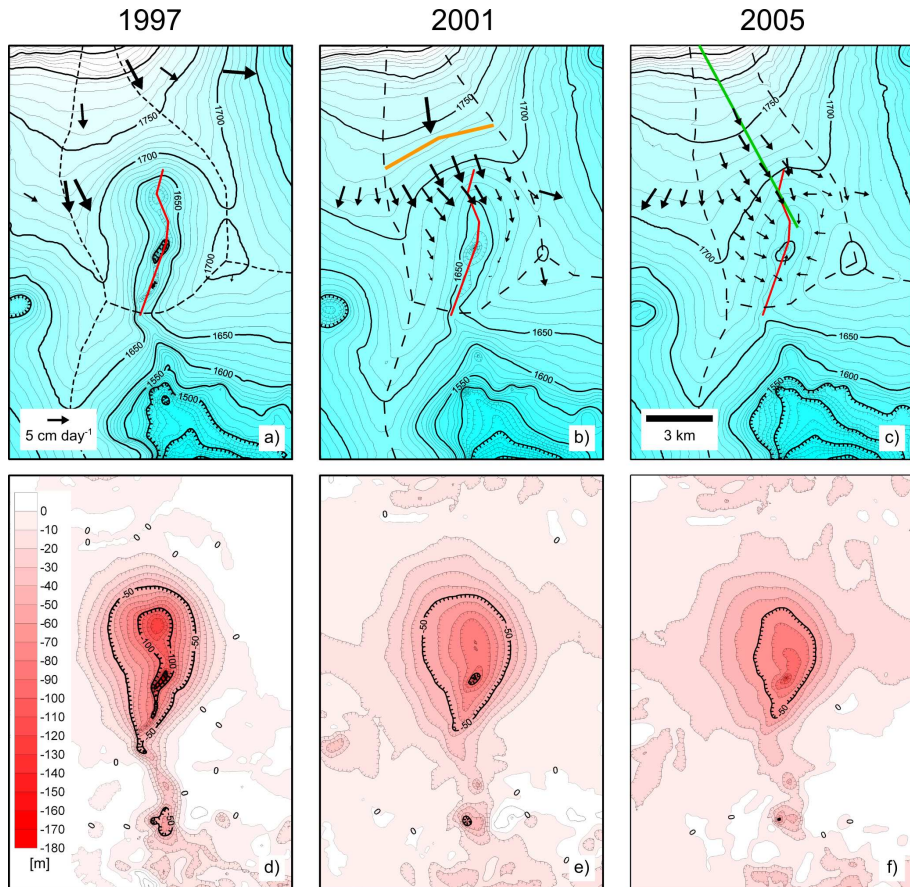
Figure 4.3: Topographic maps for the Gjálp area are shown for 1997, 2001 and 2005 in the upper row (a-c) and the difference between the pre-eruption topography and the respective year in the lower row (d-f). Superimposed on the topography maps are the annual mean surface velocities, displayed as vectors. Dashed lines mark ice divides and the red line outlines the Gjálp ridge. The orange bar in (b) defines the inflow cross-section to the north of Gjálp and the green line (c) marks the position of the 2D flow model (see section 4.3.4)
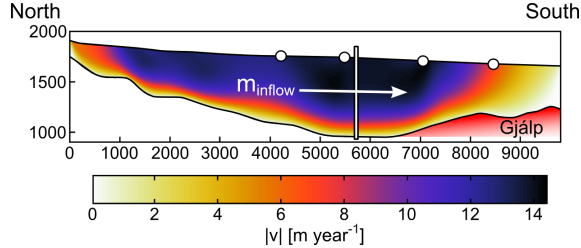
Figure 4.4: The norm of the velocity vector, $|v|$, for the 2005 flow field along the inflow line. The inflow cross-section is marked with a vertical bar and the white dots are the locations of the surface velocity measurements. Bedrock according to Björnsson et al. (1992) and Gudmundsson et al. (2002a)

the ratio $\bar{v}/v_\mathrm{s}$ is not known. Therefore a numerical model of the inflow region was created to evaluate the vertical velocity distribution and to estimate $\bar{v}/v_\mathrm{s}$.

4.3.4   Ice inflow model: $\dot{m}_\mathrm{in}$

Bedrock data from radio echo soundings are available for most parts of Vatna-jökull (Björnsson et al., 1992), and the Gjálp area was re-measured in 1997, 1998 and 2000 to acquire the shape of the edifice formed (Gudmundsson et al., 2002a). This, in combination with the surface maps and the annual surface velocity measurements, makes it possible to create a 2D, finite element model of the inflow area north of Gjálp. Using the Icetools software (Jarosch and Gudmundsson, 2007; Jarosch, 2007), the 2005 surface along with the 2005 surface velocities were used to estimate the $\bar{v}/v_\mathrm{s}$ ratio at the location of the inflow cross section (Fig. 4.3b). The model computes flow velocities along an approximately north-south trending inflow line, which is displayed in Fig. 4.3c.

   The flow field computed with the model is shown in Fig. 4.4, using n=3 in the Glen rheology, $\dot{\varepsilon}_{ij} = A\tau^{n-1}\sigma'_{ij}$ (Glen, 1955; Nye, 1957), and estimating the rate factor A with the surface velocity data. Here $\dot{\varepsilon}_{ij}$ denotes the strain rates and σ'_{ij} the deviatoric stresses.

   This investigation of the vertical velocity distribution at the inflow cross-section estimates $\bar{v}/v_\mathrm{s} = 0.8$, the same value as for a parallel-sided slab model. The rather smooth bedrock topography on the 2 km long section north of Gjálp (Fig. 4.4) causes this local agreement between the numerical and the much more simple model of a parallel-sided slab. Other regions within the inflow area have quite different $\bar{v}/v_\mathrm{s}$ ratios. With the numerically-estimated ratio it is now possible to use the annual surface velocities to calculate $\dot{m}_\mathrm{in}$ for each year through the cross-section defined in Fig. 4.3b.
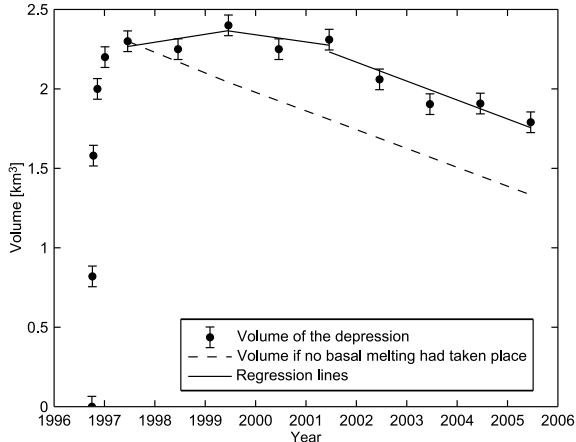
Figure 4.5: The evolution of the surface depression volume, V, throughout the study period . The estimated closure rate of the depression in the absence of basal melting using $\dot{m}_{\mathrm{in}}$ and $\dot{m}_{\mathrm{s}}$ is shown as dashed line. The solid black lines indicate regression lines for three different time periods.

4.4 Results

4.4.1 Thermal power as a function of time

Using the pre-eruption surface together with the annual surface maps yields the volume of the Gjálp depression as a function of time (Fig. 4.5). The change with time, $\dot{V}$, is the derivative of this function.

The heat output, Q_{heat}, was estimated using eqs. (4.1) and (4.2) for the whole study period. A detailed plot of Q_{heat} for the first 100 days after the eruption is shown in Fig. 4.6 and the long term evolution in Fig. 4.7.

The evolution of the heat output from Gjálp from the end of the eruption can be divided into four episodes (Figs. 4.6 and 4.7): (I) The eruption (13 days), (II) end of eruption until June 1997, (III) June 1997-June (2001), and (IV) the period since June 2001. During the eruption (I) the heat output dropped from an initial value of $> 2 \times 10^{12}$ W to 7×10^{10} W (Gudmundsson et al., 2004). A period of rapid drop in heat output followed until June 1997 (II).

The period from June 1997 to June 2001 (III) was split into two two-year periods and linear regression lines were used to identify the average change in volume for these periods (Fig. 4.5). A similar regression line was used for the average volume change during the four year period from June 2001 to June 2005. Until June 2001 changes in the surface depression volume were very small. The volume increased slightly from June 1997 to June 1999 and thereafter decreased

64
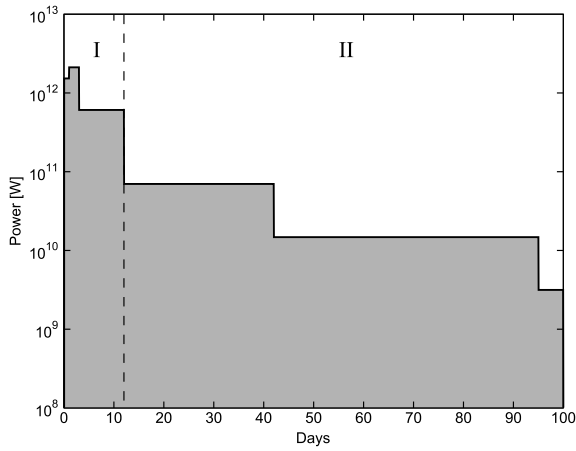
Figure 4.6: Evolution of the heat output of the Gjálp edifice for the first 100 days after the eruption (Gudmundsson et al., 2004). (I) marks the period of the eruption and (II) the period from the end of the eruption until June 1997 (see text).
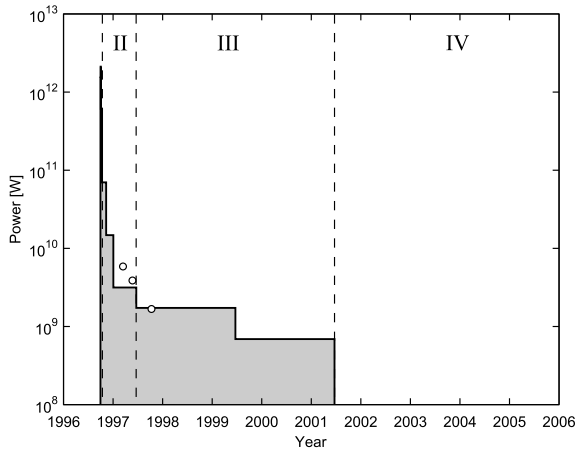
Figure 4.7: Evolution of the heat output of the Gjálp edifice 1996-2006. After June 2001 the power drops to $0 \pm 2 \times 10^8 \, \mathrm{W}$. For comparison the results based on combined InSAR and GPS from Gudmundsson et al. (2002b) are marked with black circles. (II) marks the period from the end of eruption until June 1997, (III) June 1997-June (2001), and (IV) the period since June 2001 (see text).

slightly until June 2001 (Figs. 4.5 and 4.7). From June 2001 onward the depression is closing at an almost constant rate. This approach leads to an average heat output of $17 \pm 2 \times 10^8$ W for the period between June 1997 and June 1999. From June 1999 to June 2001 an average heat output of $7 \pm 2 \times 10^8$ W is obtained. Between June 2001 and June 2005 (IV) no significant heat output was measured. However, since the uncertainty is of the order of 2×10^8 W heat output of 1-2$\times 10^8$ W cannot be excluded during that period.

4.4.2   Energy budget of edifice

The energy balance of the Gjálp eruption can be investigated by considering the following two aspects:

- The total volume of the erupted material can be used to calculate the total eruption energy as $E_{\text{tot}} = \int_{T_0}^{T_{\text{er}}} m_{\text{m}} \, c_{\text{m}} \, dT$ with m_{m} being the mass and c_{m} the specific heat content of the erupted material, T_{er} is the eruption temperature and T_0 the final temperature after cooling, i.e. that of the ice ($\sim 0\,^\circ$C). By ignoring latent heat of crystallization it is assumed that crystalline material constitutes a minor part of the edifice, an assumption based on the rapid heat transfer (Gudmundsson et al., 2002a), direct observations of the top in 1997, and gravity modeling yielding very low bulk density of the edifice (Gudmundsson et al., 2004).

- The presented Q_{heat} data can be integrated over time to derive energy released during that time period. The total energy released during the study period is defined as $E_{\text{rel}} = E_{\text{er}} + E_{\text{post}}$, where the energy released during the eruption (t_{er}) is $E_{\text{er}} = \int_0^{t_{\text{er}}} Q_{\text{heat}} dt$ and the energy released from the end of the eruption until the end of the study period (t_{end}) is $E_{\text{post}} = \int_{t_{\text{er}}}^{t_{\text{end}}} Q_{\text{heat}} \, dt$, ignoring the insignificant energy loss to the atmosphere.

The first estimation of total energy is based on the mass of the erupted material, whereas the second method is based on our record on ice melting and calorimetry.

The total volume of erupted material during the Gjálp eruption was 0.8 ± 0.1 km^3 with an average porosity of 45 % (Gudmundsson et al., 2002a). This yields the mass of erupted magma $m_{\text{m}} = 1.21 \pm 0.20 \times 10^{12}$kg, using a density of volcanic glass as 2750 kg m^{-3}. The energy stored in the erupted magma can be calculated as $E_{\text{m}} = m_{\text{m}} c_{\text{m}} \Delta T$. With $\Delta T = 1090 \pm 50\,^\circ$C being the temperature difference between the initial eruption temperature and 0 $^\circ$C (Gudmundsson et al., 1997), and $c_{\text{m}} = 1100 \pm 50$ J kg^{-1} K^{-1} denoting a temperature-averaged value of the specific heat capacity of the magma (Bacon, 1977), the total energy stored is estimated as $E_{\text{m}} = 1.45 \pm 0.26 \times 10^{18}$ J. Initial volatile content of the Gjálp magma is not known, but only H$_2$O is likely to have been present in sufficient
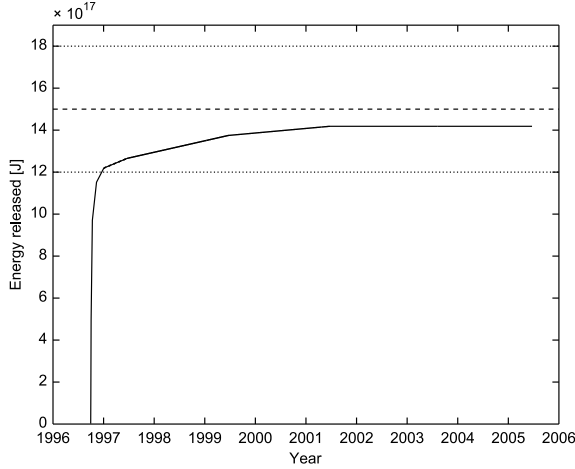
Figure 4.8: The energy released from the Gjálp edifice with time. The dashed line marks the total eruption energy (E_{tot}) with the corresponding error margin as dotted lines.

quantities to be relevant for energy considerations. Taking a plausible value of 0.5-1.0 % H_2O of total mass for basaltic andesite (Wallace and Anderson, Jr., 1999), the maximum energy of volatiles may have been ~3 % of E_{m}. Thus including the volatile contribution, the total thermal energy of the eruption is estimated to have been $E_{\text{tot}} = 1.50 \pm 0.28 \times 10^{18}$ J.

Now E_{tot} can be compared with the energy release from the Gjálp edifice with time (Fig. 4.8) and with the total energy released from Gjálp, E_{rel}, throughout the study period. $E_{\text{rel}} = 1.42 \pm 0.20 \times 10^{18}$ J, which indicates that only some 5 % of the initial energy remained by the end of 2005. During the eruption itself, which lasted for 13 days, $E_{\text{er}} = 0.97 \pm 0.10 \times 10^{18}$ J were released, a remarkable ~64 % of E_{tot}. The energy released gradually since the eruption is $E_{\text{post}} = 0.45 \pm 0.10 \times 10^{18}$ J (Fig. 4.8).

4.4.3 Temperature of edifice

Since the energy released during the eruption (E_{er}) is known and was used to melt ice, it is possible to estimate an average temperature within the edifice after the eruption. Assuming that after the eruption the pore space within the edifice is filled with water in thermal equilibrium with the rock matrix, the average

67
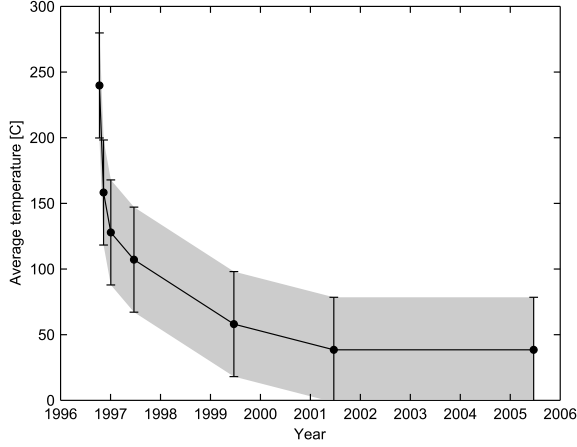
Figure 4.9: The change of average temperature within the Gjálp edifice with time. The gray shaded area indicates the error margins

temperature, T_{av} at a given time t can be estimated as

$$T_{av}(t) = \frac{E_{tot} - E_{er}(t)}{m_{ridge}c_m + m_w c_w}, \qquad (4.3)$$

with m_w being the mass of the water within the pore space and $c_w = 4200$ J kg^{-1} K^{-1} the specific heat capacity of water. For the density of the pore water, which was assumed to be at the pressure boiling point, 900 kg m^{-3} was used. Since 1/8 of the erupted material was transported away from the eruption site by meltwater draining into Grímsvötn (Gudmundsson et al., 2002a), $m_{ridge} = 1.06 \pm 0.20 \times 10^{12}$ kg is the mass of the Gjálp ridge after the eruption. The volcanic glass in Gjálp was highly vesicular (Steinthorsson et al., 2000). This contributes to the high porosity of 45 %. Parts of the pore space are expected to stem from closed minor vesicles in tephra grains, not accessible to pore water. It is therefore sensible to assume a somewhat lower effective porosity, here cautiously estimated as 40 %. This results in mass of the pore water of $m_w = 2.5 \pm 0.5 \times 10^{11}$ kg. The heat capacity of the ridge is an useful quantity and can be estimated as $C_{ridge} = m_{ridge}c_m + m_w c_w = 2.2 \pm 0.4 \times 10^{15}$ J K^{-1}.

Using eq. (4.3) and the given parameter values, we obtain $T_{av} \sim 240\,^{\circ}$C at the end of the eruption. Now the change of average temperature within the edifice with time can be estimated using eq. (4.3) and the energy release history (Fig. 4.8). It is assumed that the porosity remains constant and the effective pore space is always saturated with water. The resulting cooling history is displayed in Fig. 4.9.

The estimated average temperature decreased from initially $\sim 240\,°\mathrm{C}$ right after the eruption to $\sim 128\,°\mathrm{C}$ at the beginning of 1997. In June 1997 the average temperature was $\sim 107\,°\mathrm{C}$. This is broadly consistent with the measured temperature of 60-70 $°\mathrm{C}$ at 0.5 m depth in the exposed part of the ridge at this time(Gudmundsson et al., 2002a, 2004). In June of 1999 the estimated temperature had further decreased to $\sim 58\,°\mathrm{C}$. June 2001 yields a temperature of $\sim 38\,°\mathrm{C}$ with little change happening in 2001-2005 since the energy release during that period was negligible. The errors of $\delta T = \pm 40\,°\mathrm{C}$ in average temperature is cautiously estimated from the fact that the edifice cannot have cooled to temperatures lower than to 0 $°\mathrm{C}$.

4.5 Discussion

4.5.1 Permeability of edifice

Heat transport by advection in a porous medium is strongly dependent on the permeability, regardless of whether one or two phase flow is considered. The permeability is related to the porosity as well as fracturing of a medium but consolidation and alteration act to reduce permeability (Ingebritsen and Sanford, 1999). It is therefore important to estimate possible permeability values for the Gjálp edifice in order to explain the cooling record presented. In the absence of a drill core and permeability measurements, we attempt to explain the cooling record by a simple heat transport model.

If a liquid-phase buoyancy-driven flow through a porous medium is assumed as the main heat transport mechanism within the edifice, possible heat flux values can be calculated. The volumetric flow rate per unit area q_w (Darcy velocity) (Ingebritsen and Sanford, 1999) was estimated using

$$q_\mathrm{w} = \frac{k\rho_0 g\alpha_\mathrm{w}(T_\mathrm{core} - T_\mathrm{surf})}{\mu_\mathrm{w}}, \tag{4.4}$$

with k being the permeability of the rock, ρ_0 the density of water at T_surf , the surface temperature, T_core the core temperature in the center of the Gjálp ridge, g gravitational acceleration, and α_w and μ_w respectively the coefficient of thermal expansion and the dynamic viscosity of water. Heat flux values for given parameters can easily be obtained by using the enthalpy difference $\Delta H = H(T_\mathrm{core}) - H(T_\mathrm{surf})$ of the water as $q_\mathrm{heat} = q_\mathrm{w}\rho_0\Delta H$.

The core temperature of the Gjálp edifice (T_core) was assumed to be double the estimated average temperature T_av given in Fig. 4.9 and the surface of the edifice was assumed to be at $\sim 0\,°\mathrm{C}$. Three permeability values were used to estimate possible heat flux values, two from Surtsey and one from Hawaii. For unaltered hyaloclastite in Surtsey $k_1 = 1.2 \times 10^{-10}\,\mathrm{m}^2$ was used and for altered hyaloclastite at a depth of 60-100 m b.s.l. $k_2 = 4.1 \times 10^{-13}\,\mathrm{m}^2$ (Stefansson
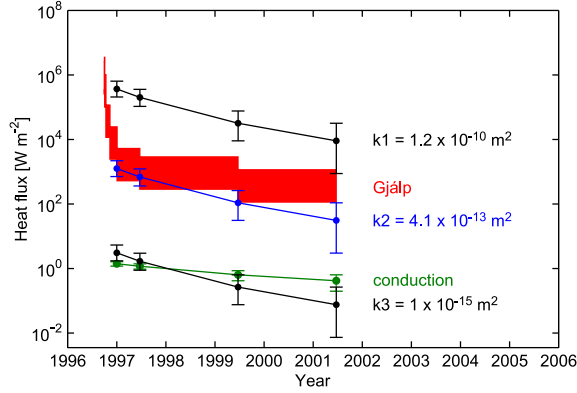
Figure 4.10: Heat flux estimates based on three different permeability values, estimated temperature conditions and assuming liquid phase buoyancy driven flow (see text and Fig. 4.9). The Gjálp heat flux record is displayed in red. For comparison, heat flux values assuming conduction and the same temperature conditions are shown in green. A best fit can be obtained using permeability values of 1-2×10^{-12} m^2.

et al., 1985). The very old hyaloclastite from Hawaii, which was found at a depth of 2000-3000 m b.s.l. has a permeability of $k_3 = 1 \times 10^{-15}$ m^2 (Dannowski, 2002). Using these permeability values together with eq. (4.4) and the assumed temperature conditions, a set of heat flux values can be predicted for each point in time where average temperature has been estimated. The results are shown in Fig. 4.10 together with the heat flux history of Gjálp which was calculated by using the heat output, Q_{heat} (Fig. 4.7) and an area A_{gjalp} , where the heat transport occurs, or $q_{\mathrm{heat}} = Q_{\mathrm{heat}}/A_{\mathrm{gjalp}}$. The area A_{gjalp} was assumed to be either 100 % or 10 % of the total area of the Gjálp edifice, thus yielding a region of possible heat flux values.

As can be seen in Fig. 4.10, the only permeability value matching the heat flux record of Gjálp after the end of the eruption is the one for the altered Surtsey hyaloclastite (k_2). For comparison, heat flux values assuming conduction as the main heat transport mechanism are also shown in Fig. 4.10. An average thickness of ∼200 m for the conducting layer is used to estimate these values together with a thermal conductivity $\lambda = 1.1$ W m^{-1} K^{-1}, a value for porous basalts similar to Gjálp (Robertson and Peck, 1974). For the period before January 1997 thermal conditions inside Gjálp may have been controlled by two phase flow and very efficient heat transport, which can not be explained by this simple model. However after January 1997 this simple model for heat transport within the Gjálp edifice matches the recorded heat flux changes quite well.

70

On the basis of our heat output record and the derived temperature history we propose the following scenario: A short period of very high heat fluxes right after the eruption was driven by two phase convection, that lasted until the end of 1996. If we assume that the heat release was evenly distributed over the surface area of Gjálp, the heat fluxes calculated with eq. (4.4) are not significantly different from the values derived from the heat output record (Fig. 4.10). The gradual reduction in heat flux occurs as a consequence of lowering of the core temperature. After June 2001 no significant heat flux is measured. However, when the error margins are considered, this result is not very robust and the existence of the small cauldron in the center of Gjálp (Fig. 4.2) after 2001 confirms that some thermal energy is still being released. The large drop in heat flux caused by lowering of the core temperature can be understood by considering the nonlinear relationship between buoyant heat flux and temperature difference, since both volume expansivity and viscosity are temperature dependent (eq. 4.3). Thus, a drop in base temperature from $\sim 120\,^{\circ}\mathrm{C}$ to $\sim 80\,^{\circ}\mathrm{C}$ (corresponding to average temperatures of $58\,^{\circ}\mathrm{C}$ to $38\,^{\circ}\mathrm{C}$) leads to a drop in convective heat flux from about $100\ \mathrm{W\ m^{-2}}$ to $\sim 30\ \mathrm{W\ m^{-2}}$.

4.5.2 Implications for development of hyaloclastite mountains

The presented cooling record indicates that the Gjálp edifice sustained large scale geothermal activity over a period of ~ 5 years. After this period no significant heat output was detected, except the small, localized activity at the top of the ridge. The question arises if this rather short period of geothermal activity was long enough for the process of palagonitization to lead to consolidation of the Gjálp edifice. Of importance here is that the observed thermal history cannot be be explained assuming permeability values of loose tephra for the edifice, that would result in much higher heat flux values than observed, given the same edifice temperatures and faster cooling. The reduction in permeability could be caused by consolidation of the material and therefore one could argue that the thermal history indicates considerable consolidation and hence palagonitization. However, in the absence of samples from the ridge confirming compaction and alteration, the extent to which palagonitization has occurred at Gjálp remains speculative.

Another aspect of the preservation potential for the ridge is the diverted local ice flow field. Fig. 4.3c shows clearly that the local ice flow field is still diverted towards the edifice with no overflow of ice occurring in these first 10 years after the eruption, which confines the erupted material in its place. This implies that the process of glacial erosion of the edifice has not been effective after the eruption in 1996. This type of shielding of a hyaloclastite edifice in its early post-eruption development may play important role in the preservation of hyaloclastite ridges

formed in subglacial eruptions.

Finally, it may be instructive to compare the post-eruption development of Gjálp with that of the Surtsey eruption. The island of Surtsey, which was formed in a 4 year period of repeated volcanic activity, has been characterized by a very slow decrease in average temperature and low heat flux values. Borehole measurements done in 1982, 15 years after the end of the island's formation, show that the average temperatures in the core of the island were still above 100 °C while the average heat flux in Surtsey was ∼6 W m^{-2} (Stefansson et al., 1985). Heat transfer in Surtsey was dominated by hydrothermal convection, both above and below sea level. In contrast, average temperatures in Gjálp decreased to values well below 100 °C over the first five years after the eruption. Moreover, the observed heat flux at Gjálp was about two orders of magnitude higher than found in Surtsey. The island of Surtsey is only partly submerged in water and the remaining part is subaerial. Gjálp on the other hand is completely covered with glacier ice, resulting in a practically inexhaustible supply of groundwater that submerges the edifice. This leads to highly efficient heat transfer from hot rocks to the surroundings and faster cooling times than can be expected for an oceanic island like Surtsey.

4.6 Conclusion

We have derived a 10 years record of the heat output and cooling history for the subglacial hyaloclastite ridge formed in the Gjálp eruption in 1996. The main conclusions are:

- The heat output history of Gjálp can be divided into four episodes: (I) The eruption (13 days), (II) end of eruption until June 1997, (III) June 1997 - June (2001), and (IV) the period since June 2001. During episode (I) heat output dropped from initially $> 2 \times 10^{12}$ W to 7×10^{10} W and further decreased to 3×10^9 W by the end of episode (II). An average value of 1.2×10^9 W characterized episode (III) and no significant heat output was measured in episode (IV).

- The total eruptive energy was $1.50 \pm 0.28 \times 10^{18}$ J, estimated from the volume of erupted material. A remarkable $\sim 64\%$ of the total energy was released during the eruption itself and by June 2005, only some 5 % remained within the edifice.

- The heat remaining in the edifice at several points in time has been determined and its average temperature estimated. The temperature dropped from $\sim 240\,°C$ at the end of the eruption to $\sim 128\,°C$ after three months and $\sim 107\,°C$ after nine months. In mid 1999 an average temperature of

$\sim 58\,^{\circ}\mathrm{C}$ is estimated and $\sim 38\,^{\circ}$ by mid 2001, with little cooling occurring since.

- Using a liquid-phase buoyancy-driven convection model and the derived edifice temperatures, it is found that the cooling history is consistent with permeability values of order 10^{-12}-10^{-13} m^2, similar to that estimated for consolidated hyaloclastite in the island of Surtsey, but inconsistent with a pile of loose tephra. This may indicate that the edifice consolidated to dense hyaloclastite in the first 1 or 2 years. However, this remains speculative.

- No traversing ice flow over the edifice was observed in the surface velocity data record, indicating that the surface depression closure still dominates the local ice flow field.

Acknowledgments

Appendix A

Field data

Surface velocities have been measured within the Gjálp region between 1997 and 2005 utilizing GPS measurements of stake locations. The results of these measurements are given in the table below. Names of the stake locations were not systematic before 2000, therefore the systematic names and the old names are listed. Coordinates are given in ISNET 93 along with the height above sea level. The day of the first location measurement is labeled d_1 and the day of the second measurement d_2. Δd is the time in days between d_1 and d_2, Δl is the distance in meters between the two locations and B denotes the bearing of the movement. The horizontal velocity obtained at a given location is labeled v_h.

For 1997-2003 the measurements were done with a Trimble® Pathfinder ProXL submeter instrument (accuracy $\leq$ 1 m). Since 2004 a Trimble® R7 receiver in kinematic mode has been used (accuracy $\sim$ 0.1 m).

Name	Old name	x isnet93	y isnet93	height [m a.s.l]	d_1	d_2	Δd [days]	Δl [m]	B [∘]	v_h [m a^{-1}]
1997										
gjal10	GJ08	574367	448924,7	1721,4	17.06.97	24.08.97	68	5,5	154	29,76
gjal11	GJ07	573660,9	448848,1	1727,4	17.06.97	24.08.97	68	5,1	172	27,2
gjal13	GJ06	571982,7	448794,7	1720,8	17.06.97	24.08.97	68	2,5	121	13,36
	GJ02	581285,8	445242,7	1697,4	17.06.97	24.08.97	68	1,2	192	6,62
	GO1A	581489,4	454685,1	1680	15.05.97	24.08.97	111	8,6	94	28,12
	GO2A	578247	454564,8	1757,1	15.05.97	24.08.97	111	5,6	126	18,27
	GO3A	576651,7	454501,8	1788,6	15.05.97	24.08.97	111	8,6	152	28,37
	GO4A	574302	452562,8	1772,1	15.05.97	24.08.97	111	6,4	176	21,06
1998										
gjal01	NV051	581505,6	449085,2	1692,9	11.06.98	24.08.98	74	1,4	102	6,73
gjal02	NV052	580790	449070,1	1699,7	11.06.98	24.08.98	74	0,5	182	2,47
gjal03	NV053	579992,6	449076,7	1684,8	11.06.98	24.08.98	74	0,9	216	4,41
gjal04	NV054	579177,2	449045,3	1665,3	11.06.98	24.08.98	74	1,8	233	9,03

Name	Old name	x isnet93	y isnet93	height [m a.s.l]	d_1	d_2	Δd [days]	Δl [m]	B [°]	v_h [m a^{-1}]
gjal06	NV056	577823,8	448885	1637,9	11.06.98	24.08.98	74	3,7	147	18,26
gjal07	NV058	576777,4	448963,5	1664	11.06.98	24.08.98	74	6,3	135	30,98
gjal08	NV059	575877,8	448987,6	1686,7	11.06.98	24.08.98	74	4,8	131	23,58
gjal09	NV069	575115,1	448960,7	1703,9	13.06.98	24.08.98	72	3,4	134	17,15
gjal10	NV070	574369,1	448893,6	1718,6	13.06.98	24.08.98	72	1,4	135	6,86
gjal11	NV071	573589,4	448857	1725,2	13.06.98	24.08.98	72	2	234	10,04
gjal12	NV072	572787,4	448858,1	1723,9	13.06.98	24.08.98	72	2,4	220	12,25
gjal20	GO3b	575634,3	446114,5	1692,4	15.06.98	26.08.98	72	2,1	104	10,77
	BB08	567932,2	444373	1596,7	27.05.98	26.08.98	91	7,2	246	28,98
	BB14	576980,9	444022,5	1639,6	28.05.98	25.08.98	89	1,4	160	5,73
	BB15	575322,5	443330,9	1690,4	28.05.98	26.08.98	90	1,3	194	5,1
	BB16	573291,7	443583,9	1652,2	28.05.98	26.08.98	90	3	260	12,33
	BB17	577992,9	449646,9	1653,1	28.05.98	24.08.98	88	6,9	170	28,64
	BB18	581243,7	447195,6	1699,9	28.05.98	25.08.98	89	1,7	186	7,03
	BB19	581188,7	444772,7	1689,7	28.05.98	25.08.98	89	1,4	182	5,7
	BB20	581114,3	442446,4	1644,5	28.05.98	25.08.98	89	4,1	186	16,95
	GO1b	579041,9	450988,9	1706,9	15.06.98	24.08.98	70	4	169	20,76
	GO2b	576633,1	451890,8	1739	15.06.98	24.08.98	70	4,6	149	23,9
	GO4b	575725,8	443903,1	1688,4	15.06.98	26.08.98	72	1,1	99	5,67
	NV055	578413,6	449343,2	1648,8	11.06.98	24.08.98	74	3,5	187	17,02

1999

Name	Old name	x isnet93	y isnet93	height [m a.s.l]	d_1	d_2	Δd [days]	Δl [m]	B [°]	v_h [m a^{-1}]
gjal01	GP01a	581603,9	449109,9	1687,5	20.06.99	24.09.99	96	2,7	21	10,21
gjal02	GP02a	580785,2	449082,1	1695,6	20.06.99	24.09.99	96	1,8	350	6,86
gjal03	GP03a	580011,2	449061,4	1684,2	20.06.99	24.09.99	96	1,9	288	7,09
gjal05	GP05a	578386,5	449037,3	1648,1	20.06.99	24.09.99	96	2,6	218	9,87
gjal06	GP06a	577636,2	449004,1	1645,4	20.06.99	24.09.99	96	2,6	142	9,98
gjal07	GP07a	576787,8	448984,1	1674,3	20.06.99	23.09.99	95	4,1	138	15,9
gjal08	GP08a	576063,9	448944,1	1686,1	20.06.99	23.09.99	95	2,7	119	10,52
gjal09	GP09a	575214,1	448916,4	1703,6	20.06.99	23.09.99	95	2,3	131	8,93
gjal11	GP10a	573547,1	448875,6	1723,4	20.06.99	23.09.99	95	1,7	175	6,5
gjal14	GP11a	576037,4	447113,9	1688,2	20.06.99	23.09.99	95	1,9	112	7,31
gjal15	GP12a	576072,3	445173,4	1682,2	20.06.99	23.09.99	95	1,5	125	5,59
go1e	GO1c	575926,6	452615,9	1758,3	07.05.99	23.09.99	139	8,3	156	21,67

2000

Name	Old name	x isnet93	y isnet93	height [m a.s.l]	d_1	d_2	Δd [days]	Δl [m]	B [°]	v_h [m a^{-1}]
gjal01		581509,1	449080,5	1687,8	12.06.00	15.09.00	95	3,9	58	14,8
gjal02		580802,4	449069,7	1697	12.06.00	15.09.00	95	0,6	270	2,21
gjal03		579999,9	449086	1687	12.06.00	15.09.00	95	0,7	287	2,73
gjal04		579183,7	449051,2	1670,2	12.06.00	15.09.00	95	1,3	283	4,85
gjal05		578399,3	449019,2	1655,2	12.06.00	15.09.00	95	1,8	234	7,07
gjal06		577834,4	448896,1	1652,1	12.06.00	15.09.00	95	1	175	3,93
gjal07		576794,7	448968,3	1678,9	12.06.00	15.09.00	95	3,8	141	14,52
gjal08		575895	448994,8	1694,5	12.06.00	15.09.00	95	3,1	131	12,04
gjal09		575089,1	448957,3	1708,2	14.06.00	15.09.00	93	2	133	7,94
gjal10		574384,4	448895	1718,2	14.06.00	15.09.00	93	1,4	160	5,57
gjal11		573570,3	448875,7	1723,4	14.06.00	15.09.00	93	2,7	194	10,47
gjal12		572770,5	448838	1721,9	14.06.00	15.09.00	93	3,3	219	12,83
gjal13		571978,4	448811,8	1719,3	14.06.00	15.09.00	93	5	223	19,55
gjal14		576043,9	447122,5	1686,3	14.06.00	15.09.00	93	0,7	57	2,78

Name	Old name	x isnet93	y isnet93	height [m a.s.l]	d_1	d_2	Δd [days]	Δl [m]	B [○]	v_h [m a^{-1}]
gjal15		576082,4	445157,3	1680,7	14.06.00	15.09.00	93	0,7	340	2,55
gjal16		579647,5	447228,2	1672,8	14.06.00	15.09.00	93	1,4	287	5,48
gjal17		578849,2	445314,9	1665,7	14.06.00	15.09.00	93	2,5	293	9,98
gjal18		581278,9	445231,2	1694,4	14.06.00	15.09.00	93	1,2	308	4,62
gjal19		584085,6	445410,2	1687	14.06.00	15.09.00	93	1,7	348	6,77
go1d		575930,4	452636,4	1755,6	15.06.00	15.09.00	92	2,1	150	8,18

2001

Name	Old name	x isnet93	y isnet93	height [m a.s.l]	d_1	d_2	Δd [days]	Δl [m]	B [○]	v_h [m a^{-1}]
gjal01a		581590	449085,2	1679,4	04.06.01	15.09.01	97	5,5	106	20,76
gjal02a		580786,6	449070,9	1692,7	04.06.01	15.09.01	97	3,1	130	11,71
gjal03a		580007,5	449019,8	1685,1	04.06.01	15.09.01	97	2,5	158	9,25
gjal04a		579175,5	449012,3	1671,2	04.06.01	15.09.01	97	3	155	11,19
gjal05a		578358,2	449007,8	1659,8	04.06.01	15.09.01	97	5,1	150	19,07
gjal06a		577810,4	448971,8	1660,1	04.06.01	15.09.01	97	5,4	142	20,19
gjal07a		576772,8	448880,6	1682,5	04.06.01	15.09.01	97	5,6	136	21,04
gjal08a		575906,2	448944,3	1695,4	04.06.01	15.09.01	97	4,1	145	15,53
gjal09a		575086,5	448898,6	1707,6	04.06.01	15.09.01	97	5,9	150	22,16
gjal10a		574376,7	448866,6	1716,6	04.06.01	15.09.01	97	4,4	156	16,5
gjal11a		573607,1	448885,3	1720,9	04.06.01	15.09.01	97	3,7	170	13,89
gjal12a		572769,3	448851,9	1719,6	04.06.01	15.09.01	97	4,1	190	15,51
gjal13a		571945	448812,4	1716,5	04.06.01	15.09.01	97	5,1	197	19,07
gjal14a		576064,4	447098	1687,3	04.06.01	16.09.01	97	3,5	147	13,31
gjal15a		576106,1	445204,5	1682,1	04.06.01	16.09.01	97	1,8	155	6,63
gjal16a		579640,6	447130,3	1672,2	04.06.01	16.09.01	97	2,7	197	10,06
gjal17a		578855,3	445285,1	1667,8	04.06.01	16.09.01	97	0,8	261	2,96
gjal18a		581292,9	445296,5	1694,6	04.06.01	16.09.01	97	4,2	168	15,95
gjal20a		576093,7	446220,3	1685,9	04.06.01	16.09.01	97	2,4	149	9,14
gjal21a		576516	448089,2	1682	04.06.01	16.09.01	97	4	141	14,88
gjal22a		576336	449843,7	1699,9	04.06.01	15.09.01	97	6	151	22,51
gjal23a		577273,8	450172	1693,3	04.06.01	16.09.01	97	6,5	159	24,3
gjal24a		578267,3	450318,6	1689,1	04.06.01	16.09.01	97	5,7	161	21,54
gjal25a		579553,3	449933,3	1689,8	04.06.01	16.09.01	97	3,7	157	14,03
gjal26a		579779	448073,5	1675,4	04.06.01	16.09.01	97	3,1	169	11,79
gjal27a		579259,7	446033,4	1671,9	04.06.01	16.09.01	97	1,4	205	5,31
go1e		575902,5	452623,9	1772,1	04.06.01	15.09.01	97	8,2	173	30,93
go4f		584088,5	445421,4	1687,5	04.06.01	16.09.01	97	0,8	77	3,03

2002

Name	Old name	x isnet93	y isnet93	height [m a.s.l]	d_1	d_2	Δd [days]	Δl [m]	B [○]	v_h [m a^{-1}]
gjal01b		581519,9	449093,4	1681,6	03.06.02	13.09.02	102	3,7	70	13,26
gjal02b		580805,2	449067,4	1695,5	03.06.02	13.09.02	102	1,3	59	4,66
gjal03b		579985	449086,4	1690	03.06.02	13.09.02	102	0,8	311	2,82
gjal04b		579175,7	449044,2	1677,2	03.06.02	13.09.02	102	1	206	3,46
gjal05b		578407,3	449022	1669,1	03.06.02	13.09.02	102	2,3	170	8,08
gjal06b		577848,8	448885	1668,6	03.06.02	13.09.02	102	2	154	7,22
gjal07b		576774,4	448953,9	1689,9	03.06.02	13.09.02	102	2,6	144	9,37
gjal08b		575878,9	448994,5	1702,4	03.06.02	13.09.02	102	2,5	144	8,97
gjal09b		575065,6	448960,3	1712,6	03.06.02	13.09.02	102	2	148	7,24
gjal10b		574355	448872,2	1720,7	03.06.02	13.09.02	102	2,2	160	7,82
gjal11b		573572,8	448852,8	1723	03.06.02	13.09.02	102	2,8	189	10
gjal12b		572776,7	448836,6	1721,2	03.06.02	13.09.02	102	4	203	14,37

Name	Old name	x isnet 93	y isnet 93	height [m a.s.l]	d_1	d_2	Δd [days]	Δl [m]	B [°]	v_h [m a^{-1}]
gjal13b		571969,7	448793,8	1718,6	03.06.02	13.09.02	102	4,8	210	17,29
gjal14b		576042,8	447111,8	1691,8	03.06.02	13.09.02	102	2,1	121	7,49
gjal15b		576093,6	445145,8	1685	03.06.02	13.09.02	102	1,2	88	4,18
gjal16b		579637,1	447238,8	1674,8	03.06.02	13.09.02	102	1,1	288	4,06
gjal17b		578860,4	445306,6	1670,5	03.06.02	13.09.02	102	0,9	239	3,1
gjal20b		576058,1	446197,6	1689,4	03.06.02	13.09.02	102	2,3	112	8,13
gjal21b		576456,6	448095,8	1688	03.06.02	13.09.02	102	2,6	118	9,34
gjal22b		576290,7	449824,7	1705,6	03.06.02	13.09.02	102	4,2	141	15,11
gjal23b		577198,8	450157,4	1699,6	03.06.02	13.09.02	102	3,7	153	13,2
gjal24b		578217,7	450313,2	1694,6	03.06.02	13.09.02	102	3,3	150	11,73
gjal25b		579527,8	449960,2	1694,5	03.06.02	13.09.02	102	1,2	138	4,4
gjal26b		579762,2	448135,7	1678,5	03.06.02	13.09.02	102	0,3	248	1,08
gjal27b		579259,5	446053,2	1674,5	03.06.02	13.09.02	102	1,2	275	4,34
gjal28b		576242,3	451407,7	1737,7	06.06.02	13.09.02	99	2,7	153	10,09
go4g		584098,6	445418,2	1688	03.06.02	13.09.02	102	0,5	37	1,73

2003

Name	Old name	x isnet 93	y isnet 93	height [m a.s.l]	d_1	d_2	Δd [days]	Δl [m]	B [°]	v_h [m a^{-1}]
gjal01c		581578,5	449072,8	1678,1	02.06.03	26.09.03	116	4,01	85	12,6
gjal02c		580781,7	449044,1	1692,4	02.06.03	26.09.03	116	2,16	50	6,8
gjal03c		579986,9	449031,2	1690,9	02.06.03	26.09.03	116	0,63	195	1,99
gjal04c		579175,5	449010,4	1680	02.06.03	26.09.03	116	1,04	178	3,27
gjal05c		578374,8	448987,1	1671,9	02.06.03	26.09.03	116	1,71	168	5,37
gjal06c		577833,1	448967,8	1675,5	02.06.03	26.09.03	116	1,27	172	4
gjal07c		576775	448943,3	1694	02.06.03	26.09.03	116	1	91	3,15
gjal08c		575983,4	448920,4	1702,9	02.06.03	26.09.03	116	2,89	147	9,08
gjal09c		575186,6	448901,9	1710,3	02.06.03	26.09.03	116	1,66	153	5,24
gjal10c		574378,4	448879,7	1720,6	02.06.03	26.09.03	116	2,37	178	7,46
gjal11c		573582,1	448858,6	1721,8	02.06.03	26.09.03	116	2,76	193	8,68
gjal12c		572777,2	448838,6	1720,6	02.06.03	26.09.03	116	4,53	210	14,26
gjal13c		571980	448818	1717,2	02.06.03	26.09.03	116	4,43	217	13,93
gjal14c		576050,3	447130,4	1694,2	02.06.03	26.09.03	116	1,56	71	4,91
gjal15c		576092,4	445148,2	1686,6	02.06.03	26.09.03	116	1,3	64	4,07
gjal16c		579649,6	447238,4	1677,1	01.06.03	26.09.03	117	1,54	291	4,79
gjal17c		578853	445323,4	1670,8	01.06.03	26.09.03	117	4,26	315	13,29
gjal20c		576057,3	446210,4	1690,6	02.06.03	26.09.03	116	1,52	28	4,8
gjal21c		576460,1	448081,1	1690,6	02.06.03	26.09.03	116	2,2	93	6,91
gjal22c		576327,4	449838	1707,8	02.06.03	26.09.03	116	3,28	134	10,31
gjal23c		577224,3	450189	1702,4	02.06.03	26.09.03	116	2,92	149	9,2
gjal24c		578219,4	450319,9	1697,2	02.06.03	26.09.03	116	2,46	106	7,73
gjal26c		579766	448152,2	1680,8	01.06.03	26.09.03	117	1,54	309	4,8
gjal27c		579267,1	446033,4	1676,3	01.06.03	26.09.03	117	2,05	301	6,4
gjal28b		576246,3	451401,2	1737,7	14.09.02	26.09.03	377	12,54	152	12,14
go1g		575924,6	452643,1	1756,2	01.06.03	26.09.03	117	3,52	158	10,97
go4h		584087,2	445425,8	1686,1	06.06.03	26.09.03	112	0,73	56	2,39

2004

Name	Old name	x isnet 93	y isnet 93	height [m a.s.l]	d_1	d_2	Δd [days]	Δl [m]	B [°]	v_h [m a^{-1}]
gjal01d		581530,2	449088,5	1677,8	10.06.04	28.09.04	110	3,09	76	10,26
gjal02d		580820,1	449063,4	1691	10.06.04	28.09.04	110	1,44	86	4,79
gjal03d		579985,2	449098,5	1691,9	06.06.04	28.09.04	114	0,51	128	1,63
gjal04d		579193,5	449056,4	1681,6	10.06.04	28.09.04	110	0,75	191	2,5

78

Name	Old name	x isnet93	y isnet93	height [m a.s.l]	d_1	d_2	Δd [days]	Δl [m]	B [∘]	v_h [m a^{-1}]
gjal05d		578418,6	449030,3	1675,3	10.06.04	28.09.04	110	1,37	172	4,53
gjal06d		577846,9	448899	1673,3	10.06.04	28.09.04	110	1,84	153	6,1
gjal07d		576783,4	448953,5	1696,7	06.06.04	28.09.04	114	2,38	141	7,61
gjal08d		575878,5	448989	1706,3	10.06.04	28.09.04	110	1,07	133	3,54
gjal09d		575059,3	448967,7	1713	08.06.04	28.09.04	112	2,12	136	6,91
gjal10d		574346,5	448873,9	1720,5	08.06.04	28.09.04	112	0,75	190	2,45
gjal11d		573560,2	448851,6	1720,4	08.06.04	28.09.04	112	2	142	6,53
gjal12d		572767,9	448834,7	1721,6	08.06.04	28.09.04	112	5,2	230	16,94
gjal13d		571981,9	448794,4	1716,6	08.06.04	28.09.04	112	5,2	213	16,93
gjal14d		576039,4	447107,5	1695	06.06.04	28.09.04	114	1,12	130	3,59
gjal15d		576088,4	445142,2	1687,1	10.06.04	28.09.04	110	0,74	130	2,47
gjal16d		579636,9	447253,6	1679,1	06.06.04	28.09.04	114	1,04	313	3,32
gjal17d		578840,7	445327,9	1672,8	10.06.04	28.09.04	110	1,85	313	6,13
gjal20d		576064,2	446195,7	1692,7	10.06.04	28.09.04	110	0,84	249	2,78
gjal21d		576457,2	448087,9	1694,7	06.06.04	28.09.04	114	1,73	138	5,55
gjal22d		576287,7	449820,9	1709,9	10.06.04	28.09.04	110	1,03	163	3,4
gjal23d		577193,2	450157,7	1704,5	10.06.04	28.09.04	110	2,06	120	6,82
gjal24d		578194,8	450316,1	1699,2	10.06.04	28.09.04	110	0,65	149	2,15
gjal25d		579513,3	449966,9	1696,6	06.06.04	28.09.04	114	1,18	134	3,78
gjal26d		579758,4	448160,7	1681,9	10.06.04	28.09.04	110	1,37	295	4,53
gjal27d		579263,8	446048,1	1677,6	10.06.04	28.09.04	110	1,96	323	6,5
gjal28d		576250,8	451419,6	1740	10.06.04	28.09.04	110	3,02	148	10,02
gjal29d		576947,3	445127,8	1673,2	10.06.04	28.09.04	110	0,76	104	2,52
gjal30d		577771,3	445165,5	1651,7	10.06.04	28.09.04	110	0,31	100	1,03
gjal31d		576971,5	446216	1676,9	10.06.04	28.09.04	110	1,15	108	3,82
gjal32d		577092,5	447133,3	1673,3	10.06.04	28.09.04	110	1,49	120	4,95
gjal33d		577410,2	447871,2	1674	10.06.04	28.09.04	110	1,46	119	4,85
gjal34d		578696,9	447902,7	1662,8	10.06.04	28.09.04	110	0,9	190	2,99
gjal35d		578653,4	447148,9	1651,1	10.06.04	28.09.04	110	0,3	241	1
gjal36d		578123	446013	1644,4	10.06.04	28.09.04	110	0,47	321	1,57
gjal37d		577277,4	451445,5	1729,3	10.06.04	28.09.04	110	3,3	143	10,94
gjal38d		575338,1	450596,3	1733,6	10.06.04	28.09.04	110	2,72	159	9,04
go1h		575915,4	452649,9	1755,6	18.07.04	28.09.04	72	2,24	127	11,34
go1h		575914,1	452651,1	1756,5	09.06.04	18.07.04	39	1,39	143	13,03
go1hx		575911,7	452651,8	1755,7	06.06.04	28.09.04	114	3,13	154	10,03
go4i		584083,3	445432,3	1685,9	09.06.04	18.07.04	39	0,44	45	4,15
go4i		584083,5	445432,8	1685,5	18.07.04	28.09.04	72	0,56	38	2,85

2005

Name	Old name	x isnet93	y isnet93	height [m a.s.l]	d_1	d_2	Δd [days]	Δl [m]	B [∘]	v_h [m a^{-1}]
gjal01e		581528,7	449091,7	1676,1	10.06.05	01.10.05	113	1,64	100	5,3
gjal02e		580812,6	449069,4	1689,3	10.06.05	01.10.05	113	1,41	167	4,55
gjal03e		579978,2	449095,3	1691,5	10.06.05	01.10.05	113	0,55	116	1,78
gjal04e		579191,3	449060,3	1682,9	10.06.05	01.10.05	113	1,38	270	4,44
gjal05e		578413,2	449046,5	1678,8	08.06.05	02.10.05	116	1,37	161	4,32
gjal05ne		578417,1	449044,3	1678,8	08.06.05	02.10.05	116	1,28	167	4,01
gjal06e		577850,9	448904,9	1677,9	08.06.05	02.10.05	116	1,74	145	5,48
gjal06ne		577847,2	448907,2	1677,9	08.06.05	02.10.05	116	1,86	155	5,86
gjal07e		576784,8	448951,9	1698,6	08.06.05	02.10.05	116	2,33	141	7,32
gjal07ne		576783,2	448956,7	1698,7	08.06.05	02.10.05	116	2,35	141	7,38
gjal08e		575885	448987,8	1707,8	08.06.05	03.10.05	117	2,3	147	7,19

Name	Old name	x isnet93	y isnet93	height [m a.s.l]	d_1	d_2	Δd [days]	Δl [m]	B [∘]	v_h [m a^{-1}]
gjal08ne		575884	448992,2	1707,8	08.06.05	03.10.05	117	2,07	147	6,44
gjal09e		575185,8	448891,8	1712,9	08.06.05	03.10.05	117	2,02	159	6,32
gjal10e		574367,8	448864,9	1720,1	08.06.05	03.10.05	117	2,32	182	7,23
gjal11e		573568,8	448855	1720,1	08.06.05	03.10.05	117	3,03	198	9,47
gjal12e		572764,6	448847,2	1718,2	10.06.05	03.10.05	115	4,29	205	13,6
gjal13e		571980,1	448814,6	1715,4	10.06.05	03.10.05	115	5,56	213	17,65
gjal14e		576047,2	447107	1695,5	08.06.05	02.10.05	116	1,41	127	4,43
gjal15e		576093,2	445134,6	1687,8	08.06.05	02.10.05	116	0,84	127	2,64
gjal16e		579635,8	447254,8	1678,8	10.06.05	02.10.05	114	0,49	274	1,57
gjal17e		578841,5	445333,9	1673,8	08.06.05	02.10.05	116	0,51	274	1,62
gjal20e		576066,7	446196,6	1692,2	08.06.05	02.10.05	116	1,02	135	3,21
gjal21e		576465,9	448082	1696,6	08.06.05	02.10.05	116	1,79	140	5,62
gjal21ne		576462,3	448083,1	1696,5	08.06.05	02.10.05	116	1,73	144	5,43
gjal22e		576284,7	449816,9	1711,4	08.06.05	01.10.05	115	2,76	149	8,78
gjal22ne		576287,6	449820,5	1711,5	08.06.05	01.10.05	115	2,6	149	8,27
gjal23e		577198,6	450153,1	1706,6	08.06.05	01.10.05	115	2,78	146	8,84
gjal23ne		577193,6	450151,6	1706,7	08.06.05	01.10.05	115	2,84	144	9,03
gjal24e		578202,3	450299	1698,4	08.06.05	01.10.05	115	2,53	143	8,02
gjal24ne		578206,4	450297,4	1698	08.06.05	01.10.05	115	3,09	174	9,81
gjal25e		579515,9	449973,1	1696,6	08.06.05	02.10.05	114	1,33	119	4,25
gjal26e		579758	448166,4	1682,6	10.06.05	02.10.05	114	0,23	190	0,72
gjal27e		579264,2	446059,5	1678,8	08.06.05	02.10.05	116	0,44	292	1,39
gjal28e		576245,2	451415,1	1740,5	08.06.05	01.10.05	115	3,17	151	10,06
gjal28ne		576250	451415,2	1740,5	08.06.05	01.10.05	115	3,25	149	10,3
gjal29e		576944	445119,8	1675	08.06.05	02.10.05	116	0,83	119	2,6
gjal30e		577771	445165,6	1654,2	08.06.05	02.10.05	116	0,43	124	1,36
gjal31e		576985	446207,8	1678,1	08.06.05	02.10.05	116	1,17	111	3,68
gjal32e		577090,3	447138,3	1675,3	08.06.05	02.10.05	116	1,42	121	4,47
gjal33e		577400,1	447887,8	1676,8	08.06.05	02.10.05	116	1,64	137	5,16
gjal34e		578695,4	447906,2	1664,2	10.06.05	02.10.05	114	0,35	179	1,13
gjal36e		578118	446011,2	1646,7	08.06.05	02.10.05	116	0,4	12	1,25
gjal37e		577269,8	451456,4	1730,1	08.06.05	01.10.05	115	3,15	142	9,98
gjal38e		575322,8	450598,5	1734,3	10.06.05	01.10.05	113	2,75	160	8,89
go1i		575920,5	452636,9	1756,1	01.05.05	01.10.05	153	4,03	158	9,61
go4j		584094,6	445406,7	1685	05.06.05	11.08.05	67	0,6	11	3,29
go4j		584094,9	445407	1683,5	11.08.05	02.10.05	52	0,42	72	2,95

Bibliography

Aðalgeirsdóttir, G., Gudmundsson, G. H., Björnsson, H., 2000. The response of a glacier to a surface disturbance: a case study on Vatnajokull ice cap, Iceland. Annals of Glaciology 31, 104–110.

Aðalgeirsdóttir, G., Gudmundsson, G. H., Björnsson, H., 2003. A regression model for the mass-balance distribution of the Vatnajökull ice cap, Iceland. Annals of Glaciology 37, 189 − 193.

Aðalgeirsdóttir, G., Gudmundsson, G. H., Björnsson, H., 2005. Volume sensitivity of Vatnajökull Ice Cap, Iceland, to perturbations in equilibrium line altitude. Journal of Geophysical Research - Earth Surface 110, F04001, doi:10.1029/2005JF000289.

Aðalgeirsdóttir, G., Jóhannesson, T., Björnsson, H., Pálsson, F., O. Sigurðsson, O., 2006. Response of Hofsjökull and southern Vatnajökull, Iceland, to climate change. Journal of Geophysical Research - Earth Surface 111, F03001, doi:10.1029/2005JF000388.

Allen, M. P., Tildesley, D. J., 1989. Computer Simulation of Liquids. Oxford University Press, Oxford.

Alsdorf, D. E., Smith, L. C., 1999. Interferometric SAR observations of ice topography and velocity changes related to the 1996, Gjalp subglacial eruption, Iceland. International Journal of Remote Sensing 20, 3031–3050.

Arrow, K. J., Hurwicz, L., Uzawa, H., 1958. Studies in Linear and Non-Linear Programming. Stanford University Press, Stanford, CA.

Bacon, C. R., 1977. High temperature heat content and heat capacity of silicate glasses: experimental determination and a model for calculation. American Journal of Science 277, 109–135.

Balay, S., Buschelman, K., Eijkhout, V., Gropp, W. D., Kaushik, D., Knepley, M. G., Curfman McInnes, L., Smith, B. F., Zhang, H., 2004. PETSc users manual. Tech. Rep. ANL-95/11 - Revision 2.1.5, Argonne National Laboratory.

Balay, S., Eijkhout, V., Gropp, W. D., Curfman McInnes, L., Smith, B. F., 1997. Efficient management of parallelism in object oriented numerical software libraries. In: Arge, E., Bruaset, A. M., Langtangen, H. P. (Eds.), Modern Software Tools in Scientific Computing. Birkhäuser Press, pp. 163–202.

Behrendt, J. C., Blankenship, D. D., Damaske, D., Cooper, A. K., 1995. Glacial removal of late Cenozoic subglacially emplaced volcanic edifices by the West Antarctic ice sheet. Geology 23, 1111–1114.

Behrendt, J. C., Blankenship, D. D., Finn, C. A., Bell, R. E., Sweeney, R. E., Hodge, S. R., Brozena, J. M., 1994. Evidence for late Cenozoic flood basalts(?) in the West Antarctic rift system revealed by the CASERTZ aeromagnetic survey. Geology 22, 527–530.

Björnsson, H., 1974. Explanation of jökulhlaups from Grímsvötn, Vatnajökull, Iceland. Jökull 24, 1–26.

Björnsson, H., 1975. Subglacial water reservoirs, jökulhlaups and volcanic eruptions. Jökull 25, 1–14.

Björnsson, H., 1977. The cause of jökulhlaups in the Skaftá river, Vatnajökull. Jökull 27, 71–78.

Björnsson, H., 1988. Hydrology of Ice Caps in Volcanic Regions. Rit XLV. Societas Scientarium Islandica, Reykjavík.

Björnsson, H., 2003. Subglacial lakes and jökulhlaups in Iceland. Global and Planetary Change 35, 255 – 271.

Björnsson, H., Einarsson, P., 1990. Volcanoes beneath Vatnajökull, Iceland: evidence from radio-echo sounding, earthquakes and jökulhlaups. Jökull 40, 147–168.

Björnsson, H., Gudmundsson, M. T., 1993. Variations in the thermal output of the Subglacial Grímsvötn Caldera, Iceland. Geophysical Research Letters 20 (19), 2127 – 2130.

Björnsson, H., Pálsson, F., Gudmundsson, M. T., 1992. Vatnajökull, northwestern part: ice surface and bedrock maps. University of Iceland. National Power Company and Science Institute., Reykjavik.

Björnsson, H., Pálsson, F., Haraldsson, H. H., 2002. Mass balance of Vatnajökull (1991-2001) and Langjökull (1996-2001). Jökull 51, 75–78.

Björnsson, H., Rott, H., Gudmundsson, S., Fischer, A., Siegel, A., Gudmundsson, M. T., 2001. Glacier-volcano interaction deduced by SAR interferometry. Journal of Glaciology 47 (156), 58 – 70.

Blankenship, D. D., Bell, R. E., Hodge, S. M., Brozena, J. M., Behrendt, J. C., Finn, C. A., 1993. Active volcanism beneath the West Antarctic ice sheet and implications for ice-sheet stability. Nature 361, 526 − 529.

Bourgeois, O., Dauteuil, O., van Vliet-Lanoë, B., 1998. Pleistocene subglacial volcanism in Iceland: tectonic implications. Earth and Planetary Science Letters 164, 165–178.

Clarke, G. K. C., Cross, G. M., Benson, C. S., 1989. Radar Imaging of Glaciovolcanic Stratigraphy, Mount Wrangell Caldera, Alaska - Interpretation Model and Results. Journal of Geophysical Research - Solid Earth and Planets 94, 7237 − 7249.

Clough, R. W., September 1960. The finite element method in plane stress analysis. In: Proceedings 2nd ASCE Conference on Electronic Computation. Pittsburgh, Pa.

Cressie, N. A. C., 1991. Statistics for Spatial Data. John Wiley & Sons, New York.

Dannowski, G., 2002. Untersuchungen des thermo-hydraulischen Feldes und der Wärmeflussdichte in der Nähe eines aktiven Mantelplumes (Insel Hawaii) mit Hilfe von Bohrlochtemperaturmessungen. Str02/03, Technische Universität Berlin.

Einarsson, P., Brandsdóttir, B., Gundmundsson, M. T., Björnsson, H., K., G., Sigmundsson, F., 1997. Center of the Icelandic hotspot experiences volcanic unrest. Eos 78, 369 − 375.

Einarsson, P., Sæmundsson, K., 1987. Earthquake epicenters 1982-1985 and volcanic systems in Iceland (map). Menningarsjóður, Reykjavík.

Flowers, G. E., Björnsson, H., Pálsson, F., 2003. New insights into the subglacial and periglacial hydrology of Vatnajökull, Iceland, from a distributed physical model. Journal of Glaciology 49 (165), 257–270.

Flowers, G. E., Björnsson, H., Pálsson, F., Clarke, G. K. C., 2004. A coupled sheet-conduit mechanism for jökulhlaup propagation. Geophysical Research Letters 31, L05401, doi:10.1029/2003GL019088.

Galerkin, B. G., 1923. Series solutions of some problems in elastic equilibrium of rods and plates (russian). Vestnik Inzhenerov i Tekhnikov 19, 897–908.

Gauss, C. F., 1809. Werke, Bd. VII: Theoretische Astronomie. Königliche Gesellschaft der Wissenschaften (reprint 1906), Göttingen.

Glen, J. W., 1955. The creep of polycrystalline ice. Proceedings of the Royal Society, London A228 (1175), 519 − 538.

Gudmundsson, G. H., 1994. Glacier sliding over sinusoidal bed and the characteristics of creeping flow over bedrock undulations. Mitteilung 130, Versuchsanstalt für Wasserbau, Hydrologie und Glaziologie der ETH Zürich, Gloriastrasse 37-39, ETH-Zentrum, CH-8092 Zürich.

Gudmundsson, G. H., 1999. A three-dimensional numerical model of the confluence area of Unteraargletscher, Bernese Alps, Switzerland. Journal of Glaciology 45 (150), 219–230.

Gudmundsson, G. H., 2003a. Transmission of basal variability to a glacier surface. Journal of Geophysical Research 108 (B5), 2253, doi:10.1029/2002JB002107.

Gudmundsson, M. T., 2003b. Melting of ice by magma-ice-water interactions during subglacial eruptions as an indicator of heat transfer in subaqueous eruptions. In: White, J. D. L., Smellie, J. L., Claque, D. A. (Eds.), Explosive Subaqueous Volcanism. American Geophysical Union, Monograph, 140, pp. 61–72.

Gudmundsson, M. T., 2005. Subglacial volcanic activity in Iceland. In: Caseldine, C., Russel, A., Hardardottir, J., Knudsen, O. (Eds.), Iceland - Modern Processes and Past Environments. Elsevier, pp. 127 − 151.

Gudmundsson, M. T., Björnsson, H., 1991. Eruption in Grimsvötn, Vatnajökull, Iceland, 1934-1991. Jökull 41, 21–45.

Gudmundsson, M. T., Björnsson, H., Palsson, F., 1995. Changes in Jökulhlaup Sizes in Grimsvötn, Vatnajökull, Iceland, 1934-91, deduced from in-situ Measurements of Subglacial Lake Volume. Journal of Glaciology 41, 263 − 272.

Gudmundsson, M. T., Högnadóttir, Þ., 2005. Jarðhiti í Grímsvötnum árið 2004, tengsl eldgoss og jarðhita. Tech. Rep. RH-02-2005, Jarðvísindastofnun Háskólans.

Gudmundsson, M. T., Högnadóttir, Þ., Kristinsson, A. B., Gudbjörnsson, S., 2007. Geothermal activity in the subglacial Katla caldera, Iceland, 1999-2005, studied with radar altimetry. Annals of Glaciology 45, 66–72.

Gudmundsson, M. T., Pálsson, F., Björnsson, H., Högnadóttir, Þ., 2002a. The hyaloclastite ridge formed in the subglacial 1996 eruption in Gjálp, Vatnajökull, Iceland: present day shape and future preservation. In: Smellie, J. L., Chapman, J. L. (Eds.), Volcano-Ice Interaction on Earth and Mars. Vol. 202. Geological Society, London, Special Publications, pp. 319 − 335.

Gudmundsson, M. T., Sigmundsson, F., Björnsson, H., 1997. Ice-volcano inter-action of the 1996 Gjálp subglacial eruption, Vatnajökull, Iceland. Nature 389, 954 − 957.

Gudmundsson, M. T., Sigmundsson, F., Björnsson, H., Högnadóttir, Þ., 2004. The 1996 eruption at Gjálp, Vatnajökull ice cap, Iceland: efficiency of heat transfer, ice deformation and subglacial water pressure. Bulletin of Volcanology 66, 46 − 65.

Gudmundsson, S., Gudmundsson, M. T., Björnsson, H., Sigmundsson, F., Rott, H., Carstensen, J. M., 2002b. Three-dimensional glacier surface motion maps at Gjálp eruption site, Iceland, inferred from combining InSAR and other ice-displacement data. Annals of Glaciology 34, 315 − 322.

Helbing, J., 2006. Glacier dynamics of Unteraargletscher: Verifying theoretical concepts through flow modeling. Mitteilung 169, Versuchsanstalt für Wasser-bau, Hydrologie und Glaziologie der ETH Zürich, Gloriastrasse 37-39, ETH-Zentrum, CH-8092 Zürich.

Hickson, C. J., 2000. Physical control and resulting morphologic forms of Qua-ternary ice-contact volcanos in western Canada. Geomorphology 32, 239 − 261.

Hindmarsh, R. C. A., 2004. A numerical comparison of approximations to the stokes equations used in ice sheet and glacier modeling. Journal of Geophysical Research 109, F01012, doi:10.1029/2003JF000065.

Hindmarsh, R. C. A., Leysinger Vieli, G. J.-M. C., Raymond, M. J., Gudmunds-son, G. H., 2006. Draping or overriding: The effect of horizontal stress gradients on internal layer architecture in ice sheets. Journal of Geophysical Research - Earth Surface 111, F02018, doi:10.1029/2005JF000309.

Hubbard, A., Blatter, H., Nienow, P., Mair, D., Hubbard, B., 1998. Comparison of a three-dimensional model for glacier flow with field data from Haut Glacier d'Arolla, Switzerland. Journal of Glaciology 44 (147), 368–378.

Hutter, K., 1983. Theoretical Glaciology: Material Science of Ice and the Me-chanics of Glaciers and Ice Sheets. Kluwer Academic Publishers, Dordrecht, Holland.

Ingebritsen, S. E., Sanford, W. E., 1999. Groundwater in Geologic Processes. Cambridge University Press.

Jakobsson, S. P., 1972. On the consolidation and palagonization of the tephra of the Surtsey volcano island, Iceland. Surtsey Research Progress Report VI, Surtsey Research Society, Reykjavik.

Jakobsson, S. P., 1978. Environmental factors controlling the palagonization of the Surtsey tephra, Iceland. Bulletin of the Geological Society of Denmark 27, $91 - 105$.

Jakobsson, S. P., 1979. Outline of the petrology of Iceland. Jökull 29, $57 - 73$.

Jakobsson, S. P., Moore, J. G., 1986. Hydrothermal minerals and alteration rates at Surtsey volcano, Iceland. Geological Society of America Bulletin 97, 648–659.

Jarosch, A. H., 2007. Icetools: a Full Stokes finite element model for glaciers. Computers & Geosciences (in review).

Jarosch, A. H., Gudmundsson, M. T., 2007. Numerical studies of ice flow over subglacial geothermal heat sources at Grímsvötn, Iceland, using Full Stokes equations. Journal of Geophysical Research - Earth Surface 112, F02008, doi:10.1029/2006JF000540.

Jóhannesson, T., 1992. Landscape of temperate ice caps. Ph.D. thesis, University of Washington.

Jóhannesson, T., 2002. Propagation of a subglacial flood wave during the initiation of a jökulhlaup. Hydrological Sciences Journal 47 (3), 417–434.

Jones, J. G., 1969. Intraglacial volcanoes of the Laugarvatn region, south-west Iceland - I. Quarterly Journal of the Geological Society London 124, $197 - 211$.

Jónsson, S., Adam, N., Björnsson, H., 1998. Effects of subglacial geothermal activity observed by satellite radar interferometry. Geophysical Research Letters 25 (7), $1059 - 1062$.

Kjartansson, G., 1943. The geology of Árnessýsla district. Árnesingafélagid, Reykjavik.

Langley, K., 2000. A morphological investigation of volcanic activity beneath Vatnajökull, Iceland, interpreted from radio-echo sounding data. Master's thesis, University of Iceland.

Larsen, G., 2002. A brief overview of eruptions from ice-covered and ice-capped volcanic systems in iceland during the past 11 centuries: frequency, periodicity and implications. In: Smellie, J. L., Chapman, M. C. (Eds.), Volcano-Ice Interaction on Earth and Mars. Geological Society, London, Special Publications, 202, pp. $81 - 90$.

Larsen, G., Gudmundsson, M. T., Björnsson, H., 1998. Eight centuries of periodic volcanism at the center of the Iceland hotspot revealed by glacier tephrostratigraphy. Geology 26, $943 - 946$.

Le Meur, E., Gagliardini, O., Zwinger, T., Ruokolainen, J., 2004. Glacier flow modelling: a comparison of the Shallow Ice Approximation and the full-Stokes solution. Comptes Rendus Physique 5, 709 − 722.

Lescinsky, D. T., Fink, J. H., 2000. Lava and ice interaction at stratovolcanoes: Use of characteristic features to determine past glacial extents and future volcanic hazards. Journal of Geophysical Research - Solid Earth 105.

Leysinger Vieli, G. J.-M. C., Gudmundsson, G. H., 2004. On estimating length fluctuations of glaciers caused by changes in climatic forcing. Journal of Geophysical Research - Earth Surface 109, F01007, doi:10.1029/2003JF000027.

Luthi, M., Funk, M., Iken, A., Gogineni, S., Truffer, M., 2002. Mechanisms of fast flow in Jakobshavn Isbrae, West Greenland: Part III. Measurements of ice deformation, temperature and cross-borehole conductivity in boreholes to the bedrock. Journal of Glaciology 48 (162), 369–385.

Major, J. J., Newhall, C. G., 1989. Snow and Ice Perturbation during Historical Volcanic-Eruptions and the Formation of Lahars and Floods - A Global Review. Bulletin of Volcanology 52, 1 − 27.

Marshall, S. J., 2005. Recent advances in understanding ice sheet dynamics. Earth and Planetary Science Letters 240, 191 − 204.

Marshall, S. J., Björnsson, H., Flowers, G. E., Clarke, G. K. C., 2005. Simulation of Vatnajökull ice cap dynamics. Journal of Geophysical Research - Earth Surface 110, F03009, doi:10.1029/2004JF000262.

Martin, C., Navarro, F., Otero, J., Cuadrado, M. L., Corcuera, M. I., 2004. Three-dimensional modelling of the dynamics of Johnsons Glacier, Livingston Island, Antarctica. Annals of Glaciology 39, 1 − 8.

Mathews, W. H., 1947. "Tuyas", flat topped volcanos in northern British Columbia. American Journal of Science 245, 560 − 570.

McHenry, D., 1943. A lattice analogy for the solution of plane stress problems. Journal of the Institution of Civil Engineers 21, 59–82.

Mickens, R. E., 1994. Nonstandard Finite Difference Models of Differential Equations. World Scientific, Singapore.

Nye, J. F., 1957. The distribution of stress and velocity in glaciers and ice sheets. Proceedings of the Royal Society London 239, 113 − 133.

Paterson, W. S. B., 2001. The Physics of Glaciers, 3rd Edition. Butterworth Heinemann, Oxford.

Pattyn, F., 2003. A new three-dimensional higher-order thermomechanical ice sheet model: Basic sensitivity, ice stream development, and ice flow across subglacial lakes. Journal of Geophysical Research - Solid Earth 108 (B8), 2382, doi:10.1029/2002JB002329.

Petrenko, V. F., Whitworth, R. W., 1999. Physics of Ice. Oxford University Press, Oxford.

Pettit, E. C., Waddington, E. D., 2003. Ice flow at low deviatoric stress. Journal of Glaciology 49 (166), 359–369.

Pozrikidis, C., 1996. Introduction to Theoretical and Computational Fluid Dynamics. Oxford University Press, New York.

Pralong, A., Funk, M., 2006. On the instability of avalanching glaciers. Journal of Glaciology 52 (176), 31–48.

Raymond, M. J., Gudmundsson, G. H., 2005. On the relationship between surface and basal properties on glaciers, ice sheets, and ice streams. Journal of Geophysical Research - Solid Earth 110, B08411, doi:10.1029/2005JB003681.

Richardson, L. F., 1910. The approximate arithmetical solution by finite differences of physical problems. Transactions of the Royal Society (London) A210, 307–357.

Robertson, E. C., Peck, D. L., 1974. Thermal conductivity of vesicular basalt from Hawaii. Journal of Geophysical Research 79 (32), 4875–4888.

Saad, Y., Schultz, M. H., 1986. Gmres: A generalized minimal residual algorithm for solving nonsymmetric linear systems. SIAM Journal on Scientific and Statistical Computing 7 (3), 856–869.

Saito, F., Abe-Ouchi, S., Blatter, H., 2003. Effects of first-order stress gradients in an ice sheet evaluated by a three-dimensional thermomechanical coupled model. Annals of Glaciology 37, 166–172.

Schopka, H. H., Gudmundsson, M. T., Tuffen, H., 2006. The formation of Helgafell, southwest Iceland, a monogenetic subglacial hyaloclastite ridge: Sedimentology, hydrology and volcano-ice interaction. Journal of Volcanology and Geothermal Research 152, 359 − 377.

Sigmundsson, F., 2006. Iceland Geodynamics. Crustal Deformation and Divergent Plate Tectonics. Springer-Praxis, Berlin.

Sigvaldason, G. E., 1965. The Grímsvötn thermal area. Chemical analysis of jökulhlaup water. Jökull 15, 125–128.

Smellie, J. L., 1999. Lithostratigraphy of Miocene-Recent, alkaline volcanic fields in the Antarctic Peninsula and eastern Ellsworth Land. Antarctic Science 11, 347 − 363.

Stefansson, V., Axelsson, G., Sigurdsson, O., Gudmundsson, G., Steingrimsson, B., 1985. Thermal conditions of Surtsey. Journal of Geodynamics 4, 91–106.

Steinthorsson, S., Hardarson, B. S., Ellam, R. M., Larsen, G., 2000. Petrochemistry of the Gjálp-1996 subglacial eruption, Vatnajökull, SE Iceland. Journal of Volcanology and Geothermal Research 98, 79–90.

Stroncik, N. A., Schmincke, H. U., 2002. Palagonite - a review. International Journal of Earth Sciences 91, 680–697.

Thorarinsson, S., 1974. Vötnin Stríð. Saga Skeiðarárhlaupa og Grímsvatnagosa [The swift flowing rivers: the history of Grímsvötn jökulhlaups and eruptions]. Menningarsjóður, Reykjavík.

Thordarson, T., Larsen, G., 2007. Volcanism in Iceland in historical time: Volcano types, eruption styles and eruptive history. Journal of Geodynamics 43, 118–152.

Tucker, M. A., Hirota, Y., Wamsley, E. J., Lau, H., Chaklader, A., Fishbein, W., 2006. A daytime nap containing solely non-REM sleep enhances declarative but not procedural memory. Neurobiology of Learning and Memory 86, 241–247.

van Bemmelen, R. W., Rutten, M. G., 1955. Table mountains of northern Iceland. EJ Brill, Leiden.

Velichko, A. A., Kononov, Y. M., Faustova, M. A., 1997. The last glaciation on Earth: Size and volume of ice-sheets. Quaternary International 41/41, 43–51.

Wallace, P., Anderson, Jr., A. T., 1999. Encyclopedia of Volcanoes. Academic Press, San Diego, Ch. Volatiles in Magmas, pp. 149–170.

Wolfe, C. J., Bjarnason, I. Þ., VanDecar, J. C., Solomon, S. C., 1997. Seismic structure of the Iceland mantle plume. Nature 385, 245–247.

Zienkiewicz, O. C., Taylor, R. L., Zhu, J., 2005. The Finite Element Method: Its Basis and Fundamentals, 6th Edition. Butterworth Heinemann, Oxford.